Investigating Microstructure in the Brain using Diffusion Weighted Magnetic Resonance Imaging

Seyed Hamed Yousefi Mesri

Submitted in total fulfilment of the requirements of the degree of

Master of Philosophy

March 2014

Department of Electrical and Electronic Engineering,

The University of Melbourne

Abstract

The morphological structure of the brain plays an important role in studying neurodegenerative diseases and disorders. Despite the great importance of the investigation of the brain microstructure, there is not any direct and non-invasive imaging techniques available to measure the micro-structural tissue parameters. Conventional Magnetic Resonance Imaging (MRI) cannot provide images of the brain microstructure due to the limitations in the image resolution. Hence, there is a need to develop indirect techniques to measure the microscopic features of the brain tissue.

Although there is not any technique developed to directly investigate the brain microstructure, studying the diffusion of water molecules in the tissue can reveal information about the underlying tissue microstructure and hence can provide an indirect method to capture the micro-structural information. Therefore, Diffusion Weighted Magnetic Resonance Imaging (DWI), which measures the diffusion of water molecules, has the capability to be used as a non-invasive method to study the microstructure of the brain and has been used in the past decade to achieve this purpose. The measurements based on DWI utilise model-based techniques to deduce the information about the tissue microstructure from the signal, which inherently suffer from bias error (as the data may not be derived from a member of the model class). However, they offer superior performance in variance minimisation, and allow the inference of parameters based on limited datasets.

In this work, we review a number of the existing model-based techniques developed to identify micro-structural parameters from DWI datasets. We present a critical analysis of different techniques in terms of their assumptions, advantages and drawbacks. In the next step, we compare the performance of different models in terms of their minimum uncertainty level. We utilise Cramer-Rao Lower Bound (CRLB) analysis to assess the minimum estimation error for different Diffusion Weighted Magnetic Resonance (DWMR) signal decay models. This includes the study of effect of optimisation of acquisition parameters on the performance of the models and identification of limiting factors to achieve higher performances. We demonstrate that, under typical measurement conditions, none of the models can provide parameter estimations with a reasonable uncertainty level. This will

show up in estimation algorithms that are extremely sensitive to parameter initial conditions, for example. At the end, we present a simulation framework to model the packing of the axons in the nerve bundles and to model the diffusion of water molecules in the tissue to construct simulation datasets and utilise them to investigate the validity of the models. We demonstrate that the sensitivity of models to initial conditions of the fitting algorithm is high and none of the models are capable of providing realistic estimations in general. Our analysis sheds a new light on methods that aim to infer microstructure from DWI data, and provides a method by which to assess the practicality of proposed techniques in the future.

Declaration

This is to certify that:

1. the thesis comprises only my original work towards the MPhil except where indicated in the Preface,
2. due acknowledgement has been made in the text to all other material used,
3. the thesis is less than 50,000 words in length, exclusive of tables, maps, bibliographies and appendices as approved by the Research Higher Degrees Committee.

Seyed Hamed Yousefi Mesri
March 12, 2014
Melbourne, Victoria, Australia

Preface

Figures 1.1, 1.2, 2.3, 2.6, 2.7 and 3.1 were used with permission from applicable sources. Figure 2.4 was provided by Australian Phenomics Network (APN), Histopathology and Organ Pathology.

Portions of the text in chapter 2 were modified with permission from Price et al. [1]. Portions of the text in chapter 3 were also modified with permission from applicable sources.

The idea of using Cramer-Rao Lower Bound (CRLB) analysis for evaluation of models of hindered/restricted diffusion in chapter 4 was proposed by Leigh Johnston and Iven Mareels. The design and implementation of the evaluation algorithm as well as defining the single figure of merit were done by myself and in collaboration with the proposers. I provided the computer codes to calculate the results and created the tables in chapter 4.

The dynamic and constructive axon packing algorithms in chapter 5 are of my own design and implementation as is the implementation of the multi-compartment simulation of Brownian motion of water molecules in the tissue models.

The appendix A was mainly adopted from the textbook by Liang et al. [2]. Appendix B was also adopted from the textbook by Price et al. [1].

Acknowledgements

First of all, I would like to thank my supervisor, Professor Iven Mareels at the Department of Electrical and Electronic Engineering, the University of Melbourne for his great guidance and many interesting and insightful discussions we had. I would also like to appreciate National ICT Australia, the Florey Institute of Neuroscience and Mental Health, and IBM Research Collaboratory for Life Sciences at Victorian Life Sciences Computation Initiative for their support and providing the equipment during my research in Melbourne.

Contents

List of Figures

List of Tables

Nomenclature

Δ	Diffusion time
δ	Gradient pulse duration
$\delta(.)$	Dirac Delta function
γ	Gyromagnetic ratio
$\Gamma(.)$	Gamma function
h	Planck's constant
k	Boltzmann's constant
ψ	Porosity
Υ	Surface relaxivity
ξ	Tortuosity
a	Characteristic distance of the geometry
ADC	Apparent Diffusion Coefficient
ADT	Apparent Diffusion Tensor
AWGN	Additive White Gaussian Noise
CHARMED	Composite Hindered And Restricted Model of Diffusion
CNS	Central Nervous System
CRLB	Cramer-Rao Lower Bound
CSF	Cerebrospinal Fluid
CT	Computed Tomography

DWI	Diffusion Weighted Magnetic Resonance Imaging
DWMR	Diffusion Weighted Magnetic Resonance
Eq.	Equation
FA	Fractional Anisotropy
FID	Free Induction Decay
GPD	Gaussian Phase Distribution
HARDI	High Angular Resolution Diffusion Imaging
ISF	Interstitial Fluid
MD	Mean Diffusivity
MMWMD	Minimal Model of White Matter Diffusion
MR	Magnetic Resonance
MRI	Magnetic Resonance Imaging
MSD	Mean Squared Displacement
NMR	Nuclear Magnetic Resonance
PDF	Probability Density Function
RA	Relative Anisotropy
RF	Radio Frequency
SGP	Short Gradient Pulse
VR	Volume Ratio

Chapter 1

Introduction

1.1 Introduction

The brain microstructure plays an important role in brain function and dysfunction. It has been shown that the brain diseases such as Alzheimer, multiple sclerosis and autism, are associated with altered physical structure of axons and myelin sheaths [3–7]. Figure 1.1 depicts the histological images of corticospinal tract axons in the spinal cord in healthy and multiple sclerosis affected tissues [8]. Figure 1.2 also illustrates the morphometric axonal analysis in mice optic nerves [9]. As it can be observed from the figures the size and density of the axons have been changed due to multiple sclerosis. The size change is more obvious in small fibres in comparison with large fibres [8]. It is also well known that the axon diameter in myelinated axons directly affects the nerve conduction velocity [10, 11].

Despite the great significance of the investigation of axon diameter distribution, the measurement of axon diameter distribution has only been performed using *ex vivo* histology. Although diagnostic imaging techniques promise to image internal organs, they cannot provide images of the axons due to the limitations in the spatial resolution. The axon diameters in the human brain ranges from 1 μm to 10 μm while for example a typical voxel size in Magnetic Resonance (MR) images is in the order of 100 μm along each dimension, which limits the capability of Magnetic Resonance Imaging (MRI) in identifying axon diameter distributions.

Over the last decade, there have been a number of efforts for indirect measurements of axon diameter distribution *in vivo* using Diffusion Weighted Magnetic Resonance Imaging (DWI). The main motivations behind the application of DWI for measuring the axon diameter distribution lies in the relationship between the changes in the diffusion patterns of water particles in the biological tissue due to underlying tissue microstructure.

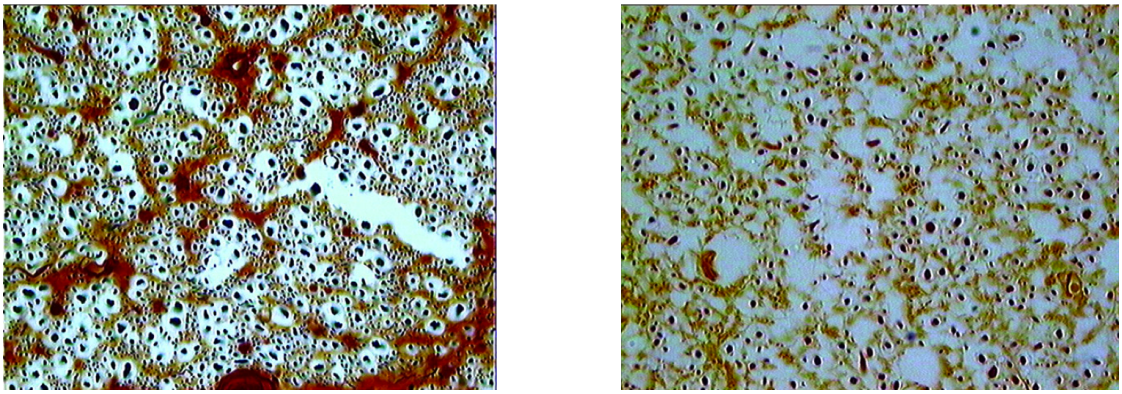

(a) (b)

Figure 1.1: Palmgren-stained transverse section of corticospinal tract axons in the spinal cord in (a) a control case and in (b) a case of multiple sclerosis photographed at 400 times magnification. There is a selective reduction in the density of small fibres compared with large fibres, which are relatively preserved; (Images modified from DeLuca et al., Brain 2004 [8]).

Water is a highly dynamic medium and water molecules continuously move and collide with each other and other molecules due to their thermal energy [12]. Hence, the investigation of self-diffusion of water molecules in the medium can reveal information about the underlying geometric structure. DWI measures the diffusion in tissues and can be used as a non-invasive method to study the microstructure of brain tissue [13]. Most techniques employ a model based approach trying to correlate the parameters of the model with the DWMR signal.

The questions addressed in this work can be summarised as follows:

1. What is the state of the art of the microstructure identification using DWI and what are the benefits and drawbacks of different techniques developed so far?

2. How to develop a theoretical framework to evaluate and compare different techniques?

3. Perform a numerical study of the different approaches using a single simulation framework.

4. What are the major obstacles these techniques encounter in clinical scanners and what are the practical solutions to overcome these obstacles?

Our main contributions are as follows:

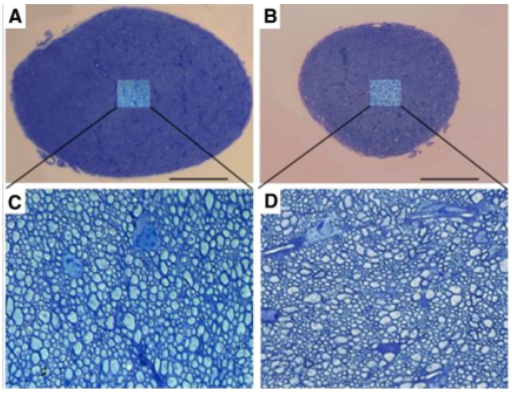

Figure 1.2: Morphometric axonal analysis in mouse optic nerve. Typical pre-chiasmal optic nerve cross-section stained with methylene blue from (A) healthy mouse and compared with (B) similar section from a mouse suffering from Multiple Sclerosis. Optic nerve size is reduced due to MS. (C and D) The central portions of methyleneblue stained cross-sections of pre-chiasmal optic nerves were photographed at 100 times magnification; (Images modified from Wu et al., Neuroimage 2007 [9]).

1. We present the physical and mathematical principles behind the derivation of different models.

2. We present all the models using similar notations to ease the comparison of different models.

3. We present a brief review over physical and mathematical principles of diffusion, DWI and the existing model-based techniques developed for interpreting the microstructural information from the DWI data.

4. We link different models to the mathematical derivations presented earlier and discuss different assumptions considered in derivation of their descriptions. We also analyse the limitations imposed by these assumptions on the applicability of the models.

5. We develop a single mathematical framework to analyse, evaluate and compare the performance of different models under similar practical conditions

6. We develop a simulation framework to model the placement of the axons inside the nerve bundles and resulting DWMR signals and utilise it to validate different models.

Performing these analyses and considering the practical acquisition parameters which can be achieved using the current scanners, we demonstrate that none of the models are able to produce estimations of the tissue microstructure parameters with a reasonable uncertainty level.

1.2 Outline of the thesis

In this chapter, we introduced the basic idea and motivations behind this work and provided the questions to be addressed through out this work. The outline of the thesis is as follows.

In chapter 2, first we introduce the diffusion process and present the physical principles related to it. This follows a discussion about different diffusion types according to different geometrical structures and time scales. This chapter also includes a brief review on the porous media and the diffusion process within them. We present the solution of the diffusion equation for some simple boundary conditions. The topics covered in this part, are used further on through this chapter to introduce the Nuclear Magnetic Resonance (NMR) based techniques to measure the diffusion properties of a medium. A clear understanding of the NMR based measurement techniques requires adequate knowledge about the NMR phenomenon and MRI. Here, we assume that the reader has an adequate knowledge about NMR physics and pulse sequences used for signal acquisition. A short review over NMR and MRI principles can also be found in Appendix A. In order to provide a clear understanding of the different methods used for relating the observed DWMR signal to the underlying geometrical structure, we review a number of approximations used to facilitate the modelling process. The understanding of these topics is crucial for a better understanding of the DWMR signal models in neural tissue, which are covered in the next chapter.

In chapter 3, a number of existing methods for modelling the DWMR signal decay in neural tissue is presented. The models are analysed and compared in terms of their assumptions and linked to the techniques and assumptions presented earlier in chapter 2. At the end of this chapter a summary of different models along with their characteristics is provided.

In chapter 4, we address the question of evaluating the performance of the models by using a mathematical framework based on Cramer-Rao Lower Bound (CRLB). We analyse the performance of a number of two compartment hindered/restricted models in terms of their minimum uncertainty level under practical acquisition conditions and compare the results. The effect of optimising the acquisition parameters (the measurement parameters which can be controlled on the scanner) on the performance is discussed together with an analysis of the practical limitations to achieve reasonable results. We demonstrate that none of the models could provide tissue related parameter estimates with reasonable uncertainty levels under practical conditions.

In chapter 5, we present a simulation framework for modelling the placement of the axons in a nerve bundle as well as the simulation of the Brownian motion of the water particles

in the neural tissue and the resultant DWMR signals. Next, we use the simulation data to analyse the validity of different models.

At the end, we provide a conclusive discussion about the work and the importance of its outcome on the research field, suggesting future work in order to address to remaining research questions.

Chapter 2

Diffusion Weighted Magnetic Resonance Imaging

Water molecules in the body exhibit random motions due to their thermal energy. These motions lead to random rotation and more importantly displacement of water particles from one position to another, which is called diffusion [14]. Although the nature of these displacements are completely random, they can provide some information about the geometry of the underlying medium through tracking the changes in the precession rate caused by the displacement of a particle in a nonuniform magnetic field, during a certain diffusion time. This is the basic idea behind DWI [12].

In this chapter, we study the physical principles of diffusion process and especially as it applies to brain tissue, and discuss the NMR techniques used to measure diffusion in brain tissue.

2.1 Physics of diffusion

Diffusion is one of the several transport phenomena in nature by which a matter is displaced as a result of thermally induced random molecular motions [15]. The concept of diffusion is closely related to the transfer of heat by conduction [16, 17]. This analogy was recognised first by Fick in 1855 who presented the mathematical equation of diffusion based on the mathematical theory for heat conduction derived earlier by Fourier in 1822 [16–19].

Based on Fick's second law, the diffusion of particles can be modelled using the diffusion equation as:

$$\frac{\partial c(\mathbf{r},t)}{\partial t} = \nabla \cdot [\mathbf{D}(\mathbf{r},t)\nabla c(\mathbf{r},t)] \tag{2.1}$$

where $c(\mathbf{r},t)$ and $\mathbf{D}(\mathbf{r},t)$ are the concentration density of the diffusing particles and the $(n \times n)$ diffusion tensor at location $\mathbf{r} = (x,y,z)$ and time t respectively and n is number of spatial dimensions [1,18]. In general the diffusion tensor in 3D Cartesian space can be represented by

$$\mathbf{D} = \begin{bmatrix} D_{xx} & D_{xy} & D_{xz} \\ D_{yx} & D_{yy} & D_{yz} \\ D_{zx} & D_{zy} & D_{zz} \end{bmatrix} \tag{2.2}$$

The associated diffusion matrix is symmetric and positive definite. In the case that $\mathbf{D}$ is isotropic and time-invariant, i.e. $\mathbf{D}(\mathbf{r},t) = D_0\mathbf{I}_n$, the diffusion equation, Eq. (2.1), can be written as:

$$\frac{\partial c(\mathbf{r},t)}{\partial t} = D_0\,\nabla^2 c(\mathbf{r},t) \tag{2.3}$$

which is known as the Fick's second law of diffusion [18]. Here, ∇^2 is the Laplacian operator

$$\nabla^2 = \left(\frac{\partial^2}{\partial x^2} + \frac{\partial^2}{\partial y^2} + \frac{\partial^2}{\partial z^2}\right) \tag{2.4}$$

Diffusivity is an intrinsic property of a medium. In general diffusivity depends on temperature, pressure, viscosity and the size of the diffusing particles [1, 20–22]. The higher the temperature, the more the energy of the particles and the faster the particles are moving [1,16,22]. As a result, increasing the temperature results in an increase in the diffusivity. On the other hand, if a medium is very viscous, the particles cannot move easily and the diffusivity decreases. The diffusion coefficient, D_0 [$\mathrm{m}^2.\mathrm{s}^{-1}$], assuming spherical particles is given by:

$$D_0 = \frac{kT}{6\pi\eta R_s} \tag{2.5}$$

where k [$\mathrm{m}^2.k\mathrm{g}.\mathrm{s}^{-2}.\mathrm{K}^{-1}$] is the Boltzmann's constant, T [K] is the temperature, η [$k\mathrm{g}.\mathrm{s}^{-1}.\mathrm{m}^{-1}$] is viscosity and R_s [m] is the effective hydrodynamic radius (i.e. Stokes radius) of diffusive particles. Eq. (2.5) is known as the Stokes-Einstein equation [1,20–23].

The diffusion propagator, $P(\mathbf{r}|\mathbf{r}_0,t)$, is used to analyse the diffusion of particles. It is defined as the (conditional) probability density of finding a particle starting initially at position $\mathbf{r}_0$ and ending up at position $\mathbf{r}$ after time t [1]. Since $P(\mathbf{r}|\mathbf{r}_0,t)$ is a probability density function (PDF) ,

$$\int_{-\infty}^{\infty} P(\mathbf{r}|\mathbf{r}_0,t)d\mathbf{r} = 1 \tag{2.6}$$

For the case of isotropic diffusion in homogeneous medium the diffusion propagator is independent of the initial position $\mathbf{r}_0$. However, in a heterogeneous system the displacement and hence the diffusion propagator depend on the initial position [1].

Since the spatial derivatives in the diffusion equation, Eq. (2.1), refer to the final position $\mathbf{r}$, the concentration of particles can be substituted using the diffusion propagator $P(\mathbf{r}|\mathbf{r}_0, t)$ as

$$\frac{\partial P(\mathbf{r}|\mathbf{r}_0, t)}{\partial t} = \nabla \cdot [\mathbf{D}(\mathbf{r}, t) \nabla P(\mathbf{r}|\mathbf{r}_0, t)] \tag{2.7}$$

with the initial condition

$$P(\mathbf{r}|\mathbf{r}_0, 0) = \delta(\mathbf{r} - \mathbf{r}_0) \tag{2.8}$$

where $\delta(.)$ is the dirac delta function . The solution of the diffusion equation Eq. (2.7) for a homogeneous system and time-invariant diffusion tensor, i.e. $\mathbf{D}(\mathbf{r}, t) = \mathbf{D}_0$ is

$$P(\mathbf{r}|\mathbf{r}_0, t) = \frac{1}{\sqrt{(4\pi t)^n |\mathbf{D}_0|}} \exp\left(-\frac{[\mathbf{r} - \mathbf{r}_0]^T \mathbf{D}_0^{-1} [\mathbf{r} - \mathbf{r}_0]}{4t}\right) \qquad \forall t > 0 \tag{2.9}$$

where the superscript $[.]^T$ denotes the vector transpose, $|\mathbf{D}_0|$ and $\mathbf{D}_0^{-1}$ denote the determinant and the inverse of the diffusion tensor respectively, and n is the number of spatial dimensions considered [1]. Eq. (2.9) demonstrates that for a homogeneous system with time-invariant diffusion tensor, the diffusion propagator can be modelled by a multivariate Gaussian distribution i.e. $P(\mathbf{r}|\mathbf{r}_0, t) \sim \mathcal{N}(\mathbf{r}_0, \mathbf{\Sigma})$ for which the covariance matrix,

$$\mathbf{\Sigma} = \begin{bmatrix} \sigma_x^2 & \sigma_x\sigma_y & \sigma_x\sigma_z \\ \sigma_x\sigma_y & \sigma_y^2 & \sigma_y\sigma_z \\ \sigma_x\sigma_z & \sigma_y\sigma_z & \sigma_z^2 \end{bmatrix} \tag{2.10}$$

is a positive, semi-definite matrix. It can be shown that:

$$\mathbf{\Sigma} = 2\mathbf{D}_0 t \qquad \forall t > 0 \tag{2.11}$$

For the particular case of isotropic and time-invariant diffusion tensor, $\mathbf{D}(\mathbf{r}, t) = D_0 \mathbf{I}_n$, the diffusion propagator is given by:

$$P(\mathbf{r}|\mathbf{r}_0, t) = \frac{1}{(4\pi D_0 t)^{n/2}} \exp\left(-\frac{|\mathbf{r} - \mathbf{r}_0|^2}{4D_0 t}\right) \quad , \quad \forall t > 0, \tag{2.12}$$

and the associated mean squared displacement (MSD) is calculated as:

$$\text{MSD}(t) = E\{|\mathbf{r} - \mathbf{r}_0|^2\} = \text{tr}(\mathbf{\Sigma}) = \text{tr}(2D_0\, \mathbf{I}_n\, t) = 2nD_0 t \quad , \quad \forall t > 0, \tag{2.13}$$

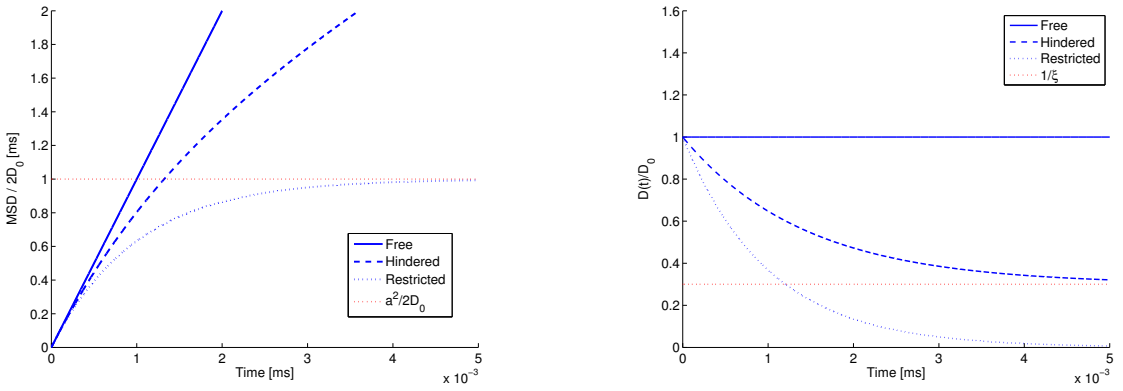

(a) (b)

Figure 2.1: Free, hindered and restricted diffusion in 1D. (a) Change of Mean square displacement (MSD) over time normalised to $2D_0$. (b) Change of the diffusivity over time normalised to D_0. The diffusivity in hindered diffusion is reduced due to porosity and tortuosity. The MSD becomes plateau in restricted diffusion in the long diffusion time regime and the diffusivity tends to zero. a denotes the pore radius and ξ denotes tortuosity; (Figure modified from Price 2009 [1]).

where $E\{.\}$ denotes the expected value and $\mathrm{tr}(\mathbf{\Sigma})$ denotes the trace of the covariance matrix. The mathematical derivation of the solution to the diffusion equation is presented in Appendix B. Eq. (2.12) indicates why the free diffusion of particles is called Gaussian diffusion. However, the diffusion of molecules in heterogeneous media is not isotropic in general and the diffusion may not be Gaussian. Moreover, if the diffusion is hindered by barriers or restricted in the medium, the diffusion tensor depends on the diffusion time and is not time-invariant [24]. In this case, the mean squared displacement is no longer linear in the diffusion time.

$$\mathrm{MSD}(t) = E\{|\mathbf{r} - \mathbf{r}_0|^2\} = \mathrm{tr}\left(2\int_0^t \mathbf{D}(\mathbf{r}, t')\, dt'\right) \tag{2.14}$$

A simple visualisation of free, hindered and restricted diffusion patterns and the resultant MSDs and time-dependent diffusion coefficients in 1D are presented in Figure 2.1.

The diffusion of particles is related to their thermal energy and at any temperature above absolute zero (0° K) the particles have random displacements. The greater the kinetic energy the faster the movements [23]. The random motion of suspended particles was first observed by Brown and as a result is referred to as Brownian motion [25]. In 1905, Einstein developed the mathematical expression for the Brownian motion and presented it as an indirect proof for the existence of molecules [26]. Brownian motion is a random walk process. A simple visualisation of Brownian motion of a particle by random walk in 2D is depicted in Figure 2.2. However, the expression of the variance and direction

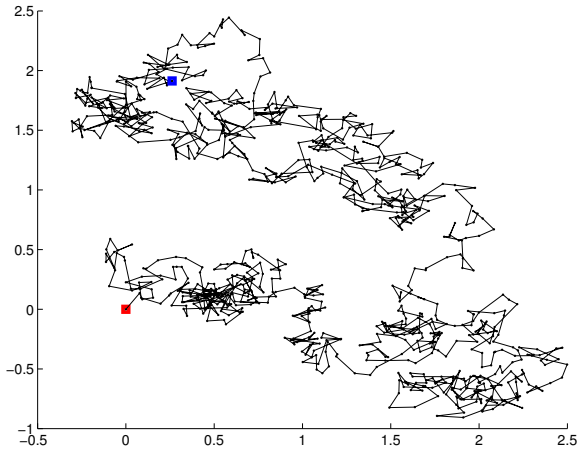

Figure 2.2: A simple visualisation of Brownian motion of a particle with random walk process. The start and end points are depicted by red and blue squares respectively.

of movements in general would be very complex. For the simple case of free isotropic diffusion in a homogeneous medium the movements are independent and the distribution of distances travelled by the particles after certain diffusion time t can be modelled by a Gaussian distribution as presented in Eq. (2.12).

The diffusion of molecules in heterogeneous media is not isotropic and will not be Gaussian in general. The inhomogeneities in the medium will result in the dependence of the diffusion propagator on the initial positions and the diffusion tensor will not be isotropic nor time-invariant. If the medium consists of non-mixing substances the mutual diffusivity will be zero and the boundaries of the spaces with different substance species will act as a barrier and the diffusion will be restricted.

2.2 Diffusion in isolated pores

In order to analyse the diffusion pattern of particles undergoing restricted diffusion, we first consider one of the most commonly used closed geometries. The structure of each geometry determines the boundary conditions for solving the diffusion equation. We present the derivation of propagators for the diffusion inside the isolated (single site) cylindrical pores. Here, we present the final mathematical descriptions. The mathematical derivations and analytical solutions of the diffusion equation for many geometries can be found in the literature [1, 15, 27–36].

2.2.1 Cylindrical pores

For diffusion in a cylindrical pore with radius a and reflective boundaries, the Neumann boundary condition is:

$$\left.\frac{\partial P}{\partial r}\right|_{r=a} = 0 \tag{2.15}$$

where $r = |\mathbf{r}|$. Solving the diffusion equation, the diffusion propagator is calculated as:

$$\begin{aligned} P(\mathbf{r}|\mathbf{r}_0, t) =& \frac{1}{\pi a^2} \\ &+ \sum_{n=1}^{\infty}\sum_{k=0}^{\infty}\left(\frac{2J_n(\beta_{nk}r_0)\,J_n(\beta_{nk}r)\,\cos(n\theta - n\theta_0)}{\pi a^2\left(1-\frac{n^2}{\beta_{nk}^2 a^2}\right)J_n(\beta_{nk}a)^2}\exp\left(-D_0\beta_{nk}^2 t\right)\right), \quad r \le a \end{aligned} \tag{2.16}$$

where n is an integer, θ is the angle between $\mathbf{r}$ and the plane perpendicular to the cylinder's main axis (similarly for θ_0 and $\mathbf{r}_0$) [1]. $J_n(.)$ is the n^{th} order Bessel function of the first kind and β_{nm} are the roots of the first derivative of the Bessel function i.e.

$$J_n'(\beta_{nk}a) = 0 \tag{2.17}$$

In the case of the parallel planes with relaxation boundaries, the Robin boundary condition is:

$$\left.(D_0\vec{n}\cdot\nabla P + \Upsilon P)\right|_{|x|=a} = 0 \tag{2.18}$$

where $\vec{n}$ is the surface normal and Υ is a positive constant denoting the surface relaxivity. The diffusion propagator is then given by:

$$\begin{aligned} P(\mathbf{r}|\mathbf{r}_0, t) =& \frac{1}{\pi a^2}\sum_{k=0}^{\infty}\frac{\beta_{0k}/J_0^2(\beta_{0k})}{\beta_{0k}^2 + (\Upsilon a/D_0)^2}J_0\left(\frac{\beta_{0k}r_0}{a}\right)J_0\left(\frac{\beta_{0k}r}{a}\right)\exp\left(-\frac{\beta_{0k}^2 D_0 t}{a^2}\right) \\ &+ \frac{2}{\pi a^2}\sum_{n=1}^{\infty}\sum_{k=0}^{\infty}\frac{\beta_{nk}^2/J_n^2\beta_{nk}}{\beta_{nk^2-n^2+(\Upsilon a/D_0)^2)}}J_n\left(\frac{\beta_{nk}r_0}{a}\right)J_n\left(\frac{\beta_{nk}r}{a}\right) \\ &\times\cos(n\theta_0)\,\cos(n\theta)\exp\left(-\frac{\beta_{nk}^2 D_0 t}{a^2}\right), \qquad r \le a \end{aligned} \tag{2.19}$$

2.3 Measurement time-scales and restricted diffusion

The time dependent diffusion coefficient for particles undergoing restricted diffusion is related to both time and geometries of the underlying medium [1]. To illustrate the effect

of restriction on the time-dependent diffusion, we consider restricted diffusion in a sphere with radius a and with an intrinsic diffusivity of the particles equal to D_0. In order to characterise the effect of diffusion time and geometric scale, we define the dimensionless parameter κ as

$$\kappa = \frac{D_0 \Delta}{a^2} \tag{2.20}$$

where D_0 is the intrinsic diffusivity of the medium and Δ is the diffusion time (the time at which we measure diffusion). Based on the value of κ three different cases can be identified:

2.3.1 Short diffusion time regime

In the short time diffusion limit, $\kappa \ll 1$, the particles does not travel far enough during diffusion time to interact with the boundaries and the diffusion can be considered free with the diffusion propagator described by Eq. (2.12). Hence, the measured diffusivity is independent of diffusion time and is equal to the intrinsic diffusivity of the particles i.e.

$$D(\Delta) = D_0 \tag{2.21}$$

and Mean squared displacement (MSD) is a linear function of time as given in Eq. (2.13) [1, 37].

2.3.2 Intermediate diffusion time regime

In the intermediate time regime, $\kappa \approx 1$, the particles start to interact with boundary. Hence the intermediate (transient) time regime is the cross-over regime of the short time limit to long-time limit [1]. The fraction of particles that interact with the boundaries is related to the surface to volume ratio (S_p/V_p) of the pore and the diffusion time (Δ) [28, 38–43]. Hence, the measured diffusivity, $D(\Delta, S_p/V_p)$, will be a function of diffusion time and Surface-to-Volume ratio as well and can be modelled as

$$\begin{aligned} D(\Delta, S_p/V_p) =& D_0 \Bigg[1 - \frac{4}{3n\sqrt{\pi}} \frac{S_p}{V_p} \sqrt{D_0 \Delta} - \frac{S_p}{2nV_p} \left(\frac{1}{2\bar{R}} - \frac{\Upsilon S_p}{V_p} \right) (D_0 \Delta) \\ &+ \frac{S_p}{V_p} O\left((D_0 \Delta)^{3/2} \right) \Bigg] \end{aligned} \tag{2.22}$$

where n is the spatial diminution (i.e. n = 1,2 or 3), $\bar{R}$ is the average principal radius of the curvature of the interface, Υ is the surface relaxivity and $O(.)$ denotes the higher order terms [28, 38–43].

As Δ increases the values for measured and intrinsic diffusivity diverge (Figure 2.1) because more particles interact with the boundaries. The MSD during this period is a non-linear function of diffusion time. Only the particles within the diffusion distance $\sqrt{D_0\Delta}$ will interact with the boundary. Hence, the higher order terms become more important at larger Δ since larger portion of the particles are affected. The time dependent diffusion at intermediate times is also called anomalous diffusion [1].

2.3.3 Long diffusion time regime

In the long time regime, $\kappa \gg 1$, all the diffusive particles interact with the boundaries and as a result the MSD of particles is a constant, independent of the diffusion time and equal to squared radius of the pore (a^2),

$$\mathrm{MSD}(\Delta) = a^2 \tag{2.23}$$

for a sphere with perfectly reflecting boundaries (i.e. $\Upsilon = 0$) [1, 44]. Therefore, in the long time regime, the MSD reflects the shape, dimension and orientation of the restricting geometry. This can be seen by calculating the limit of the diffusion propagator for cylindrical boundaries given in Eq. (2.16) when $t \to \infty$, which results only in the first terms arising from zero eigenvalue. Hence, the particles trapped in a closed pore, at long diffusion time lose the dependencies to their initial point and their final positions become independent of their starting points [1]. Similarly, for the case of diffusion with radiative boundaries, the second and third terms in the diffusion propagator Eq. (2.19) tend to zero.

2.4 Diffusion in porous media

A porous medium is an impermeable frame containing pores. Porous media are found in nature for example in rocks and biological tissues such as bone and brain. They also can be found in man-made materials like foams, cellulose fibres, concentrated emulsions and ceramics. The properties of porous media have been studied comprehensively in different disciplines like petroleum engineering, material science and biophysics [1, 45].

A porous medium consists of at least two phases (a) a porous matrix and (b) the pore space filled with a liquid or gas. Most porous media have disordered morphology and the determination of the interface between pore space and the matrix is complicated. The transport and thermodynamic properties of fluids in porous media are closely related to the size and connectivity of the pores [1,46]. Porosity (ψ) is defined as the volume fraction

of the pore space as:

$$\psi = \frac{V_p}{V} \tag{2.24}$$

where V_p is the volume of the pore space and V denotes the total volume of the sample [1]. Most porous media consist of interconnected pores (an open geometry) and the diffusive particles can move around the boundaries. In general, the characterisation of diffusion is more complicated in pores than in the free diffusion case. In contrast to impermeable pores, where the time dependent diffusivity $D(t)$ tend to zero, in material containing interconnected media the time dependent diffusivity decreases to a plateau value D_∞ determining the long range connectivity of the medium [1, 42, 47–49]. The inter-connectivity of a porous medium is determined by tortuosity (ξ) defined as

$$\xi = \frac{D_0}{D_\infty} \tag{2.25}$$

which indicates the average hindrance of a complex medium relative to an obstacle-free medium and can be interpreted as a path-length multiplication factor for particles to find their way around the obstacles. Tortuosity is a measure of a part of specific surface by diffusing particles before they lose the memory about the orientation of the surface at initial position and hence indicates the connectivity and curvature of the surfaces in porous media [1, 42, 47, 48, 50–53]. The identification of tortuosity has been used widely in the past as an important characteristic to understand several processes in the brain [1, 54, 55]. Tortuosity can be calculated for uniform colloidal objects and periodic porous mediums. However, the calculation of tortuosity in complex systems like biological tissue would be difficult and can only be determined experimentally [1, 53, 55, 56].

Based on the discussion above, it could be concluded that the diffusion in complex and disordered media (e.g biological tissue), is not free in general due to restrictions and hindrances by the boundaries and interconnected pores and as a result the diffusion cannot be determined a by Gaussian Propagator. Therefore, more advanced modelling techniques are required to identify the diffusion characteristics of molecules in the complex systems.

2.5 Diffusion in the brain white matter

Diffusion plays an important role in brain functioning. Glucose and oxygen are delivered from the vascular system into the brain cells by diffusion. Diffusion also facilitates the transportation of hormones, ions and in general cell signalling substances [54, 57–59].

The building blocks of the central nervous system are neurons which receive, process and transmit information through electrical-chemical signals. The neurons consist of a cell

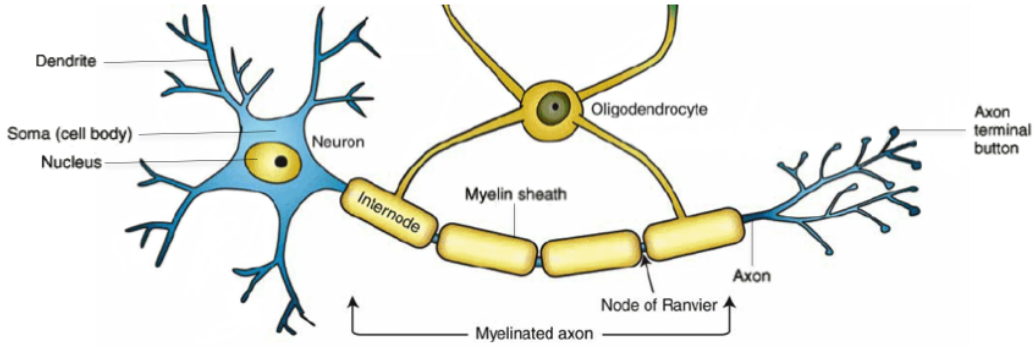

Figure 2.3: A simple representation of cellular components of neurons in the brain (Figure modified from Edgar and Griffiths 2009 [60]).

body or soma, dendrites and an axon. A simple representation of a neuron is depicted in Figure 2.3. Dendrites receive the signal from other neurons and deliver it to the soma. The soma transmits a signal through its axon. The axons can be very long in comparison to the soma. Long axons are usually insulated in a fatty myelin sheath. The myelination of axons increase the speed of signal transmission through the axons. If the myelin of an axons degrades, the conduction of signals through the nerve can be impaired or lost. The axon diameter in the central nervous system (CNS) is typically about $1[\mu\text{m}]$. However, depending on the degree of myelination, the axon diameter can be as much as $10[\mu\text{m}]$ [61].

The axons in the CNS are bundled together in fibre tracts or fasciculi. Figure 2.4 depicts the myelinated nerve bundles. The cell bodies and dendrites are placed in the grey matter at the cerebral cortex and the myelinated axons are placed in the white matter connecting different functional areas of the cortex. As a result, the white matter produces high intensities in T_1 weighted MR imaging as depicted in Figure 2.5. Besides the grey and white matter, there are also a number of cavities filled with the cerebrospinal fluid (CSF) [60].

The axons within the fibre tracts are surrounded by extracellular space which contains interstitial fluid (ISF). The ISF is in contact with CSF at the ventricular surfaces. The main transport mechanism in the extracellular space is diffusion and extensive studies have established that the extracellular space acts like a porous medium for diffusion of particles [54, 58]. This assumption makes it possible to describe the diffusion processes in the brain using the established theory of diffusion in porous media developed in other disciplines introduced previously [54, 62].

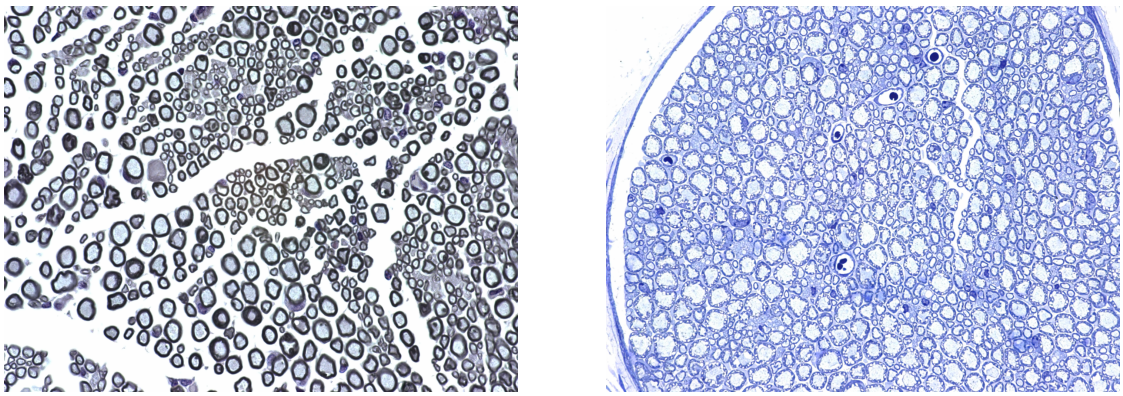

(a) (b)

Figure 2.4: Sciatic Nerve bundle of mouse Photographed at 40 times magnification. Tissue fixed in 2.5% glutaraldehyde. (a) Myelinated nerves. The black circles around the axons are myelin sheath. Postfixation with 1% Osmium tetroxides. Tissue was resin embedded and sectioned at 1μm on an ultramicrotome. (b) Myelinated nerve bundle. The axons are packed in a nerve bundle. Tissue stained with 1% Toluidine Blue. (Photo credit: Australian Phenomics Network (APN), Histopathology and Organ Pathology)

2.6 Diffusion Weighted Magnetic Resonance measurement

The measurement of the diffusion is performed using several methods including NMR [63–69], light scattering [70, 71], neutron scattering [72], capacity intermittent titration techniques (CITT) [73], capillary methods, florescence [74, 75], attenuated total reflection infrared spectroscopy (ATRIR) [76] and centrifuge studies [77]. The application of non-NMR methods are generally limited because they are quite tedious and usually invasive [1, 20, 78]. On the other hand, due to non-invasive nature and not requiring labelled probe molecules, NMR based techniques are used widely in studying diffusion of molecules in chemical and biological systems. NMR methods also utilise the non-ionising magnetic fields to acquire signals, and have much lower health concerns in comparison with the other imaging techniques such as conventional X-Ray imaging and Computed Tomography (CT)-scan, which use hazardous ionising radiations to capture the image. As a result, NMR based techniques are well suited for medical diagnostics applications.

2.6.1 Bloch-Torrey equations

The effect of diffusion on the MR signal was presented by Hahn in 1950 [63], Carr and Purcell in 1954 [64] and Woessner in 1961 [65]. Hahn described that diffusion of spins in a nonuniform magnetic field contributes to the decay of transverse magnetisation [79]. Based

on the Fick's second law given by Eq. (2.1), the self-diffusion of spins can be modelled by:

$$\frac{\partial \vec{M}}{\partial t} = \nabla \cdot \left[\mathbf{D}(\mathbf{r}, t)\, \nabla \vec{M} \right] \tag{2.26}$$

where $\mathbf{D}$ is the time dependent diffusion tensor of the medium and $\vec{M}$ is the bulk magnetisation vector (see Appendix A) [1]. Torrey [80], showed that in order to take the effect of diffusion on the transverse magnetisation vector, the term related to diffusion of particles should be added to the right hand side of the original Bloch equations [81] (see Appendix A) resulting in

$$\frac{\partial \vec{M}}{\partial t} = 2\pi\gamma\, \vec{M} \times \vec{B} - \frac{M_x \vec{i} + M_y \vec{j}}{T_2} - \frac{(M_z - M_0)\, \vec{k}}{T_1} + \nabla \cdot \left[\mathbf{D}(\mathbf{r}, t) \nabla\, \vec{M} \right] \tag{2.27}$$

where γ [MHzT^{-1}] is the gyromagnetic ratio, $\vec{B}$ [T] is the total magnetic field, and T_1 [s] and T_2 [s] are spin-lattice and spin-spin relaxation time constants respectively. M_x, M_y and M_z are the components of the bulk magnetisation vector parallel to unit vectors $\vec{i}$, $\vec{j}$ and $\vec{k}$ respectively [80].

Eq. (2.27) is called Bloch-Torrey equation and describes the complete equation of magnetisation vector by taking the effect of diffusion of spins into account. In the case of a homogeneous medium and isotropic diffusion, the diffusion tensor $\mathbf{D}(\mathbf{r}, t) = D_0 \mathbf{I}_n$ and Fick's second law of diffusion is reduced to Eq. (2.3). Hence, the Bloch-Torrey equation for the particular case of isotropic diffusion and homogeneous medium can be written as:

$$\frac{\partial \vec{M}}{\partial t} = 2\pi\gamma\, \vec{M} \times \vec{B} - \frac{M_x \vec{i} + M_y \vec{j}}{T_2} - \frac{(M_z - M_0)\, \vec{k}}{T_1} + D_0 \nabla^2 \vec{M} \tag{2.28}$$

Considering a constant magnetic field gradient, $\vec{G}(t)$ [Tm^{-1}], the total magnetic field is given by the sum of constant and gradient terms:

$$\vec{B} = (B_0 + \vec{G}(t) \cdot \mathbf{r}(t))\vec{k} \tag{2.29}$$

where $\vec{k}$ is the unit vector in z direction. Hence, the Bloch-Torrey equations in transverse plane and rotating frame (the coordinate system which rotates with angular frequency $\vec{\omega} = \omega_0 \vec{k}$, see Appendix A) can be written as:

$$\begin{cases} \dfrac{\partial M_{x'}(\mathbf{r}, t)}{\partial t} = -\dfrac{M_{x'}(\mathbf{r}, t)}{T_2} + 2\pi\gamma \vec{G}(t) \cdot \mathbf{r}(t) M_{y'}(\mathbf{r}, t) + D_0 \nabla'^2 M_{x'}(\mathbf{r}, t) \\ \dfrac{\partial M_{y'}(\mathbf{r}, t)}{\partial t} = -\dfrac{M_{y'}(\mathbf{r}, t)}{T_2} - 2\pi\gamma \vec{G}(t) \cdot \mathbf{r}(t) M_{x'}(\mathbf{r}, t) + D_0 \nabla'^2 M_{y'}(\mathbf{r}, t) \end{cases} \tag{2.30}$$

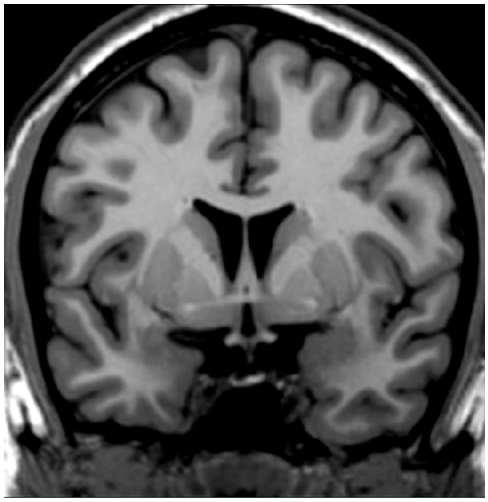

Figure 2.5: T_1 weighted coronal MR image of the brain

Here ∇'^2 is the Laplacian operator in the rotating frame defined as:

$$\nabla'^2 = \left(\frac{\partial^2}{\partial x'^2} + \frac{\partial^2}{\partial y'^2} + \frac{\partial^2}{\partial z'^2}\right) \tag{2.31}$$

Using complex notation $M_{x'y'}(\mathbf{r},t) = M_{x'}(\mathbf{r},t) + \mathrm{j}M_{y'}(\mathbf{r},t)$ to show the transverse component of the bulk magnetisation, the Bloch-Torrey equation in transverse plane can be written as:

$$\frac{\partial M_{xy}(\mathbf{r},t)}{\partial t} = -\frac{M_{xy}(\mathbf{r},t)}{T_2} - \mathrm{j}\left(\omega_0 + 2\pi\gamma\vec{G}(t)\cdot\mathbf{r}(t)\right)M_{xy}(\mathbf{r},t) + D_0\nabla'^2 M_{xy}(\mathbf{r},t) \tag{2.32}$$

The solutions for the equation above at time t is in the form:

$$M_{xy}(\mathbf{r},t) = M_{xy}(\mathbf{r},0^+)\, f(t)\, \exp\left[-\frac{t}{T_2} - \mathrm{j}\left(\omega_0 t + 2\pi\gamma\int_0^t \vec{G}(t')\cdot\mathbf{r}dt'\right)\right] \tag{2.33}$$

where $M_{xy}(\mathbf{r},0^+)$ is the magnitude of transverse magnetisation vector immediately after the RF excitation pulse and $f(t)$ is an unknown function depicting the effect of the diffusion on the transverse magnetisation [79, 82]. Taking derivative of Eq. (2.33) with respect to time, we can write

$$\begin{aligned}\frac{\partial M_{xy}(\mathbf{r},t)}{\partial t} = M_{xy}(\mathbf{r},0^+)\, \exp\left[-\frac{t}{T_2} - \mathrm{j}\left(\omega_0 t + 2\pi\gamma\int_0^t \vec{G}(t')\cdot\mathbf{r}dt'\right)\right]\times \\ \left[\frac{df(t)}{dt} + \left(-\frac{1}{T_2} - \mathrm{j}(\omega_0 + 2\pi\gamma\vec{G}(t')\cdot\mathbf{r}(t)\right)f(t)\right]\end{aligned} \tag{2.34}$$

Substituting Eq. (2.33) and Eq. (2.34) into Eq. (2.32) we have

$$\frac{df(t)}{dt}\exp\left[-\frac{t}{T_2}-\mathrm{j}\left(\omega_0 t+2\pi\gamma\int_0^t\vec{G}(t')\cdot\mathbf{r}dt'\right)\right]= D_0\,f(t)\,\nabla^2\exp\left[-\frac{t}{T_2}-\mathrm{j}\left(\omega_0 t+2\pi\gamma\int_0^t\vec{G}(t')\cdot\mathbf{r}dt'\right)\right] \tag{2.35}$$

Considering a structurally homogeneous system, and

$$\begin{aligned}&\nabla^2\exp\left[-\frac{t}{T_2}-\mathrm{j}\left(\omega_0 t+2\pi\gamma\int_0^t\vec{G}(t')\cdot\mathbf{r}dt'\right)\right]\\&=\frac{\partial}{\partial\mathbf{r}}\cdot\frac{\partial}{\partial\mathbf{r}}\exp\left[-\frac{t}{T_2}-\mathrm{j}\left(\omega_0 t+2\pi\gamma\int_0^t\vec{G}(t')\cdot\mathbf{r}dt'\right)\right]\\&=4\pi^2\left[\gamma\int_0^t\vec{G}(t')dt'\right]^T\left[\gamma\int_0^t\vec{G}(t')dt'\right]\times\\&\qquad\exp\left[-\frac{t}{T_2}-\mathrm{j}\left(\omega_0 t+2\pi\gamma\int_0^t\vec{G}(t')\cdot\mathbf{r}dt'\right)\right]\end{aligned} \tag{2.36}$$

the Eq. (2.35) can be written as

$$\begin{aligned}\frac{df(t)}{dt}&=4\pi^2\left[\gamma\int_0^t\vec{G}(t')dt'\right]^T D_0\,f(t)\left[\gamma\int_0^t\vec{G}(t')dt'\right]\\&=4\pi^2\,\mathbf{q}^T D_0\,f(t)\,\mathbf{q}\end{aligned} \tag{2.37}$$

where $\mathbf{q}$ [m^{-1}] is a vector defined as:

$$\mathbf{q}(t)=\gamma\int_0^t\vec{G}(t')dt' \tag{2.38}$$

and $\mathbf{q}^T$ denotes the transpose of $\mathbf{q}$. Therefore, the function $f(t)$ by considering $f(0)=1$ can be calculated as:

$$f(t)=\exp\left(-b\,D_0\right) \tag{2.39}$$

where

$$\begin{aligned}b(t)&=4\pi^2\int_0^t\left[\gamma\int_0^{t'}\vec{G}(t'')dt''\right]^T\left[\gamma\int_0^{t'}\vec{G}(t'')dt''\right]dt'\\&=4\pi^2\int_0^t\mathbf{q}^T(t')\mathbf{q}(t')\,dt'\end{aligned} \tag{2.40}$$

is the diffusion weighting factor, which incorporates the gradient pulse characteristics [45, 79].

Using Eq. (2.33) and considering the equation for MR signal (see Appendix A), the MR signal in presence of diffusion weighting gradient field can be written as:

$$S(b,t) = S_0(t)\exp\left(-b\,D_0\right) \tag{2.41}$$

where $S_0(t) = S(0,t)$ is the MR signal in the absence of diffusion encoding gradients (i.e. $\vec{G}(t) = 0$). Eq. (2.41) describes the effect of diffusion on the attenuation of the MR signal. One can always use Eq. (2.41) to estimate the Apparent Diffusion Coefficient (ADC) by measuring the signal first without a gradient field ($b = 0$) and then in the presence of a gradient field $\vec{G}$ (certain b value).

In order to cancel the effects of the field inhomogeneity and T_2 effect, the diffusion signal in Eq. (2.41) is normalised by $S_0(t)$. Therefore, the normalised DWMR signal attenuation due to diffusion can be presented as:

$$x(b) = \frac{S(b,t)}{S_0(t)} = \exp\left(-b\,D_0\right) \tag{2.42}$$

2.6.2 Stejskal-Tanner Pulsed Gradient Spin Echo sequence

Although the earlier DWMR measurements were performed using a continuos and steady field gradients [63, 64, 80], the NMR diffusion measurement became more populated in 1960s by the introduction of a single-PGSE sequence known as Stejskal-Tanner method [66, 67, 69, 83]. This technique utilises a measurement setup consisting of two symmetric diffusion encoding and decoding gradient pulses with duration (δ) and separated by diffusion time (Δ) to sensitise the received MR signal to the diffusion of particles. The gradient pulses are placed in either side of refocusing 180° pulse as depicted in Figure 2.6. The acquisition parameters (which can be set on scanner) for a single-PGSE sequence are diffusion sensitising gradient field amplitude and direction ($\vec{G}$), gradient pulse duration (δ) and diffusion time (Δ).

Based on the measurement setup, during the first gradient pulse, spins acquire phase shifts proportional to the initial positions of the molecules in the direction of the gradient. The second gradient pulse applied after a 180° RF refocusing pulse, shifts back the phase of particles proportional to their final position [66, 85]. If a particle does not move between two pulses (the diffusion time), the phase shifts during the first and second pulses will cancel out each other completely and the spins become completely refocused at echo time.

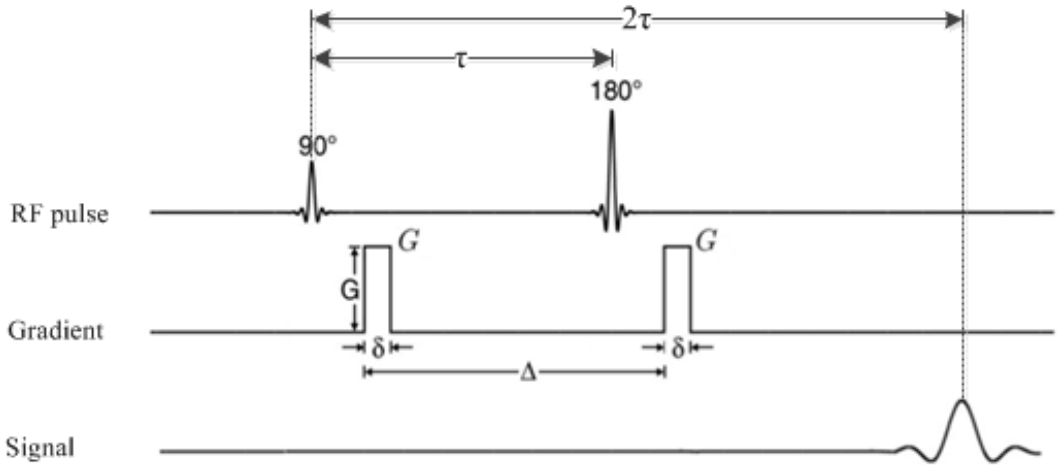

Figure 2.6: Stejskal-Tanner pulse sequence employed to sensitise the MR signal to molecular diffusion. Characteristic parameters of the waveform are the gradient amplitude (G), the diffusion time (Δ) and the gradient pulse width (δ). The encoding (first) and decoding (second) gradient pulses are separated by a 180° refocusing RF pulse (Figure modified from Yablonskiy et al., NMR in biomedicine 2010 [84]).

However, if particles move during the diffusion time, there will be a remaining phase offset related to the displacements during this period. The accumulated phase offset of a single particle (i-th particle) at echo time 2τ after the RF excitation pulse can be calculated as:

$$\varphi_i(\mathbf{r}_i, 2\tau) = 2\pi\gamma \left[\int_0^{\tau} \vec{G}(t) \cdot \mathbf{r}_i(t)\, dt - \int_{\tau}^{2\tau} \vec{G}(t) \cdot \mathbf{r}_i(t)\, dt \right] \tag{2.43}$$

where $\mathbf{r}_i(t)$ [m] is the position of the i-th spin at time t [s] and $\vec{G}(t)$ [T.m^{-1}] is the diffusion sensitising gradient waveform. γ [Hz.T^{-1}] is the gyromagnetic ratio and 2τ [s] is the echo time. Due to the dot product in Eq. (2.43), only the component of motion in the direction of the gradient will contribute to a change in the phase of the spin [1]. The diffusion weighting factor for single-PGSE sequence using Eq. (2.40) at echo time (2τ) can be calculated as:

$$b(2\tau) = 4\pi^2\gamma^2 G^2 \left(\Delta - \frac{\delta}{3}\right) = 4\pi^2 \mathbf{q}^T \mathbf{q} \left(\Delta - \frac{\delta}{3}\right) \tag{2.44}$$

where $\mathbf{q}$ [m^{-1}] is determined using a set of acquisition parameters as:

$$\mathbf{q} = \gamma \vec{G} \delta \tag{2.45}$$

and $\mathbf{q}^T$ denotes the transpose of $\mathbf{q}$. The signal at echo time (2τ) can be calculated using

Eq. (2.41) as

$$S(\mathbf{q}, \Delta, 2\tau) = S_0(2\tau) \exp\left[-4\pi^2 \mathbf{q}^T D_0\, \mathbf{q} \left(\Delta - \frac{\delta}{3}\right)\right] \tag{2.46}$$

where $S_0(2\tau) = S(0, \Delta, 2\tau)$ is the signal at echo time in the absence of diffusion sensitising gradient. The normalised DWMR signal at echo time is:

$$x(\mathbf{q}, \Delta) = \frac{S(\mathbf{q}, \Delta, 2\tau)}{S_0(2\tau)} = \exp\left[-4\pi^2 \mathbf{q}^T D_0\, \mathbf{q} \left(\Delta - \frac{\delta}{3}\right)\right] \tag{2.47}$$

For the case of continous gradients, $\delta = \Delta = \tau$, and Eq. (2.46) and Eq. (2.47) reduce to

$$S(G, 2\tau) = S_0(2\tau) \exp\left(-4\pi^2 \gamma^2 G^2 D_0 \frac{2\tau^3}{3}\right) \tag{2.48}$$

$$x(G, 2\tau) = \frac{S(G, 2\tau)}{S(0, 2\tau)} = \exp\left(-4\pi^2 \gamma^2 G^2 D_0 \frac{2\tau^3}{3}\right) \tag{2.49}$$

which are the well-known expressions for Hahn spin-echo signal in the presence of a continous gradient field G [1].

It should also be noted that the analysis presented above is performed by solving the Bloch-Torrey equations under the assumption of free and Gaussian diffusion profile for the particles in a homogeneous system with an isotropic and time-invariant diffusion tensor, i.e. $\mathbf{D}(\mathbf{r}, t) = D_0 \mathbf{I}_n$. Therefore, Eq. (2.42), Eq. (2.47) and Eq. (2.49) are only valid under the assumption of free isotropic diffusion. In general case of anisotropic and hindered/restricted diffusion, the diffusion tensor will be time dependent and the signal definition would be more complex.

2.6.3 Linking the Diffusion Weighted MR signal to diffusion

As it was mentioned earlier, the diffusion profile of water molecules in a heterogeneous medium is not Gaussian in general and depends on the underlying geometry. A complete analysis of the resultant DWMR signal requires solving the Bloch-Torrey equations. However, the analytical solutions to Bloch-Torrey equations is quite time consuming and is possible only for a number of simple geometries. Although, these equations can be solved using numerical methods by having a priori knowledge about the geometrical structure of the underlying medium, in most cases this a priori information is not available which makes the application of this technique impossible in practice. On the other hand, we are usually interested in determining the underlying geometrical structure from the measured signals and hence instead of solving the forward problem by applying a priori knowledge to

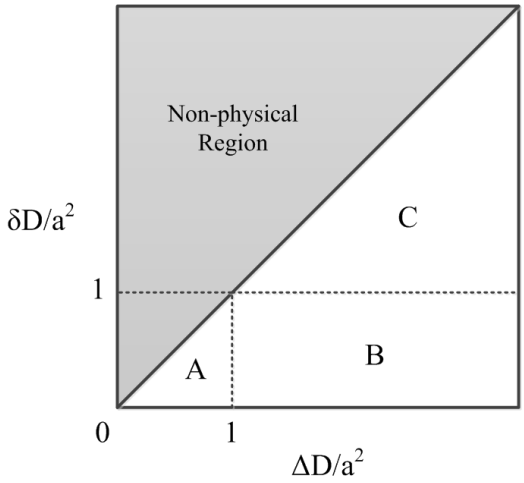

Figure 2.7: Conceptual regions of δ vs Δ in terms of $\delta D/a^2$ and $\Delta D/a^2$. There are three regions which can be identified according to the durations of δ and Δ compared to the characteristic time a^2/D required to travel to a barrier. Region A: Unrestricted diffusion, where $\Delta D/a^2 \ll 1$. Region B: Restricted diffusion where $\delta D/a^2 \ll 1 \ll \Delta D/a^2$. Region C: Rapid-diffusion where $\delta D/a^2 \gg 1$. The line $\delta = \Delta$ denotes the steady gradient case. The sizes of the regions indicated are exaggerated; (Figure modified from Wang et al., Journal of Magnetic Resonance 1995 [83]).

determine the resultant signal, we are interested in solving the inverse problem to predict the underlying microstructure from a set of measurement data. This is particularly of more interest, since it can reveal information about the microstructure in spatial scales much smaller than the resolutions, which can be achieved by conventional MRI techniques [1,86].

There have been a number of techniques developed to correlate the measured DWMR signal decay to the underlying diffusion process by considering certain approximations. The validity of these approximations mainly depends on the timing of the diffusion sensitising gradients with respect to the characteristic time of the underlying geometry. Figure 2.7 depicts the regions of gradient pulse duration δ and diffusion time Δ with respect to the characteristic time of the geometry, a^2/D, which is the time needed for a particle to travel to the boundary [83]. a represents the characteristic distance of the geometry (i. e. radius of the pore or half the distance between two parallel planes).

Three regions can be identified as:

A. Unrestricted diffusion, where $\Delta D/a^2 \ll 1$. The diffusion time Δ is so short that only particles in vicinity of the boundaries can interact with the boundaries. Hence, diffusion of particles in this region can be considered as free. This is identical to short diffusion time regime (see section 2.3.1).

B. Restricted diffusion, where $\Delta D/a^2 \gg 1$ but $\delta D/a^2 \ll 1$. The diffusion time Δ is long

enough so many particles encounter interactions with the boundaries. On the other hand, since the gradient pulse duration δ is relatively short with respect or diffusion time, i. e. $\delta \ll \Delta$, the diffusion of particles during the application of gradient pulses can be neglected and the signal attenuation can merely be linked to the diffusion of particles during the time interval $(\Delta - \delta)$.

C. Rapid diffusion, where $\delta D/a^2 \gg 1$. The spins have many wall encounters even during the gradient pulse application. Hence the diffusion of particles during the gradient pulses cannot be neglected [83]. The 45° line denotes the case where $\delta = \Delta$, which corresponds to application of continuous (steady) gradient as considered by Robertson [87] and Neuman [88].

2.6.4 Gaussian Phase Distribution Approximation

One of the commonly used approximations used to link the DWMR signal decay to diffusion process is Gaussian Phase Distribution (GPD) or Gaussian phase approximation.

The total phase offset of a single particle due to diffusion and at the end of the PGSE sequence is given by Eq. (2.43). GPD assumes that the distribution of phase offsets can be modelled by a Gaussian PDF as

$$P(\varphi, 2\tau) = \frac{1}{\sqrt{2\pi\sigma_\varphi^2}} \exp\left(-\frac{\varphi^2}{2\sigma_\varphi^2}\right) \tag{2.50}$$

where σ_φ^2 denotes the phase variance at the end of the pulse sequence and can be calculated for Hahn Spin Echo sequence [63] as:

$$\begin{aligned}
\sigma_\varphi^2 &= E\left\{\varphi^2\right\} \\
&= 4\pi^2\gamma^2 E\left\{\left[\int_0^\tau \vec{G}(t)\cdot\mathbf{r}(t)\,dt - \int_\tau^{2\tau} \vec{G}(t)\cdot\mathbf{r}(t)\,dt\right]^2\right\} \\
&= 4\pi^2\gamma^2\left[\int_0^\tau G(t)dt\int_0^\tau G(t')dt' - 2\int_0^\tau G(t)dt\int_\tau^{2\tau} G(t')dt' + \int_\tau^{2\tau} G(t)dt\int_\tau^{2\tau} G(t')dt'\right] \\
&\quad \times E\left\{r_G(t)r_G(t')\right\}
\end{aligned} \tag{2.51}$$

where r_G denotes the displacement in the direction of gradient field $\vec{G}$, τ is half the echo time and $E\{\cdot\}$ denotes the expectation operator. $E\left\{r_G(t)r_G(t')\right\}$ is expressed as the products of the probability of each motion times the corresponding displacement in the direction of the gradient, which is given by

$$E\left\{r_G(t)r_G(t')\right\} = \iiint (r_1 - r_0)_G\,(r_2 - r_0)_G\,\rho(\mathbf{r}_0)\,P(\mathbf{r}_1|\mathbf{r}_0,t)\,P(\mathbf{r}_2|\mathbf{r}_0,t'-t)\,d\mathbf{r}_0\,d\mathbf{r}_1\,\mathbf{r}_2 \qquad t' > t \tag{2.52}$$

where subscript $(.)_G$ denotes the component of the displacement in the direction of the gradient field $\vec{G}$ [1, 88–90]. Substituting Eq. (2.12) for the case of isotropic free diffusion and setting $n = 1$ for single gradient field direction, we have

$$E\left\{r_G(t)r_G(t')\right\} = 2D_0 t \tag{2.53}$$

which is the same expression for MSD given in Eq. (2.13) [1, 89].

In order for the signal to be detected, there must be enough phase coherence of the magnetisation. In a structurally homogenous system, the attenuation of DWMR signal due to diffusion related phase offset distribution, $P(\varphi, 2\tau)$ is given by

$$x(2\tau) = \int_{-\infty}^{\infty} P(\varphi, 2\tau)\exp(\mathrm{j}\varphi)d\varphi \tag{2.54}$$

where $P(\varphi, 2\tau)$ is the probability density function of the phase offsets at the end of the pulse sequence and

$$\int_{-\infty}^{\infty} P(\varphi, 2\tau)d\varphi = 1 \tag{2.55}$$

Eq. (2.54) depicts the Fourier relationship between distribution of diffusion related phase offsets and DWMR signal attenuation.

Substituting Eq. (2.53) into Eq. (2.51), the phase variance is calculated as:

$$\sigma_\varphi^2 = 8\pi^2\gamma^2 G^2\delta^2 D_0\,(\Delta - \delta/3) \tag{2.56}$$

and the signal decay due to diffusion using Eq. (2.50) and Eq. (2.54) is given by

$$\begin{aligned} x(G, 2\tau) &= \exp\left(-\frac{\sigma_\varphi^2}{2}\right) \\ &= \exp\left(-4\pi^2\gamma^2 G^2\delta^2 D_0\,(\Delta - \delta/3)\right) \end{aligned} \tag{2.57}$$

which agrees with the Eq. (2.47) derived by solving Bloch-Torrey equations.

For the case of diffusion inside a cylinder with radius a and the diffusion propagator given in Eq. (2.16), and by assuming diffusion perpendicular to the cylinder's main axis ($\theta = \pi/2$), the DWMR signal decay using GPD approximation is calculated as

$$x(G,2\tau) = \exp\left\{ -\frac{8\pi^2\gamma^2G^2}{D_0^2}\sum_{n=1}^{\infty}\frac{2\beta_n^2D_0\delta - 2 + 2f(\delta) - f(\Delta-\delta) + 2f(\Delta) - f(\Delta-\delta)}{\beta_n^6\left(\beta_n^2a^2-1\right)}\right\} \tag{2.58}$$

where

$$f(t) = \exp\left(-\beta_n^2D_0t\right) \tag{2.59}$$

β_n is the n-th root of

$$J_1'(\beta_n a) = 0 \tag{2.60}$$

and $J_1'(.)$ denotes the first derivative of the first order Bessel function of the first kind [1,89].

The GPD approximation is valid under the assumption of Gaussian probability distribution for phase offsets of the particles. This assumption is valid in the short diffusion time regime corresponding to region A in Figure 2.7 because the diffusion time is so short that only a small proportion of particles located close enough to the walls have enough time to interact with the boundaries. Hence, the random motion of particles in the absence of boundaries results in a Gaussian displacement profile as well as the phase offsets. Considering the short diffusion time limit, $\kappa \ll 1$, Eq. (2.58) reduces to Eq. (2.49). The proof that Eq. (2.58) reduces to Eq. (2.49) in the short diffusion time limit follows from the fact that

$$\sum_{n=1}^{\infty}\frac{1}{\beta_n^2a^2-1} = \frac{1}{2} \tag{2.61}$$

when β_n is the n-th root of Eq. (2.60) [1,88].

The GPD approximation is also valid in the rapid diffusion regime corresponding to region C in Figure 2.7. This can be confirmed by considering the time interval Δt long enough such that the position of particles at the end of the interval does not depend on their position at the beginning of the interval. Then from central limit theorem we can conclude that the distribution of sums of increments in phase offsets over large number of intervals becomes Gaussian, even though the distribution of displacements is not Gaussian [83,88].

In the long diffusion time limit $\kappa \gg 1$ and assuming $\delta \ll \Delta$, Eq. (2.58) reduces to

$$x(G,\infty) = \exp\left[-(2\pi\gamma G\delta a)^2\right] \tag{2.62}$$

which is identical to the expression presented by Van Gelderen et al. [91].

Neuman [88], has presented the DWMR signal attenuation for the case of steady gradients ($\delta = \Delta = \tau$) using GPD approximation as

$$x(G, 2\tau) = \exp\left\{ -\frac{8\pi^2\gamma^2G^2}{D_0} \sum_{n=1}^{\infty} \frac{\beta_n^{-4}}{\beta_n^2 a^2 - 1} \left(2\tau - \frac{3 - 4\exp\left[-\beta_n^2 D_0 \tau\right] + \exp\left[-\beta_n^2 D_0\, 2\tau\right]}{\beta_n^2 D_0} \right) \right\} \quad (2.63)$$

In the long diffusion time limit, $\kappa \gg 1$ and considering a continuous gradient, the DWMR signal attenuation given in Eq. (2.63) becomes

$$x(G, 2\tau) = \exp\left[-\frac{4\pi^2\gamma^2G^2a^4}{D_0} \frac{7}{296} \left(2\tau - \frac{99}{112} \frac{a^2}{D_0} \right) \right] \quad (2.64)$$

Here, we only presented the final equations. The complete derivation of these equations can be found in Price 2009 [1], Van Gelderen et al. 1994 [91] and Neuman 1974 [88].

2.6.5 Short Gradient Pulse approximation

Another approximation used for correlating DWMR signal measured with Stejskal-Tanner technique and underlying diffusion process is Short Gradient Pulse (SGP) approximation, in which the length of gradient pulses are considered very small in comparison with the diffusion time (i.e. $\delta \ll \Delta$) so that the diffusion of particles during the application of gradient pulses can be neglected [1, 83]. This corresponds to Region B in Figure 2.7.

Using Eq. (2.43) and considering SGP approximation (i.e. $\delta \ll \Delta$), the phase offset of a spin which was at position $\mathbf{r}_0$ during the first gradient pulse and at position $\mathbf{r}$ during the second gradient pulse can be written as

$$\varphi(\mathbf{r} - \mathbf{r}_0) = 2\pi\mathbf{q}(\delta) \cdot (\mathbf{r} - \mathbf{r}_0) \quad (2.65)$$

where $\mathbf{q}(\delta)$ can be calculated using Eq. (2.38) [1, 89]. For the case of symmetric constant gradient pulses as depicted in Figure 2.6, $\mathbf{q}$ is calculated using Eq. (2.45). Note that, in the SGP approximation, we consider that the length of gradient pulse is much smaller than the diffusion time and as a result we can neglect the diffusion of particles during the gradient pulses and merely consider the displacement in the time interval between the two pulses (which is approximated by Δ) [1, 83].

The probability density of a particle starting from $\mathbf{r}_0$ and ending at $\mathbf{r}$ during time Δ is given by the diffusion propagator $P(\mathbf{r}|\mathbf{r}_0, t)$ (recall the calculation of the diffusion propagators presented in sections 2.1 and 2.2). Therefore, the signal from a single particle is calculated as:

$$S_i(\mathbf{q}, \Delta) = S_{0,i}\rho(\mathbf{r}_0)P(\mathbf{r}|\mathbf{r}_0, t)\exp\left[-\mathrm{j}\varphi_i(\mathbf{r}-\mathbf{r}_0)\right] \tag{2.66}$$

where $\rho(\mathbf{r}_0)$ denotes the starting spin density and $\varphi_i(\mathbf{r}-\mathbf{r}_0)$ is the phase offset induced by the displacement of particle from position $\mathbf{r}_0$ to $\mathbf{r}$ during time Δ. Here, we assume a homogeneous medium and uniform starting spin density $\rho(\mathbf{r}_0) = 1$. The total signal is the integration of signals from each spins over all possible starting and ending positions. Hence the total signal can be written as

$$\begin{aligned} S(\mathbf{q}, \Delta) &= S_0 \iint P(\mathbf{r}|\mathbf{r}_0, t)\exp\left[-\mathrm{j}\varphi(\mathbf{r}-\mathbf{r}_0)\right] d\mathbf{r}_0 d\mathbf{r} \\ &= \iint P(\mathbf{r}|\mathbf{r}_0, t)\exp\left[-\mathrm{j}2\pi\mathbf{q}\cdot(\mathbf{r}-\mathbf{r}_0)\right] d\mathbf{r}_0 d\mathbf{r} \end{aligned} \tag{2.67}$$

where $S_0 = S(0, \Delta)$ is the total signal in the absence of diffusion sensitising gradients [1, 89, 90]. Therefore, the diffusion related DWMR signal decay can be written as

$$\begin{aligned} x(\mathbf{q}, \Delta) &= \frac{S(\mathbf{q}, \Delta)}{S_0} \\ &= \iint P(\mathbf{r}|\mathbf{r}_0, t)\exp\left[-\mathrm{j}2\pi\mathbf{q}\cdot(\mathbf{r}-\mathbf{r}_0)\right] d\mathbf{r}_0 d\mathbf{r} \\ &= \int \bar{P}(\mathbf{R}, \Delta)\exp\left(-\mathrm{j}2\pi\mathbf{q}\cdot\mathbf{R}\right) d\mathbf{R} \end{aligned} \tag{2.68}$$

where $\mathbf{R} = \mathbf{r} - \mathbf{r}_0$ and $\bar{P}(\mathbf{R}, \Delta)$ is the mean propagator defined as

$$\bar{P}(\mathbf{R}, \Delta) = \int \rho(\mathbf{r}_0)P(\mathbf{r}_0|\mathbf{r}_0 + \mathbf{R})\, d\mathbf{r}_0 \tag{2.69}$$

Eq. (2.68) shows a Fourier relationship between $x(\mathbf{q}, \Delta)$ and $\bar{P}(\mathbf{R}, \Delta)$ namely

$$x(\mathbf{q}, \Delta) = \mathscr{F}\left\{\bar{P}(\mathbf{R}, \Delta)\right\} \tag{2.70}$$

where $\mathscr{F}\{\cdot\}$ denotes the Fourier transform.

Substituting the diffusion propagator for the free isotropic diffusion given in Eq. (2.12) into Eq. (2.69) and using Eq. (2.68), the DWMR signal attenuation in the SGP limit can is calculated as

$$x(\mathbf{q},\Delta) = \exp\left(-4\pi^2 q^2 D_0 \Delta\right) \tag{2.71}$$

where $q^2 = |\mathbf{q}|^2$ and D_0 is the diffusion coefficient.

Similarly considering the diffusion propagator for the diffusion in a cylinder with radius a given in Eq. (2.16), the DWMR signal attenuation is given by

$$x(\mathbf{q},\Delta) = \sum_{m=0}^{\infty}\sum_{n=1}^{\infty}\sum_{k=0}^{\infty} \frac{2K_{mk}a^2(2\pi qa)^4 \sin^2(2\theta)\left[1-(-1)^m\cos\left(2\pi ql\cos(\theta)\right)\right]\beta_{nk}^2}{l^2\left[(n\pi a/l)^2-(2\pi qa)^2\cos^2(\theta)\right]^2\left[\beta_{nk}^2-(2\pi qa)^2\sin^2(\theta)\right]^2\left(\beta_{nk}^2-k^2\right)} \times \left[J_n'\left(2\pi qa\sin(\theta)\right)\right]^2 \exp\left(-\left[\left(\frac{\beta_{nk}}{a}\right)^2+\left(\frac{m\pi}{l}\right)^2\right]D\Delta\right) \tag{2.72}$$

where β_{nk} is the k-th root of $J_n'(\beta_{nk}) = 0$, l is the height of the cylinder, and θ is the angle between the gradient direction and main axis of the cylinder. The constant K_{mk} depends on the values of the indices m and k defined as

$$K_{mk} = \begin{cases} 1 & \text{if } m = k = 0 \\ 2 & \text{if } (m \neq 0 \text{ and } k = 0) \text{ or } (k \neq 0 \text{ and } m = 0) \\ 4 & \text{if } m \neq 0 \text{ and } k \neq 0 \end{cases} \tag{2.73}$$

for the case of $\theta = \pi/2$, Eq. (2.72) is reduced to

$$x(\mathbf{q},\Delta) = 4(2\pi qa)^2 \sum_{n=1}^{\infty}\sum_{k=0}^{\infty} \frac{K_{0k}\beta_{nk}^2\left[J_n'(2\pi qa)\right]^2}{\left[\beta_{nk}^2-(2\pi qa)^2\right]^2\left(\beta_{nk}^2-k^2\right)} \exp\left[-\left(\frac{\beta_{nk}}{a}\right)^2 D\Delta\right] \tag{2.74}$$

The complete derivation of the equations above along with the signal expressions for other geometries can be find in [1, 29, 92].

2.7 Summary

In this chapter, first we had a brief review over the physical principles behind the diffusion process and presented diffusion equation as a mathematical tool to model the diffusion

of particles in a medium. We discussed different types of diffusion (free, hindered, and restricted) and the relevant diffusion time scales. Next, we presented a review of diffusion in porous media and discussed the parameters affecting the diffusion process in the porous media (Surface to Volume ratio, Porosity, Tortuosity etc.). Next, we had an overview of the structure of the central nervous system in human and discussed the diffusion process in the neural tissue.

As presented in this chapter, DWI has the potential to measure the diffusion of water through its sensitivity to the motion of water molecules during diffusion time [1, 13, 93]. Considering the effects of the boundaries on the diffusion of water, DWI has the capability to reveal the information about the microstructure with smaller sizes than that can be achieved by conventional MRI. Hence it can be used as a non-invasive method to study the microstructure of neural tissue [1, 45, 60, 94, 95]. We presented the methods used to measure the DWMR signal including Stejskal-Tanner method and discussed the Bloch-Torrey equations describing the diffusion weighted MR measurement.

At the end, we presented different approaches used to link the DWMR signal attenuation to diffusion process. Basically there are four approaches have been developed for this purpose, which are:

1. Solving Bloch-Torrey equations considering a given boundary conditions.
2. GPD Approximation.
3. SGP Approximation.
4. Simulating the Brownian motion of molecules for a given geometry.

However, as discussed in this chapter, solving Bloch-Torrey equations would be intractable for most but simple geometries. The simulation of Brownian motion of molecules would be quite time consuming and requires huge number of computations. On the other hand, in practice, we mostly do not have any a priori knowledge about the underlying geometry and are interested in inferring geometric information from the DWMR signal (reverse modelling) instead of calculating the DWMR signal for a given geometry. Hence, the simulation of Brownian motion of particles is not beneficial for this purpose. We presented two main approximation methods (GPD,SGP) used to link the DWMR signal attenuation to the diffusion and discussed the conditions under which these assumptions are valid [1, 83, 89]. A good understanding of the topics covered in this chapter is crucial as most of the concept discussed in this chapter will be used in the next chapter, when we talk about the signal models in the neural tissue and the ideas behind their derivations.

Chapter 3

Models of Diffusion Weighted Magnetic Resonance Signal

In the previous chapter, we discussed basic physical principles behind the diffusion process and presented DWI as a technique to investigate the diffusion characteristics of a medium through its sensitivity to the displacements of the molecules. The diffusion of particles in a medium during certain diffusion time can reveal some information about the geometric structure of the medium which can be measured by analysing DWMR signal attenuation due to diffusion [1, 28, 39, 96, 97].

DWI has been used in the past as a non-invasive method to study the morphological structure of the brain white matter. The diffusion of water particles in the brain white matter is non-isotropic due the semi-impermeable properties of the axons. This makes it possible to determine the geometry of the axons in the brain through investigation of restrictions and hindrances imposed by axon boundaries on the diffusion of particles [13].

A number of model-based techniques have been presented in the literature to model the influence of geometrical microstructure of the brain white matter on the DWMR signal attenuation. Among the different morphological parameters of the white matter, the axon orientation, axon diameter distribution and axon density have been of interest due to the hypothetical link between their changes and neuro-degenerative disorders [3–7, 13, 98]. In this chapter, we discuss a number of model-based techniques used to describe the tissue microstructure from the characteristics of DWMR signal decay.

Any technique used for modelling DWMR signal attenuation is based on certain assumptions regarding the distribution and orientation of the axons. Some techniques consider a known diameter distribution and orientation, discard estimation of axon orientation and dispersion and try to estimate the parameters of the pre-assumed statistical distri-

bution [99–104]. However, considering the known orientation limits the application of these methods to the brain regions with uniform and known orientation like the Corpus Callosum. Other techniques take the orientation and dispersion of axons into account and provide models to predict the orientation of the axons simultaneously with other parameters [13, 105–108].

In this work, we focus on the analysis of the DWMR signal decay models for the single-PGSE pulse sequence. We study the main assumptions of each model in more detail and review the benefits and drawbacks of each model. For the ease of comparison, all models are presented using the same conventions, which are introduced in this chapter.

3.1 ADC model

A simple way to express the normalised DWMR signal attenuation would be to use Eq. (2.42) in the form:

$$x(\mathbf{q}, \Delta) = \exp\left(-4\pi^2 q^2 (\Delta - \frac{\delta}{3}) D\right) \tag{3.1}$$

where Δ [s] is the diffusion time, $q = |\mathbf{q}|$ [m^{-1}] is the reciprocal wavenumber which can be calculated from a set of measurement parameters using Eq. (2.45). The tissue related parameter to be estimated using this model is the ADC (D) [m^2/s].

Eq. (3.1) for describing the diffusion related signal attenuation is valid under the assumptions of a Gaussian diffusion profile and requires a short diffusion time such that the effect of the interaction with boundaries can be neglected (see section 2.6.4) [83]. However, one can always use Eq. (3.1) to calculate a time-dependent ADC value, $D(\Delta)$, for a particular pulse sequence and diffusion time [1].

The ADC model provides an easy to estimate parameter (ADC) which captures some information about the underlying tissue microstructure [84]. The ADC parameter was introduced by Le Bihan et al. [109] in 1986, as a global parameter reflecting the diffusion related characteristics in the biological tissue. However, a single parameter cannot describe morphology in detail. Nevertheless, the ADC model is widely used as a biomarker in the identification of stroke where the deviation of ADC parameter from "normal" indicates the ischemia in the brain [110]. The measurement of the ADC parameter is usually performed by measuring the MR signal once without the diffusion encoding gradients ($\vec{G} = 0$) and later with a certain gradient field amplitude. However, measurement of the ADC value is usually performed using more than one diffusion weighting factor to cancel out the effect of noise and other artefacts. It should also be noted that in the case of anisotropic diffusion,

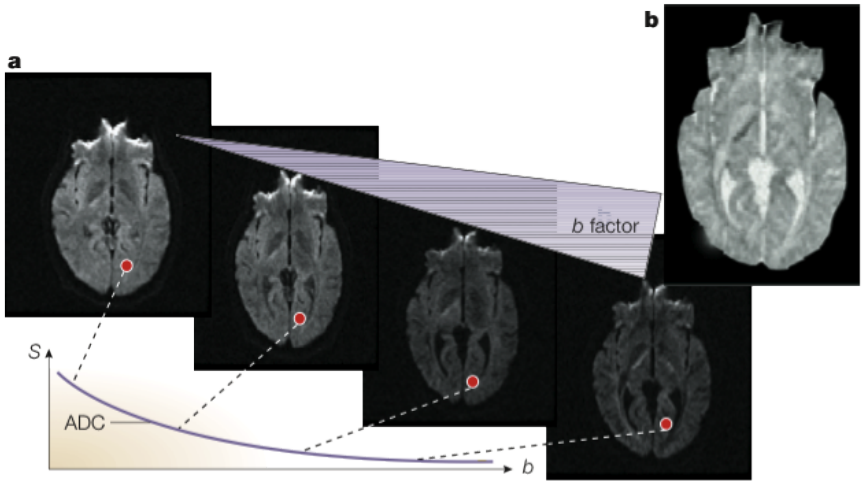

Figure 3.1: Diffusion Weighted (Magnetic Resonance) Imaging. The imaging sequence is performed using several values of diffusing weighting factor (b values). (a) The signal intensity in a particular voxel attenuates by increasing the b-value. The signal in structures with fast diffusion (higher diffusivity) like water-filled ventricular cavities decays more rapidly while the signal in tissue with slower diffusion (lower diffusivity) for example grey and white matter decays slowly. The apparent diffusion coefficient (ADC) for each voxel is calculated by fitting the signal to mono-exponential function of b-factor. (b) The resultant ADC map showing the apparent diffusion coefficient at different voxels of the image. The brighter the intensity in ADC map, the higher the ADC value of the voxel; (Figure modified from Le Bihan, Nature reviews. Neuroscience 2003 [96]).

the ADC value calculated using this method is based on the GPD approximation and will be dependent on the diffusion time (Δ) as well as the gradient direction [111]. A simple visualisation of the application of DWI to calculate the ADC map of the brain is presented in Figure 3.1.

3.2 Diffusion Tensor Imaging

As mentioned earlier, the diffusion in the biological tissue is not isotropic in general and the ADC value calculated from Eq. (3.1) depends on the gradient direction and diffusion time in general. The diffusion tensor is represented by a positive definite symmetric matrix (see section 2.1) [1,112]. Assuming a Gaussian diffusion profile for the particles it would be possible to reconstruct the apparent diffusion tensor $\mathbf{D}$ by measuring the ADC values in at least 6 different orthogonal directions (because the associated matrix is symmetric) [113]. For a gradient field G_i in direction $\mathbf{e}_i$, the net DWMR signal decay is modelled as:

$$x(\mathbf{q}_i, \Delta) = \exp\left(-4\pi^2(\Delta - \frac{\delta}{3})\mathbf{q}_i^T \mathbf{D}\mathbf{q}_i\right) \tag{3.2}$$

where $\mathbf{q}_i = \gamma\delta\vec{G}_i$ and $\mathbf{q}_i^T$ is the vector transpose of $\mathbf{q}_i$. Eq. (3.2) can be used to determine the apparent diffusion tensor by solving the system of linear equations with several gradient direction. Although theoretically, the apparent diffusion tensor can be calculated by performing the measurements in six non-collinear directions, the measurements usually are performed with more number of gradient directions to cancel the effect of noise and artefacts [45, 112, 114, 115].

The diffusion tensor provides information about the ADC values in different directions. Since the diffusion tensor is symmetric and positive definite, it can be decomposed using eigenvalue decomposition as:

$$\mathbf{D} = \mathbf{V}\mathbf{\Lambda}\mathbf{V}^{-1} \tag{3.3}$$

where $\mathbf{V} = [\mathbf{v}_1 \quad \mathbf{v}_2 \quad \mathbf{v}_3]$ is a matrix, each column of which is an eigenvector of $\mathbf{D}$ and $\mathbf{\Lambda}$ is a diagonal matrix of the corresponding eigenvalues:

$$\mathbf{\Lambda} = \begin{bmatrix} \lambda_1 & 0 & 0 \\ 0 & \lambda_2 & 0 \\ 0 & 0 & \lambda_3 \end{bmatrix} \tag{3.4}$$

By convention, we order $\lambda_1 \geq \lambda_2 \geq \lambda_3$ ($\mathbf{v}_i$ is the eigenvector corresponding to λ_i). The diffusion tensor is usually visualised by an ellipsoid illustrating the diffusion profile of the particles. The eigenvectors coincide with the axes of the ellipsoid and the eigenvalues are axes length. As presented in the previous chapter, for the case of isotropic diffusion, the diffusion tensor can be represented by a sphere and $\lambda_1 = \lambda_2 = \lambda_3 > 0$.

In order to produce a single figure of merit describing different aspect of the diffusion profile within the brain tissue, a number of parameters calculated from the diffusion tensor. Each of these parameters captures a single characteristic of diffusion profile. Among the different parameters, mean diffusivity (MD), fractional anisotropy (FA), relative anisotropy (RA) and volume ratio (VR) are of more interest [45, 116]. The definition of these quantities is described below:

$$\mathrm{MD} = \frac{1}{3}(\lambda_1 + \lambda_2 + \lambda_3) = \frac{\mathrm{tr}(\mathbf{D})}{3} \tag{3.5}$$

$$\mathrm{FA} = \sqrt{\frac{3}{2} \times \frac{(\lambda_1 - \mathrm{MD})^2 + (\lambda_2 - \mathrm{MD})^2 + (\lambda_3 - \mathrm{MD})^2}{\lambda_1^2 + \lambda_2^2 + \lambda_3^2}} \tag{3.6}$$

$$\mathrm{RA} = \sqrt{\frac{1}{2} \times \frac{(\lambda_1 - \mathrm{MD})^2 + (\lambda_2 - \mathrm{MD})^2 + (\lambda_3 - \mathrm{MD})^2}{\mathrm{MD}}} \tag{3.7}$$

$$\mathrm{VR} = \frac{\lambda_1 \lambda_2 \lambda_3}{(\mathrm{MD})^3} \tag{3.8}$$

Mean diffusivity provides an estimate of the overall diffusivity of the tissue and can be used to predict the average mean square displacement (MSD) of diffusive particles. The fractional isotropy is a number between zero and one, and describes the degree of anisotropy of a diffusion process. A value of zero indicates the isotropic diffusion, i.e. the diffusion is unrestricted (or equally restricted) in all directions. A value of one indicates that the diffusion is only possible in one direction and is completely restricted along all other directions. Relative anisotropy reflects the ratio of anisotropy relative to the mean diffusivity and volume ratio presents the ratio between the volume of the diffusion ellipsoid and the volume of the isotropic mean diffusion sphere. For the case of isotropic diffusion, $\mathrm{MD} = \lambda_1 = \lambda_2 = \lambda_3$, $\mathrm{FA} = 0$, $\mathrm{RA} = 0$ and $\mathrm{VR} = 1$. The features derived from DTI are commonly used clinically to localise white matter lesions, which cannot be identified using other forms of clinical MRI [45, 117].

In order to illustrate the diffusion properties of the white matter, the diffusion tensor is calculated for each voxel of the image. The fibre direction is identified by the eigenvector corresponding to the largest eigenvalue, which can be colour-coded to achieve a cartography of the fibre tracts, a process called tractography. The colour-codes are indicated as red for left-right, blue for superior-inferior, and green for anterior-posterior and is quantised and combined to illustrate the directions in compound directions (e.g. left-inferior). The brightness is weighted by the fractional anisotropy which indicates the degree of anisotropy in a given voxel. Figure 3.2 depicts a simple visualisation of application of DTI tractography in the human brain. Tractography is widely used in the fields of cognitive neuroscience and neurobiology as a tool for measuring deficits in white matter, such as in ageing since its estimation of fibre orientation is interestingly accurate [117].

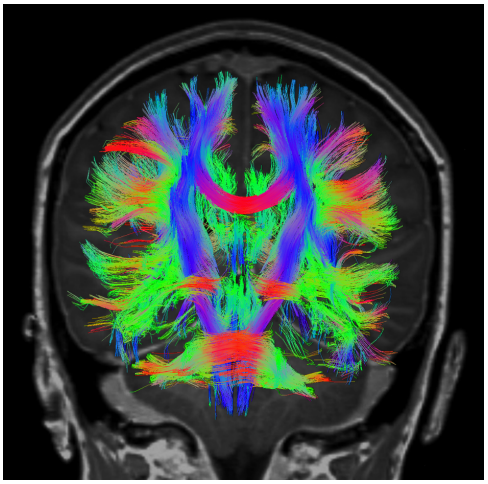

Figure 3.2: Diffusion Tensor Imaging (DTI) used for tractography.

3.3 Bi-exponential model

Due to the high complexity of the microstructure of the white matter, the assumption of a Gaussian diffusion profile is not valid in general and as a result the dependence of the DWMR signal decay on single gradient field amplitude cannot be explained using a mono-exponential function [118]. A number of studies have demonstrated the non-mono-exponential behaviour of the DWMR signal decay [84, 101, 119–131]. The deviation of DWMR signal decay from mono-exponential function is considered as an evidence for the existence of two or more compartment models. Considering the porous structure of the brain tissue and the fact that the total received signal is the integral over all the particles, a number of studies suggested modelling the DWMR signal decay using a bi-exponential model as a weighted sum of two mono-exponential functions with different ADC values arising from the restricted (slow) and hindered (fast) compartments [119, 120].

$$x(\mathbf{q}, \Delta) = (1 - f)\, x_h(\mathbf{q}, \Delta) + f\, x_r(\mathbf{q}, \Delta) \tag{3.9}$$

where x_h and x_r are the signal attenuation related to hindered and restricted compartments respectively and f is the volume fraction [45,119,132]. The volume fraction is related to surface-to-volume ratio (S_p/V_p) of the porous structure and determines the ratio of the particles which interact with the boundaries to the total number of spins. It should be noted that the volume fraction is a function of time, however, in this model it is consider as a fixed value. It is also assumed that the exchange of particles between hindered and restricted compartments are quite slow in comparison to the diffusion time scale and can be neglected. Therefore, the signal can be modelled as a weighted sum of the signals from hindered and restricted compartments [119]. The ADC for restricted compartment is lower

resulting in a slow decay function while the ADC for hindered part is larger and results in a fast attenuation of the DWMR signal. Assuming GPD approximation, the contribution of the hindered compartment to the normalised signal attenuation can be modelled as:

$$x_h(\mathbf{q}, \Delta) = \exp\left(-4\pi^2|\mathbf{q}|^2(\Delta - \frac{\delta}{3})D_h\right) \tag{3.10}$$

where D_h is the ADC for the hindered or fast compartment. On the other hand, the normalised signal from restricted compartment is modelled as:

$$x_r(\mathbf{q}, \Delta) = \exp\left(-4\pi^2|\mathbf{q}|^2(\Delta - \frac{\delta}{3})D_r\right) \tag{3.11}$$

where D_r is the ADC for the restricted or slow compartment.

The parameters of the model to be estimated are the diffusivities for the hindered and restricted compartment (D_h and D_r respectively) and the volume fraction. Therefore, the number of measurements needed to estimate the parameters should be at least three (measurements using 3 different q values).

3.4 Statistical approach

The ADC approach determines the average diffusion coefficient value in the voxel being examined using mono-exponential model of DWMR signal. A most reasonable development would be to consider the signal as the combination of several mono exponential compartments arising from different spin packets.

The voxel being examined under diffusion magnetic resonance measurement contains a variety of cells, intercellular and extracellular spaces. Hence, the DWMR signal can be considered as the sum of signals arising from a large number of spin packets originating from different positions in the voxel. For each spin packet a mono exponential function as in Eq. (3.1) is considered. Each spin packet has its own ADC [133].

Since spin packets are originated from different positions and travel through different displacement trajectories, their ADC values are different. The total DWMR signal can be described by the distribution function of ADCs, $P(D)$ or the fraction of each spin packet. For simplicity, the dependency of ADC to the pulse gradient waveform and diffusion time is neglected. Given these assumptions the DWMR signal can be written as:

$$S = S_0 \int_0^\infty P(D) \exp(-bD) dD \tag{3.12}$$

In the case of identifiable number of spin packets with known fractions and ADC values, the distribution function is:

$$P(D) = \sum_{i=1}^{n} f_i \delta(D - D_i) \tag{3.13}$$

in which f_i is the fraction of packets with $D = D_i$ and $\delta(.)$ is the Dirac delta function. Hence, the DWMR signal can be written as:

$$S = S_0 \sum_{i=1}^{n} f_i \exp(-bD_i) \tag{3.14}$$

If the diffusion time (Δ) is much longer than the time required for the spins to encounter a big number of hinderances and restrictions, the shape of $P(D)$ reflects the micro-structural information in the voxel [103, 133].

3.5 Kurtosis approach

As mentioned earlier, the assumption of Gaussian diffusion profile for the diffusion of water molecules in the brain white matter is not valid in general and the attempt to model the signal decay using a mono-exponential function fails to describe the signal behaviour accurately [118]. Another technique which has been used to model the non-mono-exponential characteristics of DWMR signal attenuation is to take into account the excess diffusion kurtosis as a measure to quantify the deviation of the diffusion profile from Gaussian shape [134, 135]. The excess diffusion kurtosis K is defined as:

$$K = \frac{E\{(\mathbf{r} - \mathbf{r}_0)^4\}}{E\{(\mathbf{r} - \mathbf{r}_0)^2\}^2} - 3 = \frac{\mu_4}{\sigma^4} - 3 \tag{3.15}$$

where $\mathbf{r}$ and $\mathbf{r}_0$ are the initial and final positions respectively. μ_4 is the forth moment and σ is the standard deviation. The kurtosis factor is a measure of the sharpness or smoothness of a PDF and provides a measure for the deviation from being Gaussian. For a Gaussian PDF the excess kurtosis factor is zero [134, 135].

Jensen et al. [136] presented a model based on the Taylor series expansion of signal $\ln(x(b))$ as:

$$\ln(x(b)) = -bD + \frac{1}{6} K b^2 D^2 + O(b^3) \tag{3.16}$$

in which, K is the diffusion kurtosis factor and D is the ADC. b is the diffusion weighting factor as described by Eq. (2.40) and $O(b^3)$ denotes the higher order terms. Neglecting

the higher order terms, the normalised DWMR signal attenuation can then be modelled as:

$$x(b) = \exp\left(-bD + \frac{1}{6}Kb^2D^2\right) \tag{3.17}$$

The tissue related parameters of the model to be estimated are the apparent diffusion coefficient (D) and diffusion kurtosis (K).

Eq. (3.17) is derived using the Taylor series expansion of $\ln(x(b))$ for sufficiently small values of b so that the bD falls inside the convergence radius b_c (The radius for which the approximations converge to the exact values). In general considering more terms in the Taylor series expansion results in larger convergence radius. However, using more terms introduce more non-linearity and increases the approximation errors, needing greater number of measurements. On the other hand, the b-values used in DWMR measurements are typically chosen larger to increase the sensitivity of the measurements to the motion of the particles and considering the terminated series of Eq. (3.17), does not guarantee that the bD values will fall inside the convergence radius. This limits the application of this model to the cases of small b-values or small diffusivities (D). For the b-values resulting in bD values beyond the convergence radius b_c, the cumulant series expansion will diverge and the application of the model to fit the experimental data will fail [137].

The kurtosis model is also only valid under the assumption of short diffusion time regime ($\kappa \ll 1$) by which the diffusion length $\sqrt{Dt}$ is much smaller than the characteristic length of the tissue micro-structure. In the case of long diffusion time regime ($\kappa \gg 1$), the time dependent diffusion coefficient falls dramatically and the mean square displacement will be independent of the diffusion time and the Taylor series expansion in Eq. (3.16) will not be valid [137].

3.6 CHARMED

Among the models developed, Composite Hindered And Restricted Model of Diffusion (CHARMED) assumes that the white matter is modelled as a population of impermeable cylindrical axons embedded in a homogeneous medium. The model embodies both hindered and restricted diffusion in the brain white matter and presents a modelling framework which captures both the aspects of the diffusion tensor imaging and q-space imaging [100, 105].

The model assumes the diffusion weighted signal attenuation as a combination of signals arising from hindered diffusion in the extra-axonal volume (including extra- and intra-

cellular spaces) and restricted diffusion in the intra-axonal volume [100]. The exchange between the compartments considered slow with respect to measurement time scale and as a result the net normalised DWMR signal attenuation is modelled as:

$$x(\mathbf{q}, \Delta) = f_h x_h(\mathbf{q}, \Delta) + f_r x_r(\mathbf{q}, \Delta) \tag{3.18}$$

where $x_h(\mathbf{q}, \Delta)$ and $x_r(\mathbf{q}, \Delta)$ are the signal from hindered and restricted compartments and f_h and f_r are T_2-weighted volume fractions respectively [100, 105]. $\mathbf{q}$ is the reciprocal wavenumber described using Eq. (2.45)

3.6.1 Signal model for restricted compartment

The signal from restricted compartment itself, $x_r(\mathbf{q}, \Delta)$, is also decomposed into contributions from spins diffusing parallel and perpendicular to the axon direction [105]. The displacements of particles perpendicular to fibre direction are considered independent from the displacements parallel to it since there is no boundaries for the displacement in the fibre direction. Hence, the signal from restricted compartment can be written as:

$$x_r(\mathbf{q}, \Delta) = x_{r\perp}(q_\perp, \Delta) x_{r\parallel}(q_\parallel, \Delta) \tag{3.19}$$

where $q_\perp = \gamma G_\perp \delta$ and $q_\parallel = \gamma G_\parallel \delta$. In general $\vec{G}$ is not perpendicular to the fibre direction. However, we can decompose $\vec{G}$ into components parallel and perpendicular gradient field strengths, $G_\parallel$ and $G_\perp$ respectively, where

$$\begin{aligned} G_\parallel &= G\cos(\alpha) \\ G_\perp &= G\sin(\alpha) \end{aligned} \tag{3.20}$$

and α is the angle between $\vec{G}$ and the fibre direction [138].

For displacements parallel to axon direction, the model assumes 1D Gaussian diffusion with diffusion coefficient $D_\parallel$. Therefore, the signal arising from spins diffusing parallel to axon directions can be written as:

$$x_{r\parallel}(q_\parallel, \Delta) = \exp\left(-4\pi^2 q_\parallel^2 (\Delta - \frac{\delta}{3}) D_\parallel\right) \tag{3.21}$$

which is identical to Stejskal's familiar equation presented in Eq. (2.47).

The model assumes a constant gradient field under the condition $\delta \sim \Delta$ and considers the signal arising from displacement of the particles perpendicular to axons using Neuman's

expression [88] for the diffusion in a cylinder with radius R using a constant gradient field and under GPD assumption (see section 2.6.4).

$$x_{r\perp}(q_\perp, \Delta) = \exp\left(\frac{-4\pi^2 R^4 q_\perp^2}{D_\perp \tau} \times \frac{7}{296} \times \big(2 - \frac{99}{112}\big) \times \frac{R^2}{D_\perp \tau}\right) \tag{3.22}$$

where $D_\perp$ is the intra-cellular diffusivity perpendicular to the axon direction and τ is half the echo time. Eq. (3.22) is identical to Eq. (2.64) derived under GPD assumption in section 2.6.4.

Substituting Eq. (3.21) and Eq. (3.22) into Eq. (3.19), the signal from restricted compartment consisting of bundles with radius R is expressed as:

$$x_r(\mathbf{q}, \Delta) = \exp\left(-4\pi^2 q_\parallel^2 (\Delta - \frac{\delta}{3}) D_\parallel\right) \exp\left(\frac{-4\pi^2 R^4 q_\perp^2}{D_\perp \tau} \times \frac{7}{296} \times \big(2 - \frac{99}{112}\big) \times \frac{R^2}{D_\perp \tau}\right) \tag{3.23}$$

3.6.2 Signal model for hindered compartment

As mentioned earlier, the diffusion of water particles in the extra-axonal space is assumed as hindered and as a result the signal arising from extra-cellular space can be modelled using 3D Gaussian displacement distribution [105]. In general the diffusion in extracellular space is considered anisotropic which can be characterised by the diffusion tensor $\mathbf{D}_h$. By considering cylindrical symmetry, one can represent the diffusion tensor in 3D frame of references as:

$$\mathbf{D}_h = \begin{bmatrix} \lambda_\perp & 0 & 0 \\ 0 & \lambda_\perp & 0 \\ 0 & 0 & \lambda_\parallel \end{bmatrix} \tag{3.24}$$

where $\lambda_\perp$ and $\lambda_\parallel$ are the eigenvalues of the diffusion tensor associated with the eigenvectors perpendicular and parallel to the fibre direction respectively. Eq. (3.24) indicates that the matrix associated with the diffusion tensor is considered as a rank two matrix which consists of two independent elements $\lambda_\perp$ and $\lambda_\parallel$ [91].

The signal is then represented as

$$x_h(\mathbf{q}, \Delta) = \exp\left(-4\pi^2 (\Delta - \frac{\delta}{3}) \mathbf{q}^T \mathbf{D}_h \mathbf{q}\right) \tag{3.25}$$

The anisotropy in the extracellular space is considered as a result of reflections from axon boundaries and increased tortuosity due to the existence of axons and other biological

components. Considering $\mathbf{q} = \mathbf{q}_\parallel + \mathbf{q}_\perp$ and $\mathbf{q}_\perp \cdot \mathbf{q}_\parallel = 0$ we can simplify the quadratic term in Eq. (3.25) as:

$$\begin{aligned}\mathbf{q}^T\mathbf{D}_h\mathbf{q} &= (\mathbf{q}_\parallel + \mathbf{q}_\perp)^T\mathbf{D}_h(\mathbf{q}_\parallel + \mathbf{q}_\perp) \\ &= \mathbf{q}_\perp^T\mathbf{D}_h\mathbf{q}_\perp + \mathbf{q}_\parallel^T\mathbf{D}_h\mathbf{q}_\parallel \\ &= \mathbf{q}_\perp^T\lambda_\perp\mathbf{q}_\perp + \mathbf{q}_\parallel^T\lambda_\parallel\mathbf{q}_\parallel \\ &= q_\perp^2\lambda_\perp + q_\parallel^2\lambda_\parallel \end{aligned} \tag{3.26}$$

Therefore, Eq. (3.25) can be written as:

$$\begin{aligned}x_h(\mathbf{q},\Delta) &= \exp\left(-4\pi^2\big(\Delta - \frac{\delta}{3}\big)\big(q_\perp^2\lambda_\perp + q_\parallel^2\lambda_\parallel\big)\right) \\ &= \exp\left(-4\pi^2\big(\Delta - \frac{\delta}{3}\big)q_\perp^2\lambda_\perp\right)\exp\left(-4\pi^2\big(\Delta - \frac{\delta}{3}\big)q_\parallel^2\lambda_\parallel\right)\end{aligned} \tag{3.27}$$

which shows relationship similar to what we had for restricted compartment in Eq. (3.19).

The net signal decay is modelled by substituting Eq. (3.23) and Eq. (3.27) into Eq. (3.18) and noting that $f_h + f_r = 1$. Hence

$$\begin{aligned}x(\mathbf{q},\Delta) = (1-f)\,&\exp\left(-4\pi^2\big(\Delta - \frac{\delta}{3}\big)q_\perp^2\lambda_\perp\right)\exp\left(-4\pi^2\big(\Delta - \frac{\delta}{3}\big)q_\parallel^2\lambda_\parallel\right) \\ &+ f\,\exp\left(-4\pi^2 q_\parallel^2(\Delta - \frac{\delta}{3})D_\parallel\right)\exp\left(\frac{-4\pi^2R^4q_\perp^2}{D_\perp\Delta} \times \frac{7}{296} \times \big(2 - \frac{99}{112}\big) \times \frac{R^2}{D_\perp\Delta}\right)\end{aligned} \tag{3.28}$$

where $f = f_r$ is the volume fraction for the restricted compartment [100, 105]. It is also possible to consider a number of restricted compartments in the CHARMED model:

$$x(\mathbf{q},\Delta) = f_h.x_h(\mathbf{q},\Delta) + \sum_{j=1}^{N} f_r^j.x_r^j(\mathbf{q},\Delta) \tag{3.29}$$

where f_r^j and $x_r^j(q,\Delta)$ are the volume fraction and signal decay of the j^{th} restricted compartment respectively [94, 100, 105, 139] and

$$f_h + \sum_{j=1}^{N}\big(f_r^j\big) = 1 \tag{3.30}$$

CHARMED utilises High Angular Resolution Diffusion Imaging (HARDI) [140–142] technique consisting of several measurements with different gradient field amplitudes (q-values) and different directions distributed uniformly and symmetrically over a sphere to capture the tissue related information [100, 143]. In order to fit the experimental data a non-linear least square estimation technique (Levenberg-Marquardt minimisation procedure) has been utilised and three cases have been considered:

1. The model consists of one hindered compartment and no restricted compartments i.e. $N = 0$. This case is identical to DTI analysis.

2. The model consists of one hindered and one restricted compartments i.e. $N = 1$. This case can be used in the areas with parallel and homogeneous fibres e.g. Corpus Callosum.

3. The model consists of one hindered and two restricted compartments i.e. $N = 2$. This case can be used for considering the crossing fibres [100, 105].

The model parameters to be estimated are the orientation of the fibres, volume fractions for restricted compartments, the parallel and perpendicular diffusivities for restricted compartment ($D_{\parallel}$ and $D_{\perp}$) and the parallel and perpendicular diffusivities for hindered compartment ($\lambda_{\parallel}$ and $\lambda_{\perp}$). The noise floor is also estimated during the fitting procedure [100].

3.7 AxCaliber

Later, Assaf et al. [99] presented a method based on CHARMED [100, 105], but included an Axon Diameter Distribution (ADD) function. The method, which is called AxCaliber, models the tissue as a composition of hindered and restricted compartments and incorporates the diameter distribution of restricted cylindrical axons as an unknown function to be estimated. AxCaliber assumes that the axon radii follow a two-parameter gamma distribution and intracellular space has the fraction density f_r.

AxCaliber, extends the two compartment hindered/restricted CHARMED model to describe the diffusion weighted signal attenuation. Hence, the net signal is modelled with the equation presented in Eq. (3.18). The experimental protocol assumes that the measurements are performed perpendicular to the fibre direction. The diffusion in the extra-axonal space is considered hindered and can be modelled as an anisotropic diffusion with an apparent diffusion coefficient D_h in the direction perpendicular to the direction of nerve bundle. Therefore, the contribution of hindered compartment is modelled as:

$$x_h(\mathbf{q},\Delta) = \exp\left(-4\pi^2 q^2 (\Delta - \frac{\delta}{3}) D_h\right) \tag{3.31}$$

where Δ and δ are the diffusion time and gradient pulse width respectively and $q = |\mathbf{q}|$. Since the experiments satisfy the SGP approximation i.e. $\delta \sim 0$ and $\delta \ll \Delta$, Callaghan's approach [29, 144] can be used by which the contribution of the intra-axonal restricted diffusion for an axon with radius R to the DWMR signal decay is expressed as:

$$\begin{aligned} x_r(\mathbf{q},\Delta) = &\sum_k 4\exp\left(-\beta_{0k}^2 D_0 \Delta / R^2\right) \left(\frac{(2\pi qR) J_0'(2\pi qR)}{(2\pi qR)^2 - \beta_{0k}^2}\right)^2 \\ &+ \sum_{nk} 8\exp\left(-\beta_{nk}^2 D_0 \Delta / R^2\right) \times \frac{\beta_{nk}^2}{\beta_{nk}^2 - n^2} \times \left(\frac{(2\pi qR) J_n'(2\pi qR)}{(2\pi qR)^2 - \beta_{nk}^2}\right)^2 \end{aligned} \tag{3.32}$$

Where J_n' are the derivatives of the n^{th}-order Bessel function and β_{nk} are the arguments that result in zero-crossings of J_n' (roots of Eq. (2.60)) [99]. Eq. (3.32) is identical to Eq. (2.74) derived using the SGP approximation in section 2.6.5.

Generalizing Eq. (3.32), the restricted diffusion signal for the multi-compartment AxCaliber model is described as:

$$\begin{aligned} x_r(\mathbf{q},\Delta) = \sum_{j=1}^{N} \pi R_j^2 f_r^j \Bigg[&\sum_k 4\exp\left(-\beta_{0k}^2 D_0 \Delta / R_j^2\right) \left(\frac{(2\pi qR_j) J_0'(2\pi qR_j)}{(2\pi qR_j)^2 - \beta_{0k}^2}\right)^2 \\ &+ \sum_{nk} 8\exp\left(-\beta_{nk}^2 D_0 \Delta / R_j^2\right) \times \frac{\beta_{nk}^2}{\beta_{nk}^2 - n^2} \times \left(\frac{(2\pi qR_j) J_n'(2\pi qR_j)}{(2\pi qR_j)^2 - \beta_{nk}^2}\right)^2 \Bigg] \end{aligned} \tag{3.33}$$

where R_j is the radius of the j-th axon, f_r^j is the volume fraction of the j-th axon and D_0 is the intra-cellular diffusivity perpendicular to the fibre direction and is considered equal to the intrinsic diffusivity of the medium. The axon radii are modelled using gamma distribution i.e. $f_r^j \sim \Gamma(k,\theta)$ where,

$$\Gamma(k,\theta) = \frac{1}{\Gamma(k)\theta^k} R_j^{k-1} \exp\left(-R_j/\theta\right) \quad \forall R \geq 0 \,\text{and}\, k,\theta > 0 \tag{3.34}$$

is the gamma distribution with the shape parameter k and the scale parameter θ [99]. $\Gamma(k)$ is the gamma function described as:

$$\Gamma(k) = \int_0^\infty t^{k-1} \exp\left(-t\right) dt \tag{3.35}$$

where k is a complex number with positive real part .

AxCaliber technique takes a series of PGSE measurements with a wide range of different diffusion weightings (q values) and different diffusion times. The framework can be applied

either spectroscopically i.e. considering the whole sample as a homogeneous voxel or for a particular voxel where the axon diameter distribution is measured within that particular voxel in the imaging volume. The model parameters to be estimated are the volume fraction of the restricted compartment f_r, the diffusivity of the hindered compartment and the parameters of the gamma distribution (k and θ) [94, 99].

It has been assumed that the axons in the imaged sample are perpendicular to the gradient magnitudes and diffusion gradients. Therefore, AxCaliber supports the estimation of a model of full axon diameter distribution only under the assumption of a priori knowledge about the orientation of axons which is not applicable in general. [145].

3.8 MMWMD

Alexander [146] developed a simple tissue model based on CHARMED model. The model which is called Minimal Model of White Matter Diffusion (MMWMD), reduces the number of parameters in the CHARMED model by simplifying the model using the following assumptions [106, 146, 147]:

1. The net signal is a combination of signals from one hindered and one restricted compartments without water exchange between compartments.

2. All parallel non-abutting cylindrical axons have identical radius.

3. The particles in the extra-axonal space have cylindrically symmetric hindered diffusion. Therefore, the apparent diffusion tensor for the hindered compartment can be described as $\mathbf{D}_h = (\lambda_{\parallel} - \lambda_{\perp})\mathbf{v}\mathbf{v}^T + \lambda_{\perp}\mathbf{I}$ where $\lambda_{\parallel}$ and $\mathbf{v}$ are the major eigenvalue and eigenvector in the fibre direction respectively, $\lambda_{\perp}$ is the minor eigenvalue which is perpendicular to $\mathbf{v}$ and $\mathbf{I}$ is the identity tensor. $\lambda_{\parallel}$ and $\lambda_{\perp}$ are the diffusivities parallel and perpendicular to the fibre direction ($\mathbf{v}$) respectively.

4. The intrinsic diffusivity of extra- and intracellular spaces are the same.

Based on these assumptions and utilising CHARMED model, MMWMD describes the net normalised diffusion weighted MR signal decay as a weighted sum of signals from hindered and restricted compartments similar to CHARMED model given in Eq. (3.18) [100, 105]. However, since the model considers only a two compartment model, the net signal decay is described using Eq. (3.9).

3.8.1 Signal model for restricted compartment

The signal model for restricted compartment, utilises the assumption of in-dependency of displacements parallel and perpendicular to the fibre direction and presents the restricted signal similarly to CHARMED model given in Eq. (3.19) as a product of signals from parallel and perpendicular components.

$$x_r(\mathbf{q}, \Delta) = x_{r\perp}(q_\perp, \Delta) x_{r\parallel}(q_\parallel, \Delta) \tag{3.36}$$

where $q_\perp = \gamma G_\perp \delta$ and $q_\parallel = \gamma G_\parallel \delta$. $G_\parallel$ and $G_\perp$ are the parallel and perpendicular components of $\vec{G}$ respectively, which can be calculated using Eq. (3.20) [138].

The diffusion within the axons and parallel to axon direction is considered as Gaussian diffusion similar to the assumption in CHARMED. Since the diffusivity of particles parallel to the fibre direction in the intra-axonal and extra-axonal space are considered the same and equal to $\lambda_\parallel$, the parallel component is described as:

$$x_{r\parallel}(q_\parallel, \Delta) = \exp\left(-4\pi^2 q_\parallel^2 (\Delta - \frac{\delta}{3})\lambda_\parallel\right) \tag{3.37}$$

which is similar to the expression for the parallel component of the restricted signal in the CHARMED model Eq. (3.21).

The perpendicular component is calculated using the Van-Gelderen's extension [91] to Murday and Cotts model [148] under the assumption of long diffusion time limit i.e. $\kappa \gg 1$. Hence the signal attenuation due the diffusion of particles perpendicular to the cylindrical axons with radius R is expressed as:

$$x_{r\perp}(q_\perp, \Delta) = \exp\left(-4\pi^2 q_\perp^2 R^2\right) \tag{3.38}$$

Which is identical to Eq. (2.62) for the diffusion in a cylinder considering long diffusion time limit ($\kappa \gg 1$) and GPD approximation (see section 2.6.4). Therefore, the total signal from restricted compartment is calcualted by substituting Eq. (3.37) and Eq. (3.38) into Eq. (3.36), which results in:

$$x_r(\mathbf{q}, \Delta) = \exp\left(-4\pi^2 q_\parallel^2 (\Delta - \frac{\delta}{3})\lambda_\parallel\right) \exp\left(-4\pi^2 q_\perp^2 R^2\right) \tag{3.39}$$

3.8.2 Signal model for hindered compartment

The hindered extra-axonal compartment is modelled using a simple cylindrically symmetric Gaussian anisotropic diffusion with diffusion tensor $\mathbf{D}_h = (\lambda_\parallel - \lambda_\perp)\mathbf{v}\mathbf{v}^T + \lambda_\perp \mathbf{I}$, where

$\lambda_{\parallel}$ and $\lambda_{\perp}$ are diffusivities parallel and perpendicular to the fibre direction $\mathbf{v}$. Therefore, using the same approach for CHARMED, the signal from the hindered compartment is described as [138, 146]:

$$x_h(\mathbf{q}, \Delta) = \exp\left(-4\pi^2(\Delta - \frac{\delta}{3})\mathbf{q}^T\mathbf{D}_h\mathbf{q}\right) \tag{3.40}$$

The tissue model parameters to be estimated are:

1. The volume fraction of the intracellular space (f) which is equal to the packing density.
2. The apparent diffusion coefficients parallel and perpendicular to the fiber orientation ($\lambda_{\parallel}$ and $\lambda_{\perp}$).
3. The major eigenvector ($\mathbf{v}$) which is the same as the axon orientation.
4. The axon radius (R).

The estimated axon radius R, in the voxel is often called the axon index [13].

The model is extended by Alexander [13], to improve the previous technique [106] by adding extra compartments to the model. This extended model considers the signal as the weighted sum of signals arising from four different tissue compartments:

$$x(\mathbf{q}, \Delta) = \sum_{i=1}^{4} f_i.x_i(\mathbf{q}, \Delta) \tag{3.41}$$

where f_i and $x_i(\mathbf{q}, \Delta)$ are the volume fraction and signal component corresponding to i-th compartment such that

$$\sum_{i=1}^{4} f_i = 1 \tag{3.42}$$

Each compartment has its own characteristics and signal decay models. Signal $x_1(\mathbf{q}, \Delta)$ corresponds to the diffusion of the water molecules trapped inside the axons with equal radius R along the axis of the cylinders. It can be modelled using Gaussian phase distribution approximation of the signal from particles trapped inside a cylinder developed by Murday and Cotts [148]. This is equivalent to the expression presented in Eq. (3.39).

Signal $x_2(\mathbf{q}, \Delta)$ corresponds to the diffusion of water molecules outside the cylinders and can be modelled as an anisotropic hindered diffusion with an apparent diffusion tensor $\mathbf{D}_h$ [149]. The hindered diffusion tensor has a major eigenvalue $\lambda_{\parallel}$ corresponding to the diffusivity parallel to the fibre direction and a minor eigenvalue $\lambda_{\perp}$ corresponding to the

diffusivity perpendicular to the fibre direction. This is identical to Eq. (3.40) presented earlier [138]. The diffusion inside the cylinders is considered unhindered along the fibre direction with the intrinsic diffusivity equal to $\lambda_{\parallel}$ as assumed in [106].

Signal $x_3(\mathbf{q}, \Delta)$ arises from the diffusion of water molecules in CSF, where the cylinders do not affect diffusion. The diffusion of particles in CSF is assumed as free and modelled with an isotropic Gaussian diffusion, as in [94], with a diffusion coefficient equal to the intrinsic diffusivity $\lambda_{\parallel}$ [13].

Signal $x_4(\mathbf{q}, \Delta)$ corresponds to stationary water trapped in glial cells and other subcellular structures which remains unattenuated by diffusion weighting i.e. $x_4(\mathbf{q}, \Delta) = 1$ [13, 150].

The tissue related parameters of the model to be estimated are f_i, $\lambda_{\parallel}$, $\lambda_{\perp}$, R and the orientation of cylinders ($\mathbf{v}$).

The basic benefits of this technique is that it considers additional CSF (similar to [94]) and sub-celluar (similar to [101]) compartments. It also utilises an optimised experimental design to explore all possible PGSE combinations by improving a priori parameter settings. The estimation of the parameters are performed using Bayesian estimation techniques from a set of PGSE measurement data acquired with different diffusion weighting b values and in several directions. In order to achieve better performance, the framework uses a grid search and gradient descent stages in the fitting procedure [13].

3.9 Generalised 1D

Johnston et al. [104] developed a simple closed-form restricted signal decay model based on the work of Cory et al. [97]. The model assumes the signal as a two compartment hindered/restricted model as presented in Eq. (3.9). The signal from the hindered compartment is considered as a result of Gaussian displacement profile for the water molecules. Hence the signal from the hindered compartment is modelled using Eq. (3.10).

For $\Delta >> R^2/D$ the 1-d brownian motion trajectories fully explore the restricted space during the diffusion time and the resultant phase distribution is uniform. Integrating over all initial positions results in a triangular phase distribution with twice the compartment width and $\text{sinc}^2(.)$ decay function. Hence, the signal from intracellular space is described as an integral with closed-form solution:

$$
\begin{aligned}
x_r(\mathbf{q},\Delta) &= \int_0^\infty x_r(q,\Delta,R)p(R)dR \\
&= \int_0^\infty \mathrm{sinc}^2(2Rq)\frac{R^{k-1}\exp\left(-r/\theta\right)}{\theta^k\Gamma(k)}dR \\
&= \frac{1}{4\pi^2 k\theta^2 q^2}\left[1-\frac{1}{\left(1+4\pi^2\theta^2q^2\right)^k}\right]
\end{aligned}
\tag{3.43}
$$

where $q = |\mathbf{q}|$. Here, it is assumed that the axon radii can be model by a two parameter gamma distribution described in Eq. (3.34).

The model parameters to be estimated are the volume fraction for the restricted compartment f, the gamma distribution parameters (shape parameter (k) and scale parameter (θ)) and the ADC value for the hindered part (D_h).

In order to estimate the parameters in the Generalised 1D model, one uses a series of PGSE measurements at different gradient field amplitudes with several diffusion times (Δ values).

3.10 Discussion

A number of models are presented in the literature to describe the geometry-related attenuation of DWMR signal in the brain white matter. Earlier models e.g. ADC proposed by Le Bihan et. al [109] and DTI presented by Basser et al. [149], provide simple and easy-to-use techniques to estimate the apparent diffusion coefficient (ADC) and apparent diffusion tensor (ADT) by assuming a Gaussian diffusion profile for the diffusion of water molecules in the brain tissue. Although, the non-Gaussian characteristics of the diffusion of particles in the brain white matter is now completely accepted, due to the simplicity, these models are widely used as a biomarker to determine the orientation of axons and the major changes in the brain microstructure, such as brain damage in stroke [151–154]. However, the markers derived from ADC and DTI, cannot be linked directly to the features of tissue microstructure and are related to a variety of different parameters simultaneously. For example, the size and packing density of axons, the permeability of cells membranes and axon myelination and the distribution of axon orientations, all affect the mean diffusivity and fractional anisotropy in a voxel. Therefore, a change in any of these markers cannot be identified exactly using these techniques [13].

More sophisticated techniques, assume the deviation of the DWMR signal decay from a mono-exponential function as an evidence for the existence of two or more compartments [101, 119–131, 134, 135]. Niendorf et al. [119] presented a Bi-exponential model for

describing the effect of "slow" and "fast" compartments corresponding to restricted and hindered diffusion respectively. Each compartment has its own diffusivity and volume fraction and the total signal is modelled as the weighted sum of the signals related to each compartment [13]. Stanisz et al. [101], presented a three compartment model for water molecules inside elongated ellipsoidal axons, inside spherical glial cells, and in the extracellular space. The statistical model proposed by Yablonskiy et al. [133] generalises this model and presents the signal as a sum of a large number of spin packets originating from different positions in the voxel, relating the microstructural features of the tissue with the distribution of ADC values.

Jensen et al. [136], has incorporated the deviation of signal from mono-exponential into kurtosis parameter and presented a two parameter model based on the cumulant expansion of $\ln(S/S_0)$ terminated in two terms, where the second term relates to the kurtosis of diffusion profile. On the other, since the approximation is valid only for the small diffusion weighting factors (b-values) and the range of b-values are usually considered much higher to sensitise the signal to the motion of the spins the approximations does not fall into the convergence region and the method fails. Moreover, the parameters derived from Kurtosis model, do not provide geometric related and physically sensible information about tissue microstructure.

Among the models developed to link the DWMR signal attenuation to the neural tissue microstructure, two compartment models have gain more interest as they propose more tissue related parameters in the models yet relatively simple models. Assaf et al. [100,105] presented a two compartment hindered/restricted model assuming parallel impermeable cylindrical axons in a homogeneous extracellular space. The model uses the GPD assumption and considers the signal from the restricted compartment as a combination of signals related to the diffusion parallel to fibre direction (modelled using Stejskal-Tanner equation, Eq. (2.57)), and the diffusion perpendicular to the fibre direction (modelled using Neuman's equation, Eq. (2.64)) for the diffusion inside a cylinder with radius R and using a constant gradient field ($\delta \sim \Delta$). The signal for hindered compartment is modelled considering the DTI model presented in Eq. (3.2). CHARMED utilises HARDI technique (measurements with different directions and different gradient weighting factors), to estimate the model parameters. It should be noted that, the CHARMED model assumes the long diffusion time limit ($\kappa \gg 1$) and constant gradient field ($\delta \sim \Delta$) to derive the model for the restricted compartment. Considering the typical diffusion times, typical length scales and the gradient field pulses used to perform the measurement, these assumptions are very unlikely to be satisfied.

Later, Assaf et al. [94,99] presented AxCaliber method based on a two compartment hindered/restricted model. The diffusion in the hindered compartment modelled using GPD

Table 3.1: Summary of the models used to describe DWMR signal decay

Model	Parameters	Complexity	Assumptions	Geometric interpretation
ADC	D	1	GPD	No
DTI	$\mathbf{D}$	6	GPD	No
Bi-exponential	D_h,D_r,f	3	GPD	Yes
Kurtosis	D,K	2	SGP	No
CHARMED	D_h,f,R	3	GPD, $\delta \sim \Delta$	Yes
AXCaliber	D_h,f,k,θ	4	SGP, GPD, Orientation	Yes
MMWMD	D_h,f,R	3	GPD	Yes
Generalised 1D	D_h,f,k,θ	4	SGP, GPD, Orientation	Yes

approximation Eq. (2.57) while the diffusion in restricted compartment is modelled using SGP Approximation Eq. (2.74). The AxCaliber model assumes a Gamma distribution for the axon radii and incorporates the axon diameter distribution into the model. AxCaliber uses measurements with several diffusion weighting factors but with a single direction (perpendicular to fibre direction) to capture the information about the underlying tissue microstructure. It also perform the measurements with different diffusion times in order to sensitises the signal to the restricted geometries. The limitations of this model are the need for a priori knowledge about the direction of the nerve fibres, high gradient field strength and long acquisition times.

The MMWMD model presented later by Alexander [106, 146], uses the GPD approximation to derive the equations describing the signal attenuation. Similarly to CHARMED, the model assumes the signal from restricted compartment as a combination of signals related to diffusion parallel and perpendicular to the fibre direction. However, it uses Van Gelderen's expression (Eq. (2.62)) in the long diffusion time limit ($\kappa \gg 1$) instead of Neuman's expression (Eq. (2.64)) for the case of constant gradient field ($\delta \sim \Delta$). It also considers the DTI model (Eq. (3.2)) for the signal from hindered compartment similarly to CHARMED. MMWMD also utilises measurements with different diffusion weighting factors and different gradient directions to capture the microstructural information.

In order to summarise the models presented in this chapter, we presented all the models along with their complexity (the number of parameters of the model to be estimated, which is the same as the minimum number of measurements needed), and the assumptions used to derive the models in Table 3.1.

3.11 Summary

In this chapter, we presented a review over a number of existing and state-of-the-art models developed to link the DWMR signal decay to the tissue microstructure in the brain. For the ease of comparison, we presented all the models using a single mathematical notation. Next, we analysed the assumption considered for deriving each model and linked them to the concepts presented in the previous chapter. This was followed by the analysis of the advantages and disadvantages of different models. At the end, we summarised all the models in a single table and compared the models in terms of their complexity, the underling assumptions and the possibility to interpret geometric information from using the models.

In the next chapter, we will basically consider two-compartment models which provide geometric information about the tissue microstructure and compare their performance in term of the minimum uncertainty of the estimations.

Chapter 4

Cramer-Rao Lower Bound analysis and model evaluation

In the previous chapter, we introduced a number of parametric models proposed in the literature to describe the signal attenuation in DWI due to natural diffusion of water in the brain white matter. Given a sufficiently rich data set, the parameters in a model may be estimated thus revealing the geometric nature of the white matter as "described" by the model. Because the models cannot describe the white matter, nor the signal properly there are inevitably two types of errors in the parameter estimation process. Firstly, there is a "bias" error. The model not being accurate implies that there is a best possible model with a non-zero residual error. Secondly, there is a "variance" error. A statistical error due to a lack of sufficient data to estimate any non-systematic error in the experimental data. There may also be a third type of error, if it were difficult to extract the parameter estimator from the experimental data, a so called algorithmic error may be present. Here to proceed, we assume that there is no algorithmic error. Moreover, we will present each model in an ideal experimental environment in which there is not any bias error either. The latter is unrealistic, but does focus on the intrinsic performance of the model with respect to our ability to reliably extract model parameters from a given dataset (produced by the model itself).

The disadvantage of this approach is that no two models are compared against the same dataset. However, if a model perform poorly under these ideal condition, it is clear that it will perform poorly and worse under a realistic test against realistic DWI data (not conforming to the model). In order to proceed, we use the Cramer-Rao Lower Bound (CRLB) as the tool to compare the variance of the models. Even though, because all models use different parametric (under different modelling) assumptions, we will need to

derive some figures of merit in order to facilitate the comparison. Quantities such as mean square error and normalised mean squared errors are envisaged.

Before engaging in this analysis, the chapter provides a basic overview of CRLB analysis. Next, it discusses the CRLB for the various models and compares their performance. Our conclusion is that most of the models as presented perform poorly and should be used with extreme caution in realistic estimation procedures.

4.1 Cramer-Rao Lower Bound

The model-based techniques are used to infer the parameters of the model from the measurement data. All the information we have is embodied in the observed data and the underlying likelihood function, which is a function of the model. The performance of the estimations is directly related to the likelihood function. In particular, the more the likelihood function is influenced by the unknown parameter the better the estimation of that parameter may be [155]. Therefore, understanding the sensitivity of the likelihood function to different parameters can provide us with a useful measure of performance.

The DWMR data consists of a set of signal intensities at a specific voxel of diffusion weighted magnetic resonance images. Noise in MRI is modelled as additive with a Rician distribution. The Rician noise for magnitude images can be approximated by a Gaussian noise with a certain bias in the mean value. However, it has been shown that for reasonably large SNR values ($SNR \geq 3$) this bias is negligible and the noise can be approximately modelled using a Gaussian distribution [156].

We assume that the model is the true representation of the observed data. The measurement data $\mathbf{y}$ can therefore be modelled as:

$$\mathbf{y}(\boldsymbol{\theta}) = \mathbf{x}(\boldsymbol{\theta}) + \boldsymbol{\epsilon}(\boldsymbol{\theta}) \tag{4.1}$$

where $\boldsymbol{\epsilon}$ is a random Additive White Gaussian Noise (AWGN) with $\boldsymbol{\epsilon} \sim \mathcal{N}(\mathbf{0}, \sigma_n^2\mathbf{I})$, and $\mathbf{y}$ and $\mathbf{x}$ are $(N \times 1)$ data and true signal vectors respectively.

$$\begin{aligned} \mathbf{y} &= [y_1, y_2, ..., y_N]^T \\ \mathbf{x} &= [x_1, x_2, ..., x_N]^T \end{aligned} \tag{4.2}$$

Here, each element of the measurement vector corresponds to the signal intensity of a particular voxel in the MR image, measured at a certain q and Δ value ($y_i = y(q_i, \Delta_i)$ and N is the total number of measurements.

The parameters to be estimated are collected in the parameter vector $\boldsymbol{\theta}$,

$$\boldsymbol{\theta} = \left[\sigma_n^2, \theta_1, \theta_2, ..., \theta_M\right] \tag{4.3}$$

where M is the number of parameters of the model.

Given that the noise's covariance matrix is diagonal, the joint probability density function can be written as:

$$p(\mathbf{y};\boldsymbol{\theta}) = \frac{1}{(2\pi\sigma_n^2)^{N/2}} \exp\left(-\frac{[\mathbf{y}-\mathbf{x}]^T[\mathbf{y}-\mathbf{x}]}{2\sigma_n^2}\right) \tag{4.4}$$

The log likelihood function can be written as:

$$\ln\left(p(\mathbf{y};\boldsymbol{\theta})\right) = -\frac{N}{2}\ln(2\pi\sigma_n^2) - \frac{[\mathbf{y}-\mathbf{x}]^T[\mathbf{y}-\mathbf{x}]}{2\sigma_n^2} \tag{4.5}$$

For any unbiased estimator $\boldsymbol{\theta}$ satisfying "regularity" condition:

$$E\left\{\frac{\partial \ln\left(p(\mathbf{y};\boldsymbol{\theta})\right)}{\partial\boldsymbol{\theta}}\right\} = \mathbf{0} \tag{4.6}$$

where $E\{.\}$ denotes the expectation with respect to $p(\mathbf{y};\boldsymbol{\theta})$ and defined as:

$$E\left\{\frac{\partial \ln\left(p(\mathbf{y};\boldsymbol{\theta})\right)}{\partial\boldsymbol{\theta}}\right\} = \int \frac{\partial \ln\left(p(\mathbf{y};\boldsymbol{\theta})\right)}{\partial\boldsymbol{\theta}}\, p(\mathbf{y};\boldsymbol{\theta})\, d\mathbf{y} \tag{4.7}$$

the Fisher information matrix $\mathbf{I}_{\boldsymbol{\theta}}$ is defined as:

$$[\mathbf{I}_{\boldsymbol{\theta}}]_{i,j} = -E\left\{\frac{\partial^2 \ln\left(p(\mathbf{y};\boldsymbol{\theta})\right)}{\partial\theta_i\partial\theta_j}\right\} \tag{4.8}$$

Taking the first derivative of Eq. (4.5) with respect to σ_n^2, and noting that

$$\frac{\partial\mathbf{x}}{\partial\sigma_n^2} = \mathbf{0} \tag{4.9}$$

we have:

$$\frac{\partial \ln\left(p(\mathbf{y};\boldsymbol{\theta})\right)}{\partial\sigma_n^2} = -\frac{N}{2\sigma_n^2} + \frac{[\mathbf{y}-\mathbf{x}]^T[\mathbf{y}-\mathbf{x}]}{2\sigma_n^4} \tag{4.10}$$

and taking the second derivative with respect to σ_n^2, we can write:

$$\frac{\partial^2 \ln\big(p(\mathbf{y};\boldsymbol{\theta})\big)}{\partial(\sigma_n^2)^2} = \frac{N}{2\sigma_n^4} - \frac{[\mathbf{y}-\mathbf{x}]^T[\mathbf{y}-\mathbf{x}]}{\sigma_n^6} \tag{4.11}$$

since $\mathbf{y}-\mathbf{x} = \boldsymbol{\epsilon} \sim \mathcal{N}(\mathbf{0}, \sigma_n^2\mathbf{I})$, the quadratic term $[\mathbf{y}-\mathbf{x}]^T[\mathbf{y}-\mathbf{x}]$ has chi-square distribution i.e.

$$[\mathbf{y}-\mathbf{x}]^T[\mathbf{y}-\mathbf{x}] \sim \chi^2 \tag{4.12}$$

and the expected value can be calculated as:

$$\begin{aligned} E\left\{\frac{\partial^2 \ln\big(p(\mathbf{y};\boldsymbol{\theta})\big)}{\partial(\sigma_n^2)^2}\right\} &= E\left\{\frac{N}{2\sigma_n^4}\right\} - E\left\{\frac{[\mathbf{y}-\mathbf{x}]^T[\mathbf{y}-\mathbf{x}]}{\sigma_n^6}\right\} \\ &= \frac{N}{2\sigma_n^4} - \frac{\mathrm{tr}(\sigma_n^2\mathbf{I})}{\sigma_n^6} = -\frac{N}{2\sigma_n^4} \end{aligned} \tag{4.13}$$

where $\mathrm{tr}(\sigma_n^2\mathbf{I})$ is the trace of the covariance matrix i.e. $\mathrm{tr}(\sigma_n^2\mathbf{I}) = N\sigma_n^2$.

Eq. (4.13) shows that the Fisher information for estimating noise variance (σ_n^2) is only depended on the number of samples and noise variance itself. Therefore, in order to simplify our analysis and since we are not interested in estimating the noise variance at this stage, we discard σ_n^2 from the parameter vector and re-write the parameter vector:

$$\boldsymbol{\theta} = [\theta_1, \theta_2, ..., \theta_M]^T \tag{4.14}$$

where M is the number of parameters to be estimated.

Using the same technique, we can write:

$$\frac{\partial \ln\big(p(\mathbf{y};\boldsymbol{\theta})\big)}{\partial\theta_i} = \frac{1}{\sigma_n^2}[\mathbf{y}-\mathbf{x}]^T\left[\frac{\partial\mathbf{x}}{\partial\theta_i}\right] \tag{4.15}$$

and

$$\begin{aligned}\frac{\partial^2 \ln\left(p(\mathbf{y};\boldsymbol{\theta})\right)}{\partial\theta_i\partial\theta_j} &= \frac{1}{\sigma_n^2}\frac{\partial}{\partial\theta_j}\left([\mathbf{y}-\mathbf{x}]^T\left[\frac{\partial\mathbf{x}}{\partial\theta_i}\right]\right)\\ &= \frac{1}{\sigma_n^2}\left[\frac{\partial}{\partial\theta_j}(\mathbf{y}-\mathbf{x})\right]^T\left[\frac{\partial\mathbf{x}}{\partial\theta_i}\right] + [\mathbf{y}-\mathbf{x}]^T\left[\frac{\partial^2\mathbf{x}}{\partial\theta_i\partial\theta_j}\right]\\ &= \frac{1}{\sigma_n^2}\left[-\frac{\partial\mathbf{x}}{\partial\theta_j}\right]^T\left[\frac{\partial\mathbf{x}}{\partial\theta_i}\right] + [\mathbf{y}-\mathbf{x}]^T\left[\frac{\partial^2\mathbf{x}}{\partial\theta_i\partial\theta_j}\right] \end{aligned} \tag{4.16}$$

Taking expectation and knowing that $E\{\mathbf{y}-\mathbf{x}\} = \mathbf{0}$, the Fisher information matrix can be written as:

$$\begin{aligned}[\mathbf{I}_{\boldsymbol{\theta}}]_{i,j} &= -E\left\{\frac{\partial^2 \ln\left(p(\mathbf{y};\boldsymbol{\theta})\right)}{\partial\theta_i\partial\theta_j}\right\}\\ &= -E\left\{\frac{1}{\sigma_n^2}\left[-\frac{\partial\mathbf{x}}{\partial\theta_j}\right]^T\left[\frac{\partial\mathbf{x}}{\partial\theta_i}\right] + [\mathbf{y}-\mathbf{x}]^T\left[\frac{\partial^2\mathbf{x}}{\partial\theta_i\partial\theta_j}\right]\right\}\\ &= \frac{1}{\sigma_n^2}\left[\frac{\partial\mathbf{x}}{\partial\theta_j}\right]^T\left[\frac{\partial\mathbf{x}}{\partial\theta_i}\right] \end{aligned} \tag{4.17}$$

The Fisher information indicates the sensitivity of the model to each parameter. The CRLB matrix is the reciprocal of the Fisher information matrix [157]. Therefore, we can find CRLB for estimated parameters as:

$$\begin{aligned}\mathrm{var}(\hat{\sigma_n}^2) &\geq \frac{2\sigma_n^4}{N}\\ \mathrm{var}(\hat{\theta_i}) &\geq \left[\mathbf{I}_{\boldsymbol{\theta}}^{-1}\right]_{i,i}\end{aligned} \tag{4.18}$$

Here $\left[\mathbf{I}_{\boldsymbol{\theta}}^{-1}\right]_{i,i}$ denotes the diagonal element of the inverse Fisher information matrix situated on row i and column i. Eq. (4.18) indicates the effect of the noise variance, the number of samples and the model on the lower bound.

Generalizing the analysis above and considering the derivation of Fisher information matrix for the case of AWGN with $E\left\{\boldsymbol{\epsilon}\boldsymbol{\epsilon}^T\right\} = \boldsymbol{\Sigma}$, and assuming,

$$\frac{\partial\boldsymbol{\Sigma}}{\partial\theta_i} = \mathbf{0} \tag{4.19}$$

the Fisher information matrix becomes:

$$[\mathbf{I}_{\boldsymbol{\theta}}]_{i,j} = \left[\frac{\partial\mathbf{x}}{\partial\theta_i}\right]^T\boldsymbol{\Sigma}^{-1}\left[\frac{\partial\mathbf{x}}{\partial\theta_j}\right] \tag{4.20}$$

For the special case when $\boldsymbol{\Sigma} = \sigma_n^2\mathbf{I}$, Eq. (4.20) reduces to Eq. (4.17).

4.2 Model evaluation using CRLB

In this section, we utilise the Cramer-Rao Lower Bound to calculate the minimum uncertainty levels of a number of models presented in the previous chapter. We consider the best-scenario for each model, by which we neglect the estimation bias and assume that the measurement data originated from the model itself (The model is completely true representation of the data). The analyses compare the sensitivity of the model parameters to the noise levels and give us an understanding about the reliability of the estimations without considering the capability of the models in fitting real data (non-model data).

The CRLB analysis for each model, is performed by calculating the Fisher information matrix for all the possible combinations of acquisition and tissue related parameters. In this work, we only consider the single-PGSE acquisition regime for which the acquisition parameters are the maximum gradient field amplitude (G_{max}), the gradient pulse width (δ), diffusion time (Δ) and the number of measurements (N) at different q-values. The tissue related parameters are different for different models. The analyses have been performed for a range of practical acquisition and typical tissue related parameters. The range of parameters used in the CRLB analysis for all models is presented in Table 4.1. The range of acquisition parameters is chosen in alignment with the range of values for existing human and animal scanners. The range is however larger to allow us exploration of the models under more favourable conditions, and predict somewhat the potential of the models when used in conjunction with future scanners. The ranges for maximum gradient amplitude is chosen such that they result into q values from 0.01 [μm^{-1}] to 0.1 [μm^{-1}], which is more than what is achievable in the existing clinical scanners. However, this will lead to a knowledge about the predicted performance for higher gradient field amplitudes. The range of tissue related parameters is chosen based on the typical values for human white matter acquired from histological studies. All the parameter intervals have been divided to the particular number of steps (presented in the Table 4.1) linearly.

We analyse the two compartment hindered/restricted models which have the capability of providing geometrically related information (see Table 3.1). The models considered for this comparative analysis are Bi-exponential [119], CHARMED [105], AxCaliber [99] and Generalised 1D [104]. The number and the physical nature of the parameters of each model vary which makes it complicated to provide a comparative analysis of the models. The bounds presented in Eq. (4.18), determine the minimum variance for an unbiased estimator [157]. Therefore, in order to normalise the error with respect to the parameter itself, and present it as a unit-less variable, we introduce the relative error ratio (RER) defined by:

Table 4.1: Range of acquisition (top) and tissue related (bottom) parameters used for CRLB analysis of all models

Parameter	[unit]	Min. value	Max. value	Number of steps
G_{max}	[mT/m]	47	986	21
N	-	6	20	8
Δ	[ms]	20	100	5
δ	[ms]	5	5	1
D_h	[μm^2/ms]	0.1	2.9	15
D_r	[μm^2/ms]	0.05	1.15	12
f	-	0.1	0.9	9
R	[μm]	0.5	4	8

$$\mathrm{RER}(\theta_i) = \frac{\sigma_{min}(\theta_i)}{\theta_i} = \frac{\sqrt{\min\left(\mathrm{var}(\theta_i)\right)}}{\theta_i} \tag{4.21}$$

where $\sigma_{min}(\theta_i)$ denotes the minimum standard deviation of parameter θ_i calculated as

$$\sigma_{min}(\theta_i) = \sqrt{\left[\mathbf{I}_{\boldsymbol{\theta}}^{-1}\right]_{i,i}} \tag{4.22}$$

The RER provides a quantitative measure for the minimum uncertainty level of each model parameter given a set of measurement and model parameters. Using RER, we can map all the minimum error levels for different parameters and different models into a normalised scale, in which the RERs can be used to compare the performance of the models. In order to produce a single figure of merit for the comparison of different models, we use the total RER defined as the sum of the RERs for all the model parameters (i.e. trace of the CRLB matrix divided by the true values of the parameters) for each model.

It may be observed that we present as a total figure of merit for a model the sum of the relative errors for each relevant parameter in the model. One may object to this on the ground of adding "totally unrelated quantities", and furthermore, one may object to comparing models on the basis of their total RER, because the models do not even share the same variables. These observations are correct. Nevertheless, relative errors are expressed in per unit, and indicate how poorly a particular parameter can be recovered under the "best possible data scenario". Hence, the sum of the RERs does reflect the quality or better, the lack of quality of a model under the best possible data scenario (i.e. one where the measurement data were derived from the model). As a consequence, we feel justified to use the sum of the relative errors as a total figure of merit of any single model

and moreover, feel justified in comparing models based on this figure of merit. The larger the figure of merit, the more problematic the model is.

We simplify all the models to strictly two compartment hindered/restricted model for which, the net normalised DWMR signal decay is described by Eq. (3.9). We also consider the models for the case of a single direction PGSE sequence and assume a priori knowledge about the orientation of the fibres. The gradient field direction is assumed perpendicular to the fibre directions. We also simplify all the models to the case of singe radius axons (mean axon radius). However, it is clear that increasing the complexity of the models will increase the uncertainty levels and reduce the performance. Here we consider the best-case scenarios. The performance of the models under more realistic conditions will be worse than what is calculated here. The analyses in this step, provide the lower bounds for the uncertainty of the models under an unrealistic best-case scenario. Performance under practical conditions will be worse than what is calculated here.

For each model we consider two different estimation approaches. The first approach called single-Δ uses the information from different measurements with different gradient field amplitude but a single diffusion time, while the second approach called multiple-Δ utilises the information from all the measurements at different gradient amplitudes and for all different diffusion times. It can also be stated that the second method will result in lower RERs as it uses more information in comparison to the first approach.

We consider the noise as AWGN and set Signal to Noise ratio, $SNR = \sigma_n^{-1} = 10$ in CRLB analyses for all models. Theoretically, the performance of the models will be improved by increasing the SNR due to the inverse relation between SNR and RER (Eq. (4.17) and Eq. (4.18)).

A reasonable range for the RER would be 0.1 which represents 10% relative error i.e. under the best-scenario assumptions, the estimated parameters will have 10% uncertainty.

4.2.1 Results for Bi-exponential model

Table 4.2: Range of hindered diffusion coefficient (D_h) used for CRLB analysis of B-exponential model

Parameter	[unit]	Min. value	Max. value	Number of steps
D_h	[μm^2/ms]	1.5	2.9	15

The Bi-exponential model [119] for hindered and restricted signal decay models are presented in Eq. (3.10) and Eq. (3.11) respectively. The net DWMR signal decay is modelled

Table 4.3: Minimum RER values for bi-exponential model using single-Δ estimation approach

Min. Avrg. RERs	RER(D_h)	RER(D_r)	RER(f)	Total RER
RER(D_h)	**2.66**	2.72	2.66	2.66
RER(D_r)	2.56	**2.50**	2.56	2.56
RER(f)	7.32	7.51	**7.32**	7.32
total RER	12.54	12.73	12.54	**12.54**
G_{max} [mT/m]	188	188	188	188
N	20	20	20	20
Δ [ms]	80	100	80	80

by a two compartment hindered/restricted diffusion model as presented in Eq. (3.9). The tissue related parameters of the bi-exponential model to be estimated are the hindered (fast) and restricted (slow) diffusion coefficients (D_h and D_r respectively) and the volume fraction (f). The range of the measurement and tissue related parameters is presented in Table 4.1. In order to prevent the singularity of the model (when $D_h = D_r$), we changed the range of D_h in a way to remove any overlapping with the range of D_r. The range of D_h used for the CRLB analysis for Bi-exponential model is presented in Table 4.2

The CRLB analysis has been performed and the minimum average RER values for different parameters as well as the minimum total average RER are calculated. The results for single- and multiple-Δ approaches are presented in Table 4.3 and Table 4.4 respectively. The values of average RER for each parameter is also presented along with the set of measurement parameters resulting in the minimum average RERs at each step.

As it can be understood from the results, the minimum average RERs for bi-exponential model are high even considering the case when the "fast" and "slow" diffusion coefficients (D_h and D_r) are completely separated. In order to have reasonable estimations, very high

Table 4.4: Minimum RER values for bi-exponential model using multiple-Δ estimation approach

Min. Avrg. RERs	RER(D_h)	RER(D_r)	RER(f)	Total RER
RER(D_h)	**1.24**	1.30	1.24	1.24
RER(D_r)	1.19	**1.19**	1.19	1.19
RER(f)	3.54	3.68	**3.54**	3.54
total RER	5.97	6.16	5.97	**5.97**
G_{max} [mT/m]	235	282	235	235
N	20	20	20	20

SNR values are required which limits the application of bi-exponential model for practical applications.

Table 4.5: Minimum RER values for CHARMED model using single-Δ estimation approach

Min. Avrg. RERs	RER(D_h)	RER(f)	RER(R)	Total RER
RER(D_h)	**0.74**	0.83	0.80	0.80
RER(f)	0.20	**0.13**	0.36	0.36
RER(R)	912.74	341.38	**115.28**	115.28
total RER	913.68	342.34	116.44	**116.44**
G_{max} [mT/m]	611	986	986	986
N	20	20	20	20
Δ [ms]	80	100	20	20

4.2.2 Results for CHARMED model

The restricted and hindered signal models for CHAMRED [100, 105], is presented in Eq. (3.23) and Eq. (3.27) respectively. The net DWMR signal decay uses a two compartment model described in Eq. (3.9). For the ease of calculation, we assume symmetric gradient pulse sequence i.e. $\tau \approx \Delta$. Since for this comparative study, it is assumed that the fibre orientation is known and is perpendicular to the gradient direction, the parallel component of the gradient $G_{\parallel}$ is zero and the restricted signal models is simplified to:

$$x_r(\mathbf{q}, \Delta) = \exp\left(\frac{-4\pi^2 R^4 q^2}{D_0 \Delta} \times \frac{7}{296} \times \left(2 - \frac{99}{112}\right) \times \frac{R^2}{D_0 \Delta}\right) \tag{4.23}$$

where D_0 is the diffusivity perpendicular to the fibre direction, which is assumed equal to the intrinsic diffusivity of the medium, R is the axon radius, Δ is the diffusion time and q is the reciprocal wave number calculated from Eq. (2.45). The signal from hindered compartment also simplifies to

Table 4.6: Minimum RER values for CHARMED model using multiple-Δ estimation approach

Min. Avrg. RERs	RER(D_h)	RER(f)	RER(R)	Total RER
RER(D_h)	**0.24**	0.31	0.31	0.31
RER(f)	0.07	**0.05**	0.05	0.05
RER(R)	327.81	45.59	**45.59**	45.59
total RER	328.12	45.96	45.96	**45.96**
G_{max} [mT/m]	376	986	986	986
N	20	18	18	18

$$x_h(\mathbf{q}, \Delta) = \exp\left(-4\pi^2 q^2 (\Delta - \frac{\delta}{3}) D_h\right) \tag{4.24}$$

where D_h is the diffusivity of water molecules perpendicular to the axon direction in the extra-axonal space.

The model assumes a priori knowledge of the diffusivity of water particles in the intra-axonal space (D_0) and typically one selects the intrinsic diffusivity of water ($D_0 \approx 2 \times 10^{-9}$ [$\mathrm{m^2 s^{-1}}$]). Therefore, the parameters of the model to be estimated are the ADC in hindered compartment (D_h), the volume fraction of restricted compartment (f) and the (mean) axon radius R.

The results for CRLB analysis of CHARMED model under single- and multiple-Δ estimation approaches are presented in Table 4.5 and Table 4.6 respectively. The results show that at the best case, the total RER will fall below 10% for $SNR \geq 459.6$, which is not be possible in practice. The typically achievable SNR is human scanners is in the order of 30. It should also be noted that the increase in the SNR needs more measurements which results in a dramatical increase in the acquisition time.

Table 4.7: Minimum RER values for single radius AxCaliber model using single-Δ estimation approach

Min. Avrg. RERs	RER(D_h)	RER(f)	RER(R)	Total RER
RER(D_h)	**0.61**	0.76	0.85	0.71
RER(f)	0.21	**0.17**	0.17	0.23
RER(R)	3.56	0.53	**0.33**	0.39
total RER	4.38	1.46	1.34	**1.32**
G_{max} [mT/m]	282	705	986	986
N	20	20	20	20
Δ [ms]	100	100	100	20

4.2.3 Results for AxCaliber model

The CRLB analysis of AxCaliber [99] was performed considering the assumption of single (mean) radius axon. The two compartment hindered/restricted AxCaliber models the net DWMR signal decay as a weighted sum of contributions from hindered and restricted compartments as presented in Eq. (3.9). The signal from restricted compartment is presented in Eq. (3.32) for an axon with radius R. AxCaliber considers the assumption of perpendicular gradient field direction with respect to axon direction. Hence, the signal decay for hindered component can be used without any alteration as presented in Eq. (3.31). The intrinsic diffusivity of water in the biological tissue is assumed $D_0 \approx 2 \times 10^{-9}$ [$m^2 s^{-1}$].

The tissue related parameters of the model in the single axon version are the diffusivity of extra-axonal compartment (D_h), the volume fraction for the restricted compartment (f)

Table 4.8: Minimum RER values for single radius AxCaliber model using multiple-Δ estimation approach

Min. Avrg. RERs	RER(D_h)	RER(f)	RER(R)	Total RER
RER(D_h)	**0.24**	0.30	0.33	0.33
RER(f)	0.10	**0.08**	0.08	0.08
RER(R)	1.54	0.24	**0.15**	0.15
total RER	1.88	0.62	0.57	**0.57**
G_{max} [mT/m]	282	705	986	986
N	20	20	20	20

and the axon radius (R). The range of acquisition and tissue related parameters used for analysis of AxCaliber model is presented in Table 4.1. The results for CRLB analysis of AxCaliber model using single- and multiple-Δ approaches are presented in Table 4.7 and Table 4.7 respectively.

For the multiple-Δ approach, the total average RER fall below 10% for SNR $\geq$ 57 which is difficult t achieve under clinical conditions. Moreover, in order to have accurate estimations the number of measurements should be at the maximum ($N = 20$), and considering the fact that the measurements should be performed for all the different diffusion times (20, 40, 60, 80, 100) the total number of measurements needed is 100. This will increase the measurement time and cost dramatically and can be considered as a barrier in application of this method in clinic. On the other hand, in order to have accurate estimations, a huge gradient field amplitude should be applied ($G_{max} = 986$ [mT/m]), which is not applicable using the existing clinical scanners and implies a number of design and safety constraints.

Table 4.9: Minimum RER values for MMWMD model using single-Δ estimation approach

Min. Avrg. RERs	RER(D_h)	RER(f)	RER(R)	Total RER
RER(D_h)	**2.52**	2.53	2.58	2.53
RER(f)	17.40	**17.24**	17.48	17.24
RER(R)	1.22	1.18	**1.18**	1.18
total RER	21.14	20.95	21.23	**20.95**
G_{max} [mT/m]	611	658	705	658
N	20	20	20	20
Δ [ms]	80	80	80	80

4.2.4 Results for MMWMD model

The MMWMD model [106, 146] utilises a two compartment hindered/restricted model as presented in Eq. (3.9) to model the net DWMR signal decay. The contributions from restricted and hindered compartments are presented in Eq. (3.39) and Eq. (3.40) respectively. Here, we consider the MMWMD model under the assumption of single direction PGSE for which the direction of gradient field is assumed perpendicular to axon direction. Therefore, the model for the contribution from the restricted compartment is simplified to:

$$x_r(\mathbf{q}, \Delta) = \exp\left(-4\pi^2 q^2 R^2\right) \tag{4.25}$$

where $q = |\mathbf{q}|$ is the reciprocal wavenumber and R is the axon radius. Based on the above assumption, the signal from hindered compartment can also be simplified to Eq. (3.10).

The CRLB analysis was performed for all the possible combinations of measurement

Table 4.10: Minimum RER values for MMWMD model using multiple-Δ estimation approach

Min. Avrg. RERs	RER(D_h)	RER(f)	RER(R)	Total RER
RER(D_h)	**0.29**	0.29	0.39	0.32
RER(f)	0.16	**0.16**	0.20	0.17
RER(R)	0.31	0.25	**0.15**	0.18
total RER	0.75	0.70	0.74	**0.66**
G_{max} [mT/m]	376	423	939	564
N	20	20	20	20

and tissue related parameters presented in Table 4.1. The results of CRLB analysis for MMWMD model using single- and multiple-Δ approaches are presented in Table 4.9 and Table 4.10 respectively.

As it can be inferred from the results, the minimum average RERs for MMWMD is slightly higher than AxCaliber model and the RERs fall below 10% for $SNR \geq 66$. However, the maximum gradient field needed to achieve the minimum RERs in this technique ($G_{max} = 564$), which is less than what was needed for AxCaliber.

The total RER are reduced in general as the number of measurements and maximum gradient field amplitude increases giving the idea that in order to obtain better estimations, more measurements and higher gradient fields are required. For this model also the minimum total average RER value could be obtained by having large number of measurements ($N = 20$) and by using all different diffusion times. Increasing the number of measurements will lead to increase in the scanning time and cost, while increasing the maximum gradient field runs into physical design obstacles and safety concerns. In general such gradient fields cannot be implemented in clinical scanners. Therefore, the application of these methods in clinical studies using existing clinical scanners is not practical.

Table 4.11: Minimum RER values for single radius Generalised 1D model using single-Δ estimation approach

Min. Avrg. RERs	RER(D_h)	RER(f)	RER(R)	Total RER
RER(D_h)	**0.86**	0.92	1.47	0.92
RER(f)	0.37	**0.31**	0.36	0.31
RER(R)	0.68	0.35	**0.26**	0.35
total RER	1.92	1.58	2.09	**1.58**
G_{max} [mT/m]	94	141	235	141
N	20	20	20	20
Δ [ms]	100	100	100	100

4.2.5 Results for Generalised 1D model

The generalised 1D model [104] utilises a two compartment hindered/restricted model for the net DWMR signal decay presented in Eq. (3.9). The experimental method assumes a priori knowledge about the orientation of the axons. The direction of the gradient field vector is assumed perpendicular to the fibre direction. The signal from the hindered compartment is modelled using a Gaussian diffusion approximation as presented in Eq. (3.10). Since, we consider the simple case of single (mean) axon radius, the signal from restricted water molecules inside an axon with radius R is modelled as:

$$x_r(\mathbf{q}, \Delta) = \text{sinc}^2(2Rq) \tag{4.26}$$

The CRLB analysis was performed for all possible combinations of acquisition and tissue related parameters presented in Table 4.1 and the RERs were calculated. The results for CRLB analysis of Generalised 1D model for single- and multiple-Δ approaches are

Table 4.12: Minimum RER values for single radius Generalised 1D model using multiple-Δ estimation approach

Min. Avrg. RERs	RER(D_h)	RER(f)	RER(R)	Total RER
RER(D_h)	**0.29**	0.30	0.51	0.35
RER(f)	0.16	**0.11**	0.15	0.12
RER(R)	1.28	0.29	**0.11**	0.16
total RER	1.73	0.71	0.78	**0.62**
G_{max} [mT/m]	47	94	282	141
N	20	20	20	20

presented in Table 4.11 and Table 4.12 respectively.

For the Multiple-Δ approach the total average RER will fall below 10% for $SNR \geq 62$. The minimum total RER is obtained at the maximum number of measurements ($N = 20$). However, the maximum gradient amplitude needed is lower than other techniques, which can be considered as an advantage for this model.

4.3 Summary

In this chapter, we investigated the performance of a number of models used for describing diffusion weighted MR signal decays. We utilised the CRLB as a tool to analyse the minimum variance of an unbiased estimator. Our analysis was performed in the ideal and unrealistic sitting that the data are derived from the model and AWGN. We calculated the CRLBs for a range of acquisition and tissue related parameters and calculated the RERs for all the combinations of the parameters. In order to calculate the minimum total RER for each model, we found a particular combination of acquisition parameters which results in the minimum total average RER. The average is taken over all the RER values for different possible combinations of tissue related parameters.

The models were simplified for the case of approximating single (mean) axon radius and the direction of fibres were assumed to be known and perpendicular to the gradient field direction. The minimum total average RERs for different models are presented in Table 4.13. Theoretically, RERs will decrease by increasing the SNR and one should keep in mind that by increasing the SNR by factor K all the RER values presented in Table 4.13 will be divided by the factor K. The results demonstrate that, none of the models could provide estimation with reasonable uncertainty level (RER ≤ 0.1) under normal SNR and ideal unrealistic model validity.

Table 4.13: Minimum total average RER values for all models using multiple-Δ estimation approach

Model	Bi-exp.	CHARMED	AxCaliber	MMWMD	G.1D
Min. Total Avrg. RER	**5.97**	**45.96**	**0.57**	**0.66**	0.62
Avrg. RER(D_h)	1.24	0.31	0.33	0.32	0.35
Avrg. RER(D_r)	1.19	-	-	-	-
Avrg. RER(f)	3.54	0.05	0.08	0.17	0.12
Avrg. RER(R)	-	45.59	0.15	0.18	0.16

Theoretically, an increase in the number of measurements results in the decrease in the Total average RER. On the other hand, an increase in the maximum field gradient can lead to higher Total RER, because of the effect of the faster signal decay at higher diffusion times and loss of signal. It can be shown that for higher diffusion times the DWMR signal will drop sharply and obtaining more measurement with higher gradient amplitudes will not produce more information (Since the SNR drops dramatically).

Chapter 5

Simulation framework

In order to be able to compare different techniques and estimate the accuracy of each model, we need to develop a simulation framework, which has the behaviour as similar as possible to the real biological tissue. The simulation framework for this project should be able to model the axon placement and water molecule diffusion and calculate the accumulated phase and displacement. The phase distribution then can be used to estimate the DWMR signal decay and fit the model.

The simulation framework we have developed consists of two parts:

1. Axon Packing: This routine simulates the placement of axons (of various diameters).
2. Signal modelling: In this routine, the diffusion of water molecules in the simulated tissue is modelled, and the resulting phase distribution is computed and used to produce simulated data of the DWMR signal.

5.1 Axon Packing Algorithms

Modelling of the placement of axons in a nerve bundle plays an important role in the investigation of the axon diameter distribution using DWI. Based on the images obtained from electron microscopy, the axon radii in a nerve bundle can be well modelled by a gamma distribution [99]. The probability density function of the gamma distribution is given by Eq. (3.34). In this part, we present a technique for simulating axon packings in nerve fibres based on a dynamic and constructive approaches.

From visual inspection of the microscopy images, the axons within a nerve bundle are packed together (see Figure 2.4(b)). In order to simulate the axons and restricted water

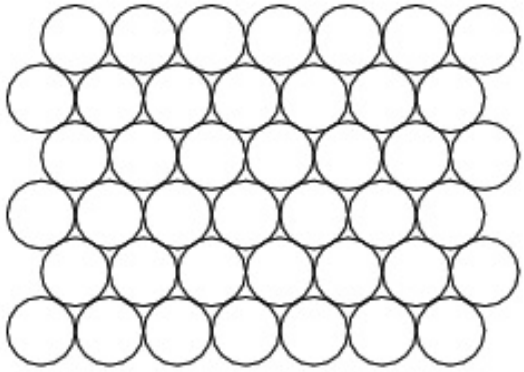

Figure 5.1: Hexagonal circle packing

diffusion, the structure of packing and the distribution of axon radii must be considered.

The model consists of a voxel (a rectangle) with width and height W filled with circles (axons) with the radii r_i generated from a gamma distribution. The circles are separated by interfaces with specific thickness (h) called boundaries and there is no overlap between any two circles. The problem is to distribute the circles in a rectangle considering the desired packing density. The packing density in this context is defined as the proportion of surface area occupied by the circles in a voxel. This density depends on the size distribution of axons, the thickness of boundaries and the way the axons are packed. Therefore, the problem of packing axons in a voxel is similar to packing circles inside a rectangle. Joseph Louis Lagrange proved in 1773 that in particular case where circles have identical size in two dimensional Euclidean space the, the highest density is the hexagonal packing arrangement, in which the centers of the circles are arranged in a hexagonal lattice, and each circle is surrounded by 6 other circles as depicted in Figure 5.1. The density of this arrangement is $\pi/\sqrt{12} \approx 0.9069$ [158, 159].

In the case that we know that the radii distribution is derived from a gamma distribution, we can estimate the number of axons resulting in a particular packing density. The expected value for the area of a circle with a radius derived from a gamma distribution is:

$$E\{A\} = \int_0^\infty \pi r^2 p(r) dr. \tag{5.1}$$

where $p(r)$ is the probability density function of gamma distribution as given by Eq. (3.34). By substituting Eq. (3.34) into Eq. (5.1), the expected value for the area of an axon is the solution of the following integral:

$$E\{A\} = \frac{\pi}{\Gamma(k)\theta^k} \int_0^\infty r^{k+1} \exp(-r/\theta) dr$$
$$= \pi \frac{\Gamma(k+2)\theta^2}{\Gamma(k)} \tag{5.2}$$

where $\Gamma(k)$ denotes the gamma function as given by Eq. (3.35).

Therefore, the number of circles can be estimated as:

$$N_A = \frac{W^2 f_r}{E\{A\}} \tag{5.3}$$

where W is the width of the voxel and f_r is the packing density which is a real number and $f_r \in (0, 1)$.

In designing our simulation algorithm, we have considered two different approaches for filling a square with circles, which are Dynamic and Constructive approach.

5.1.1 Dynamic Approach

In the dynamic approach, for the placement of a new circle the information about the position of previous circles is not considered. The only constraint here is that any two circles do not intersect with each other. Therefore, after selecting the values for radius and centre coordinates, the intersection of the new circle with previous circles is checked to decide whether to keep the current position or not. In this particular problem we are strict about the size distribution of the axons, in the case of any intersection between the new and previous circles, the size of the circle cannot be changed and a new centre coordinates for the circle is tried. Usually the dynamic method is not computationally efficient and is quite time consuming especially for the cases with high packing density [158]. A simple outcome of the dynamic packing approach is depicted in Figure 5.2. The axon radii distribution histogram and probability density function fitting is shown in Figure 5.3. Since in the dynamic method, there is a possibility that for a particular radius value there would be no available place in the voxel to fit the circle, we have to discard some random values after certain number of failed trials. Consequently, the probability density function in dynamic method does not match the expected curve accurately.

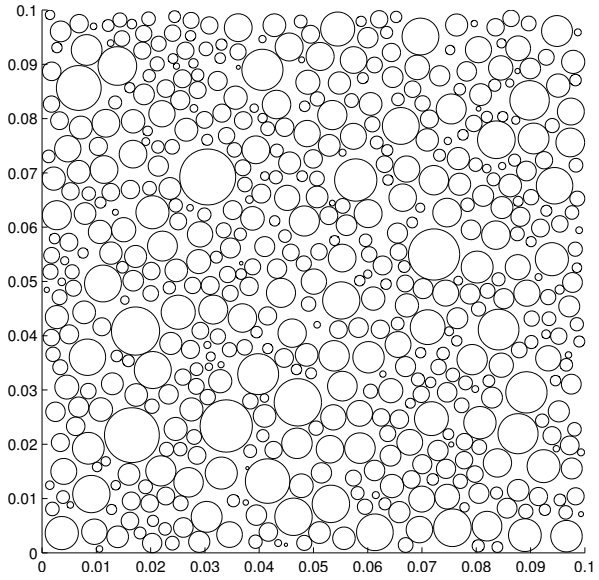

Figure 5.2: Dynamic axon packing algorithm results with W = 100 μm , $f_r = 0.6$, $k = 4$ and $\theta = 5 \times 10^{-4}$

5.1.2 Constructive Approach

In the constructive approach, the position of a new axon is determined using the information from previously placed axons. The algorithm starts with a circle in the centre of the voxel continuing in the levels around the first circle. In order to have the structure as dense as possible in each step, the boundary for new circle is in contact with the boundaries of two previously placed circles.

The constructive approach utilises the concept of advancing neighbours in which each neighbour is a pointer to a circle adjacent to the new circle. In order to place a new circle, the information of the placement of two previously placed neighbours is used.

A pseudo-code description of constructive algorithm is:

1. Produce N_A radii based on the gamma distribution with desired parameters, k and θ.

2. Place the first circle in the centre of the voxel i.e. $(x_1, y_1) = (W/2, W/2)$.

3. Create the first neighbour L_1 and set it to 1, i.e. $L_1 = 1$.

4. Place the centre of the second circle (x_2, y_2) with the constraint to be on the circle

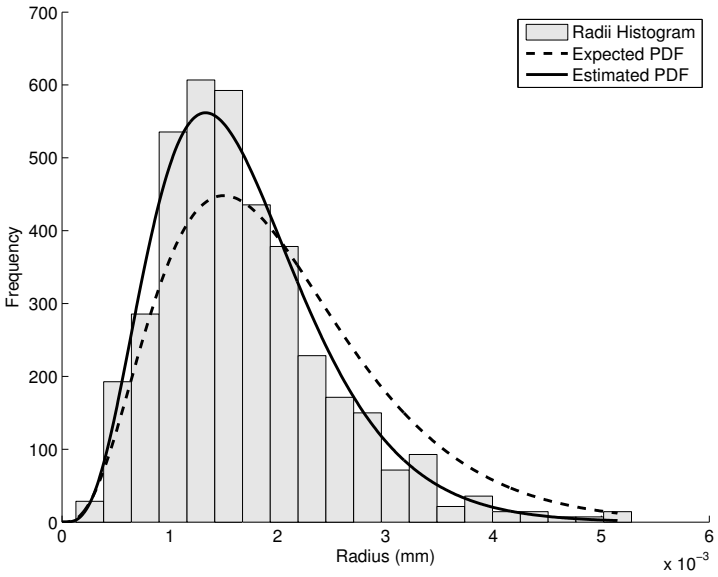

Figure 5.3: Dynamic axon packing radii distribution histogram and expected and estimated PDF curves with $W = 0.1$ mm and $f_r = 0.6$, $k = 4$ and $\theta = 5 \times 10^{-4}$

with the following equation:

$$x_2^2 + y_2^2 = (r_1 + h_1 + r_2 + h_2)^2, \tag{5.4}$$

Here, r_1 and h_1 are the radius and boundary thickness of the first axon and, r_2 and h_2 are the radius and boundary thickness of the second axon respectively. This constraint guarantees that the boundary of the second circle will be in contacts with the boundary of the first circle.

5. Create the second neighbour L_2 and set its value to 2 to point to the second circle, i.e. $L_2 = 2$.

6. for i=3 to N_A
   place the new circle with radius r_i at the centre with coordinates (x_i, y_i) with the constraint to satisfy the following system of equations:

$$\begin{cases} (x_i - x_{L_1})^2 + (y_i - y_{L_1})^2 = (r_{L_1} + h_{L_1} + r_i + h_i)^2 \\ (x_i - x_{L_2})^2 + (y_i - y_{L_2})^2 = (r_{L_2} + h_{L_2} + r_i + h_i)^2 \end{cases} \tag{5.5}$$

Here, (x_i, y_i) is the coordinates for the centre of the i-th axon. The set of coordinates (x_{L_1}, x_{L_1}) (x_{L_2}, x_{L_3}) are the centre of the first and second neighbours respectively. These equations guarantee that the new circle's boundary is in contact with the L_1 and L_2 neighbors as depicted in Figure 5.4.

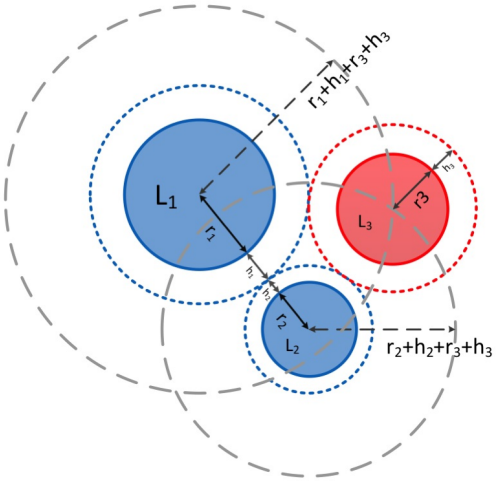

Figure 5.4: Placement of the new circle with regard to the first and second neighbours

7. for j=1 to i
   Check the intersection of the new circle with centre coordinate (x_i, y_i) and radius r_i and the j-th circle with centre (x_j, y_j) and radius r_j using the following equation:

$$\|(x_i, y_i) - (x_j, y_j)\| < (r_i + h_i + r_j + h_j) \tag{5.6}$$

8. If two circles intersect, discard the centre coordinate (x_i, y_i) and increment L_1, i.e. $L_1 = L_1 + 1$.

9. If $L_1 = L_2$, decrement L_2, i.e. $L_2 = L_2 - 1$, set $L_1 = 1$ and go to 6
   else keep the coordinates, increment i and go to 6.

The results of the constructive packing approach is depicted in Figure 5.5. The histogram and probability density function of the axon radii distribution using constructive approach is also demonstrated in the Figure 5.7. The distribution of the radii using the constructive approach gives better results in comparison with the dynamic method.

5.1.3 The relationship between boundary thickness and packing density

Thickness parameter (h) is a representative of the boundary thickness of axons and is the ratio of the boundary thickness to axon radius. In the simulations we consider $h \in [0, 1]$. However it can be greater than one if needed.
The packing density can be altered by changing the thickness parameter. Figure 5.6 shows the relationship between the packing density and thickness parameter. By increasing the

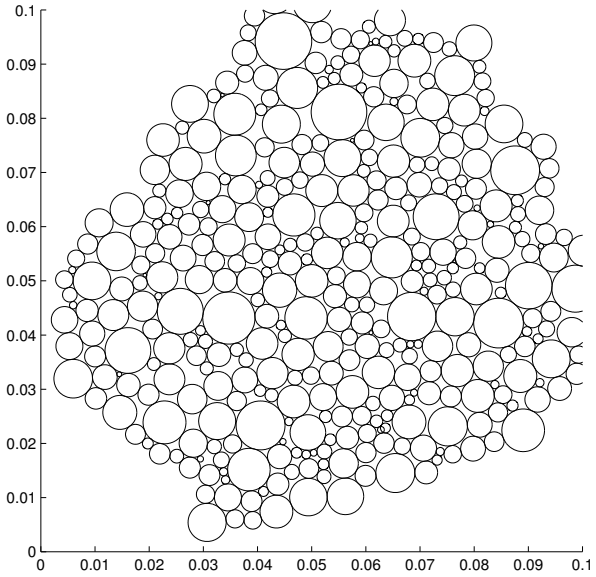

Figure 5.5: Constructive axon packing algorithm results with $W = 0.1$ mm, $f_r = 0.6$, $k = 4$ and $\theta = 5 \times 10^{-4}$.

thickness parameter, the number of axons in the voxel is decreased approximately by a factor of $(1 + h)^2$:

$$N_A \approx \frac{W^2 f_{r0}}{(1 + h)^2 E\{A\}} \tag{5.7}$$

where f_{r0} is the mean value for the maximum packing density which can be achieved for $h = 0$. For dynamic method $f_{r0} = 0.55$ and for constructive method $f_{r0} = 0.85$. Hence, the relationship between the packing density and the thickness parameter can be written as:

$$f_r(h) = N_A \times \frac{E\{A\}}{W^2} \approx \frac{f_{r0}}{(1 + h)^2} \tag{5.8}$$

Eq. (5.8) can be used to determine the desired packing density of the model and reduce the model parameters by one.

5.1.4 Statistical analysis of results

In this section we present the statistical analysis of the model to verify the accuracy of the model and the simulated parameters. The simulated parameters of the model are the sample mean and variance of the radii distribution. We calculate the expected value for variance of the sample mean and use central limit theorem to calculate an approximation

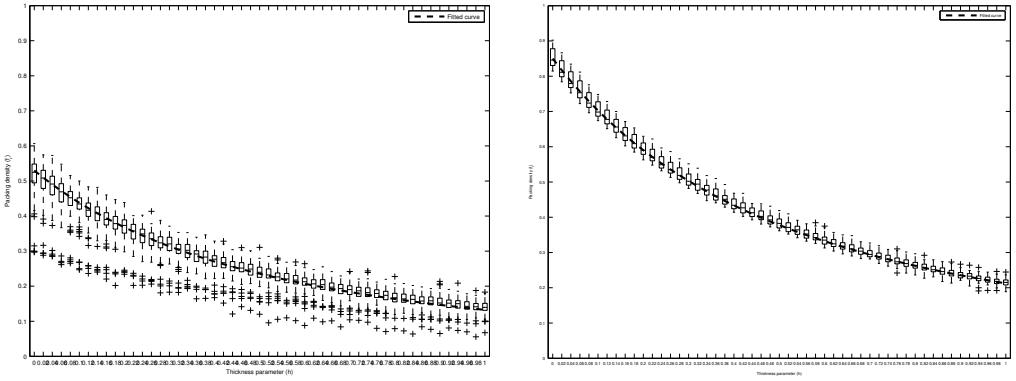

(a) (b)

Figure 5.6: The relationship between packing density and thickness parameter. (a) Dynamic approach (b) Constructive approach

of the sampling distribution. Therefore, the normal distribution will be utilised to find the probabilistic bounds for the estimation error and find the confidence intervals for the estimated values.
We consider the estimated mean as:

$$\bar{r} = \frac{1}{n} \sum_{i=1}^{n} r_i \tag{5.9}$$

We can consider $\bar{r}$ as an estimation of actual radius mean (μ). The sampling distribution of $\bar{r}$ determines how accurately $\bar{r}$ estimates μ. Using central limit theorem, the sampling distribution of the estimated mean can be modelled by a normal distribution. It can be stated that the more tightly the sampling distribution of $\bar{r}$ is centred around μ, the better the estimate.

The variance of the estimated mean, neglecting the finite population correction, is:

$$\text{var}(\bar{r}) = \frac{1}{n^2} \sum_{i=1}^{n} \text{var}(r_i) = \frac{\sigma^2}{n} \tag{5.10}$$

in which σ^2 is the actual variance of the population and n is the number of axons in the sample [160]. The standard deviation of $\bar{r}$ which is called standard error is:

$$\sigma_{\bar{r}} = \frac{\sigma}{\sqrt{n}} \tag{5.11}$$

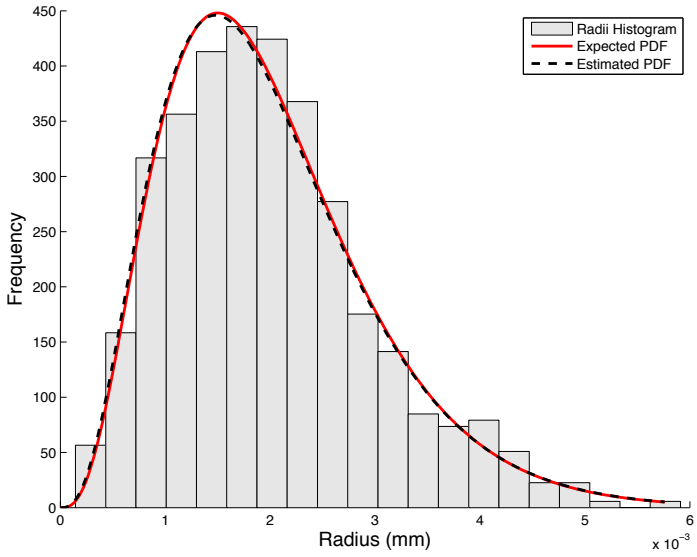

Figure 5.7: Constructive axon packing radii distribution histogram along with the expected and estimated PDF curves with $W = 100\,\mu m$, $f_r = 0.6$, $k = 4$ and $\theta = 5 \times 10^{-4}$.

In the case that we do not know the exact value for the population variance, we can estimate the population variance by the sample variance [160], given by

$$s^2 = \frac{1}{n}\sum_{i=1}^{n}(r_i - \bar{r})^2 \tag{5.12}$$

The standard error can be calculated as:

$$s_{\bar{r}} = \frac{s}{\sqrt{n}} \tag{5.13}$$

Eq. (5.11) and Eq. (5.13), show that the standard error has the inverse relation with the sample number. Therefore, for the models with more axons, the accuracy of the estimation would be better.

According to central limit theorem for a fixed number z,

$$P\left(\frac{\bar{r} - \mu}{\sigma_{\bar{r}}} \leq z\right) \to \Phi(z) \tag{5.14}$$

Therefore,we can derive a confidence interval for the population mean (μ). A confidence interval for a population parameter μ is a random interval, calculated from the sample

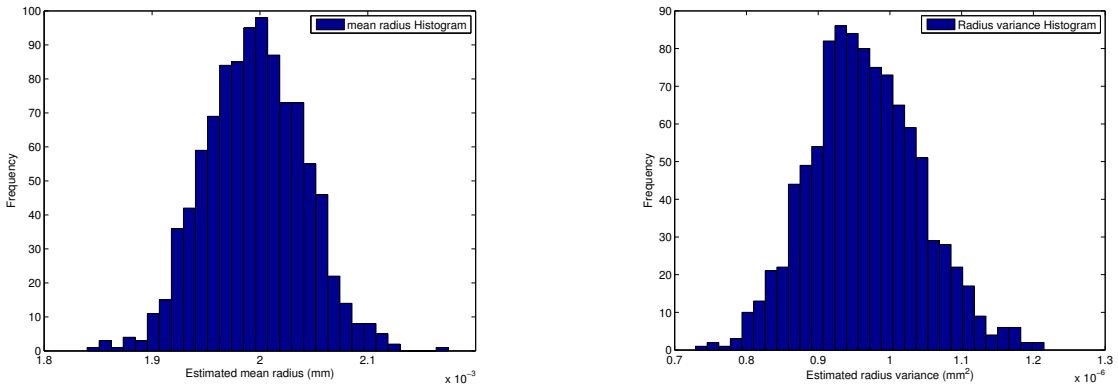

(a) (b)

Figure 5.8: (a) Estimated axon radii mean, (b) Estimated axon radii variance

which contains μ with a certain probability. Therefore, a confidence interval for μ can be calculated as:

$$P\left(\bar{r} - z(\alpha/2)\sigma_{\bar{r}} \leq \mu \leq \bar{r} + z(\alpha/2)\sigma_{\bar{r}}\right) \approx 1 - \alpha \tag{5.15}$$

Where $z(\alpha)$ is a number such that the area under the standard normal density function to the right of $z(\alpha)$ is α [160]. The standard error vs. packing density for both techniques is depicted in Figure 5.9 for comparison. Comparing the standard error for dynamic approach with the standard error for constructive approach, it can be inferred that the constructive approach leads to smaller standard error and consequently a more accurate simulation of the model parameters.

To summarise, it can be stated that the dynamic algorithm is easy to implement and less complicated in comparison with constructive algorithm. However, the simulation time required is relatively high especially for the models with high packing density and leads to lower computational efficiency, and higher standard error rate. The constructive approach is more efficient and produces more accurate results. Hence, we utilise this method in modelling the axons in a nerve bundle.

5.2 Random walk simulation of the diffusion of water particles in the brain white matter

In order to simulate the resultant NMR signal, the Brownian motion and diffusion of water molecules in biological tissue is modelled during the application of Stejskal-Tanner pulse

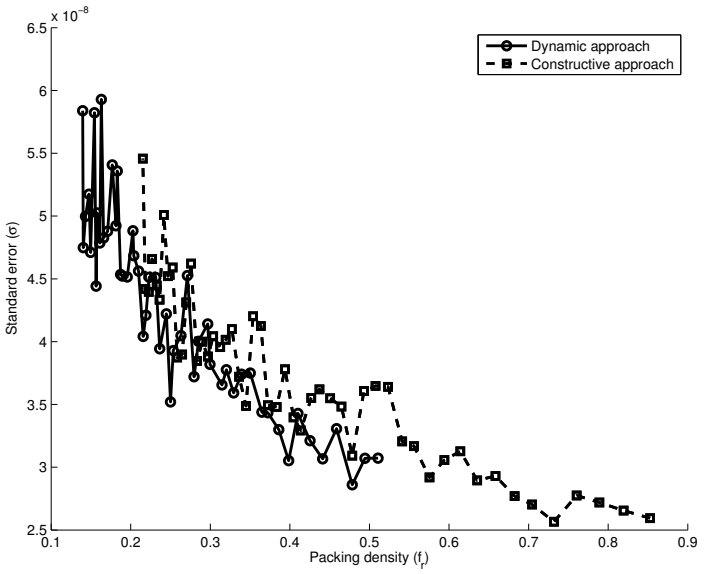

Figure 5.9: Standard error vs. Packing density. The more axons the lower the error.

sequence.

The accumulated phase offset of a single particle at time t after the RF excitation pulse can be calculated as:

$$\phi(\mathbf{r}, t) = 2\pi\gamma \int_0^t \vec{G}(t') \cdot \mathbf{r}(t')\, dt' \tag{5.16}$$

where $\mathbf{r}(t)$ [m] is the trajectory of a single particle during time t [s] under gradient pulse waveform $G(t)$ [T.m^{-1}], and γ [Hz.T^{-1}] is the gyromagnetic ratio.

Based on the measurement setup, during the first gradient pulse, spins acquire phase shifts proportional to the displacements of the molecules in the direction of the gradient. The second gradient pulse applied after a 180° RF refocusing pulse, shifts the phase of particles back proportional to their displacements during the second pulse [66, 85]. If a particle does not move between two pulses, the diffusion time (Δ), the phase shifts during the first and second pulses will cancel out each other completely and the spins become completely refocused at echo time. However, if particles move during the diffusion time, there will be a remaining phase offset related to the displacements during this period. In order to find the analytical description of this phase offset, we consider a single particle starting at time ($t_0 = 0$) in ($\mathbf{r}_0 = \mathbf{0}$). We assume without loss of generality that at $t = t_0$ the gradient field G is zero. The motion of water molecules during diffusion follows a Brownian motion [161] and can be modelled by a random walk process at small time steps

Δt. At each time step, the new position of the particle would be the sum of its initial position and a random Gaussian increment:

$$\mathbf{r}_k = \mathbf{r}_{k-1} + \mathbf{w}_k \tag{5.17}$$

where $\mathbf{w}_k \sim \mathcal{N}(\mathbf{0}, \sigma^2 \mathbf{I_n})$, i.i.d and the variance of the movements is calculated from Eq. (2.13) as $\sigma^2 = 2n\, D_0 \Delta t$. D_0 is the intrinsic diffusivity of the particles in an unrestricted medium. Substituting $\mathbf{r}_k$ and considering $\mathbf{r}_0 = \mathbf{0}$, without loss of generality the position at time t_k could be written as:

$$\mathbf{r}_k = \mathbf{w}_1 + \mathbf{w}_2 + ... + \mathbf{w}_k \tag{5.18}$$

Since only the phase difference is important, we consider the phase of the particles at $t = 0$ to be $\phi_0 = 0$. Each particle accumulates phase on each time step Δt:

$$\phi_k = \phi_{k-1} + 2\pi\gamma \vec{G} \cdot \mathbf{r}_k \Delta t \tag{5.19}$$

Here γ is the gyromagnetic ratio in [Hz.T^{-1}]. Substituting Eq. (5.18) into Eq. (5.19) the phase offset at the k-th time step is:

$$\begin{aligned}
\phi_k &= \phi_{k-1} + 2\pi\gamma \vec{G} \cdot [\mathbf{w}_1 + \mathbf{w}_2 + ... + \mathbf{w}_k]\, \Delta t \\
&= \phi_{k-2} + 2\pi\gamma \vec{G} \cdot \left[\sum_{i=1}^{k-1} \mathbf{w}_i \Delta t\right] + 2\pi\gamma \vec{G} \cdot \left[\sum_{i=1}^{k} \mathbf{w}_i \Delta t\right] \\
&= ... \\
&= 2\pi\gamma \vec{G} \cdot \left[\sum_{i=1}^{k} \sum_{j=1}^{i} \mathbf{w}_j \Delta t\right]
\end{aligned} \tag{5.20}$$

At the end of the first gradient pulse ($t = \delta$) the phase of each particle can be written as:

$$\phi_M = 2\pi\gamma \vec{G} \cdot \left[\sum_{i=1}^{M} (M - i + 1)\, \mathbf{w}_i \Delta t\right] \tag{5.21}$$

where $M = \lfloor \frac{\delta}{\Delta t} \rfloor$ is the largest integer such that $M \leq \frac{\delta}{\Delta t}$. During the period $\delta < t < \Delta$, the gradient pulse is zero and the phase offset is fixed. During this period a 180° RF pulse is applied which inverts all the phases:

$$\phi_N = -\phi_M \tag{5.22}$$

Here, $N = \lfloor \frac{\Delta}{\Delta t} \rfloor$ is the largest integer such that $N \leq \frac{\Delta}{\Delta t}$. During the period $\Delta < t < \Delta + \delta$, the second gradient is applied:

$$\begin{aligned}
\phi_{N+1} &= \phi_N + 2\pi\gamma \vec{G} \cdot [\mathbf{w}_1 + \mathbf{w}_2 + ... + \mathbf{w}_{N+1}]\, \Delta t \\
&= -\phi_M + 2\pi\gamma \vec{G} \cdot [\mathbf{w}_1 + \mathbf{w}_2 + ... + \mathbf{w}_{N+1}]\, \Delta t
\end{aligned} \tag{5.23}$$

and at the end of sequence $t = \Delta + \delta$ the final phase is:

$$\begin{aligned}\phi_K &= -\phi_M + 2\pi\gamma\vec{G}\cdot\left[\sum_{i=1}^{N} M\mathbf{w}_i\Delta t\right] + 2\pi\gamma\vec{G}\cdot\left[\sum_{i=1}^{M}\sum_{j=1}^{i}\mathbf{w}_{N+j}\Delta t\right] \\ &= -\phi_M + 2\pi\gamma\vec{G}\cdot\left[\sum_{i=1}^{N} M\mathbf{w}_i\Delta t\right] + 2\pi\gamma\vec{G}\cdot\left[\sum_{i=1}^{M}(M-i+1)\mathbf{w}_{N+i}\Delta t\right] \end{aligned} \tag{5.24}$$

Here $K = \lfloor\frac{\Delta+\delta}{\Delta t}\rfloor$ is the largest integer such that $K \leq \frac{\Delta+\delta}{\Delta t}$. Substituting Eq. (5.21) into Eq. (5.24) we have

$$\begin{aligned}\phi_K &= 2\pi\gamma\vec{G}\cdot\left[-\sum_{i=1}^{M}(M-i+1)\,\mathbf{w}_i\Delta t + \sum_{i=1}^{N} M\mathbf{w}_i\Delta t + \sum_{i=1}^{M}(M-i+1)\,\mathbf{w}_{N+i}\Delta t\right] \\ &= 2\pi\gamma\vec{G}\cdot\left[\sum_{i=0}^{M-1} i\,\mathbf{w}_{i+1}\Delta t - \sum_{i=M}^{N} M\mathbf{w}_i\Delta t - \sum_{i=1}^{M}(M-i+1)\,\mathbf{w}_{N+i}\Delta t\right] \end{aligned} \tag{5.25}$$

Since $\mathbf{w}_k \sim \mathcal{N}(\mathbf{0}, \sigma^2\mathbf{I})$ and $\sigma^2 = 2nD_0\Delta t$

$$\phi_K \sim N\left(0, 4\pi^2\gamma^2|\vec{G}|^2\sigma^2\left(\sum_{i=1}^{M} i^2\Delta t^2 + \sum_{i=M+1}^{N} M^2 i\Delta t^2 + \sum_{i=1}^{M} i^2\Delta t^2\right)\right) \tag{5.26}$$

Therefore, the phase variance of a single particle can be written as:

$$\sigma_\phi^2 = 8n\pi^2\gamma^2|\vec{G}|^2 D_0\left(\sum_{i=1}^{M} i^2\Delta t^3 + \sum_{i=M+1}^{N} M^2\Delta t^3 + \sum_{i=1}^{M} i^2\Delta t^3\right) \tag{5.27}$$

Considering the limit when $\Delta t \to 0$ the phase variance can be written in the continuous form as:

$$\sigma_\phi^2 = 8n\pi^2\gamma^2|\vec{G}|^2 D_0\left(\int_0^\delta t^2 dt + \delta^2\int_\delta^\Delta dt + \int_0^\delta t^2 dt\right) \tag{5.28}$$

which results in

$$\sigma_\phi^2 = 8n\pi^2 q^2(\Delta - \frac{\delta}{3})D_0 \tag{5.29}$$

where n is the spatial dimension (n=1, 2 or 3) and $q = |\mathbf{q}|$ [m^{-1}] is the reciprocal wave-number determined using a set of measurement parameters using Eq. (2.45).

For the case of having a single gradient direction, $n = 1$, and the phase variance is:

$$\sigma_\phi^2 = 8\pi^2 q^2(\Delta - \frac{\delta}{3})D_0 \tag{5.30}$$

Therefore, the particle will have certain amount of accumulated phase offset at time t which is related to the trajectory of the particle and the gradient pulse waveform.

The net diffusion attenuated DWMR signal in a particular voxel is calculated by averaging the signals from individual molecules over all initial positions and possible trajectories.

$$S = S_0 \int_{-\infty}^{\infty} P(\phi) \exp(-j\phi) d\phi \tag{5.31}$$

Here, $P(\phi)$ is the probability density functions for the phases in (2.43) and S_0 is the MR signal measured without using diffusion encoding gradients. Equation (5.31) indicates the effect of accumulated diffusion related phase offset of particles on the MR signal decay during a particular diffusion encoding gradient waveform $G(t)$.

As it is shown earlier, in the case of unrestricted Brownian motion of water particles (Gaussian distribution for the random movements), the accumulated phase of water particles can be modelled by a Gaussian distribution

$$P(\phi) = \frac{1}{\sqrt{2\pi\sigma_\phi^2}} \exp\left(-\frac{\phi^2}{2\sigma_\phi^2}\right) \tag{5.32}$$

in which the variance of accumulated phases is calculated using Eq. (5.29). Therefore, the resultant MR signal can be modelled as:

$$S(q) = S_0 \exp\left(-4\pi^2 q^2 D(\Delta - \frac{\delta}{3})\right) \tag{5.33}$$

which agrees with the results derived from solving Bloch-Torrey equations as given in Eq.(2.46). Therefore, the distribution of phase offset at the end of pulse sequence can be used to calculate the resultant NMR signal decay.

In order to simulate the DWMR signal decay, we utilised a two-dimensional simulation of 1,024,000 random walkers within a two-compartment tissue structure developed in the previous section. The simulations were performed using Message Passing Interface (MPI) parallel programming paradigm with 256 CPUs on an IBM BlueGene/Q supercomputer hosted at Victorian Life Sciences Computation Initiative (VLSCI). For each simulation, particles were initially spread randomly inside a voxel of 100 [μm] $\times$ 100 [μm]. The underlying tissue structure simulated using constructive approach described earlier with different values of the mean axon radius (R) and volume fraction (f). The values presented for axon radius in Table 5.1 was used as the true values for mean axon radii. The true values for volume fraction (f) was chosen as

0.22 0.24 0.27 0.31 0.35 0.40 0.46 0.53 0.62 0.74 0.90

The trajectories of the particles at each time step were calculated by moving the particles according to Eq. (5.17). The diffusivity of particles inside the tissue is set to 2×10^{-9}

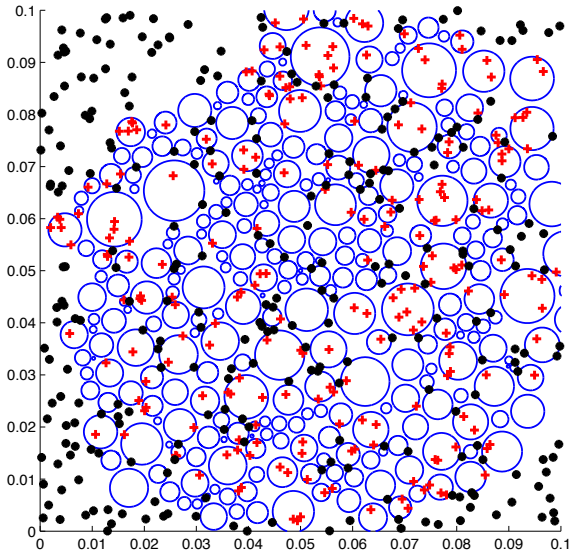

Figure 5.10: Simulation of diffusion of water particles in the biological tissue. Particles demonstrated with red + and black • are intracellular and extracellular respectively.

$[m^2s^{-1}]$. A sample visualisation of tracking the Brownian motion of water particles inside a simulated biological tissue is demonstrated in Figure 5.10.

The permeability of axon boundaries is considered zero i.e. there is not any transfer of particles between intracellular space and extracellular space and the amount of intracellular and extracellular particles are constant during the simulation. Particles hitting the boundaries of axons, were elastically reflected and the reflection of particles was continued until no more reflection was required. However, the surface relaxation (Υ) of axon boundaries was set to zero and the total random distance was constant during the reflection. Particles leaving the examined voxel were re-entered the voxel from the opposite side.

Table 5.1: Values of acquisition (top) and tissue related (bottom) parameters used for simulations

Parameter	[unit]	Min. value	Max. value	Number of steps
G_{max}	[mT/m]	986	986	1
N	-	20	20	1
Δ	[ms]	20	100	5
δ	[ms]	5	5	1
f	-	0.22	0.9	11
R	[μm]	1	10	10

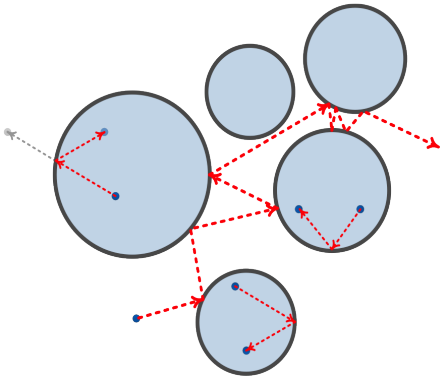

Figure 5.11: Modelling the Brownian motion of water particles in the brain white matter

Figure 5.11 depicts a simple illustration of 2D simulation of Brownian motion of water particles using a random walk process.

Given the assumptions above, the simulations were designed to model the Brownian motion of the water molecules in a two-compartment environment.

5.3 Validation of the DWMR signal attenuation models

The random walk simulations of the Brownian motion of particles were performed as described in the previous section and the resultant DWMR signal decays were calculated. The noise-free simulations were run for different combination of the acquisition and tissue related parameters as given in Table 5.1. In order to verify the validity of the models, the models were fitted to the noise-free simulated DWMR signals using a Levenberg-Marquardt algorithm. The fittings were performed using the multiple-Δ approach, in which the data from all different diffusion times were used simultaneously during the fitting process. The fitting process were performed 1000 times with random starting points for the algorithm in each run. In order to avoid results outside the acceptable ranges, the limits for the fitting algorithm were set with respect to the range of the tissue related parameters given in Table 5.1. However, we extended the limits slightly in order to capture estimated parameters close to the acceptable regions. Here, we only investigated the models which provide estimations of the mean axon radius (R) and volume fraction (f) as these are the only characteristic features of the simulated tissue that we can control during simulation. Therefore, the models used for validation are CHARMED, AxCaliber, MMWMD and Generalised 1D.

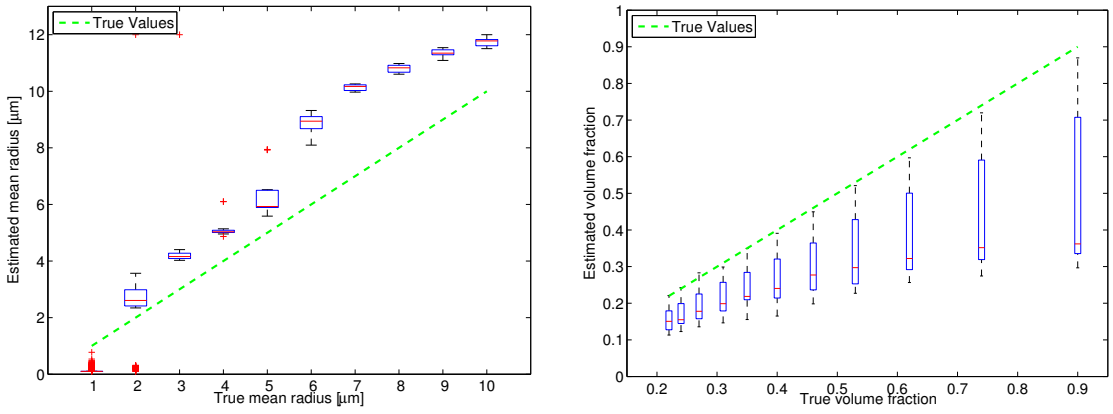

(a) (b)

Figure 5.12: Validation of the CHARMED model. (a) Results for mean axon radius (R), (b) Results for volume fraction (f)

5.3.1 Results for CHARMED model

The results of the fitting the noise-free simulation data to CHARMED model [105] is presented in Figure 5.12. In order to investigate the effect of a random starting point for the Levenberg-Marquardt algorithm on the derived estimations, the results are presented in separate box plots for mean axon radius R and volume fraction f with respect to their true values. the box plots provide us with a better understanding of the statistical presentation of the estimated parameters resulted from different starting points.

As it can be inferred from the results the CHARMED model fails to produce accurate estimations of the mean axon radius (R) and volume fraction (f). However, the model can follow the increasing trend in the data and the estimations provided by the model increase as the mean axon radius increases. The model overestimate the mean axon radius. Sensitivity of the estimated values to the starting points are relatively high for this model. This is much worse for the estimations of volume fraction, where the sensitivity increases by the increment in the true volume fraction. The model underestimate the values for volume fractions and the uncertainty of the estimations increases as the true volume fraction increases.

5.3.2 Results for AxCaliber model

The results of the fitting the noise-free simulation data to AxCaliber model [99] is presented in Figure 5.13. As it can be inferred from the results, AxCaliber model underestimates the

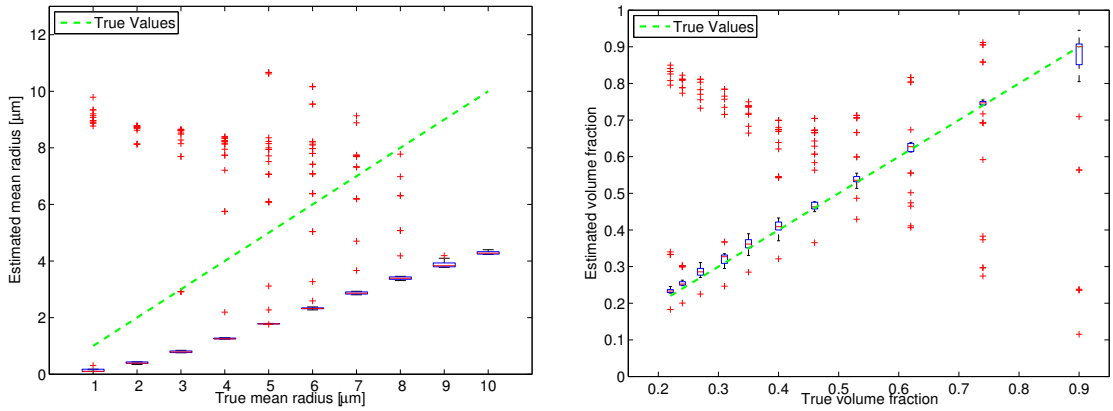

(a) (b)

Figure 5.13: Validation of the AxCaliber model. (a) Results for mean axon radius (R), (b) Results for volume fraction (f)

values for mean axon radius (R). The error (difference between true and estimated value) in the estimation of mean axon radius increases as the true values increase. On the other hand, the model provides a relatively accurate estimations of the volume fraction (f). The uncertainties related to the selection of the starting points for the fitting algorithm is relatively low for this model.

5.3.3 Results for MMWMD model

The results of the fitting the noise-free simulation data to MMWMD model [106] is presented in Figure 5.14. The results show that MMWMD model underestimates the values for the mean axon radius (R). The error (difference between true and estimated value) increases as the true mean axon radius increases.

The results for estimating volume fraction (f) reveals that the model slightly overestimate the true volume fraction. The uncertainty related to the choice of starting points increases as the true value increases. However, the estimations are relatively accurate and follow the trend in the real values.

The results for estimating using MMWMD is very similar to the results obtained from AxCaliber. However, the uncertainties due to the selection of starting points are higher in MMWMD in comparison with AxCaliber. This can be seen by more number of outliers and larger uncertainty regions in the box plots.

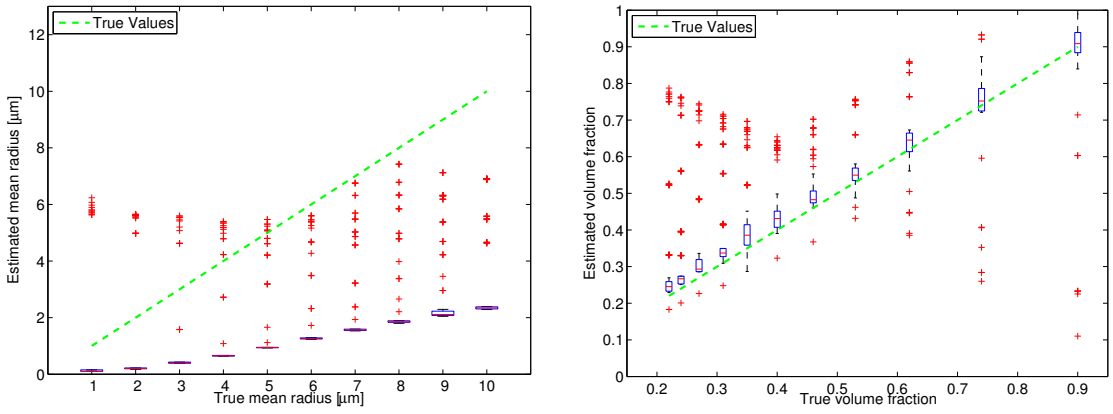

(a) (b)

Figure 5.14: Validation of the MMWMD model. (a) Results for mean axon radius (R), (b) Results for volume fraction (f)

5.3.4 Results for Generalised 1D model

The results of the fitting the noise-free simulation data to Generalised 1D model [104] is presented in Figure 5.15. The results show that the model fails to provide accurate estimations of the mean axon radius (R) and volume fraction (f). The estimations are highly sensitive to the selection of the starting point and the estimated values cover the whole acceptable region set during the fitting process. Hence, the model is not accurate and is not applicable in practice.

5.4 Summary

In this chapter, we presented a simulation framework to model the axon packings in the nerve bundles and to model the Brownain motion of water molecules and capture resultant DWMR signal decays.

We presented two different approaches for placement of the axons in the nerve bundles (Dynamic and Constructive approaches). We demonstrated that the constructive approach provides an efficient and accurate algorithm to model the placement of the axons within the nerve bundles.

In the next step, we presented an algorithm to simulate the Brownian motion of water molecule within the tissue models produced in the previous step. We utilised a random walk process to model the Brownian motion of water molecules. The mathematical

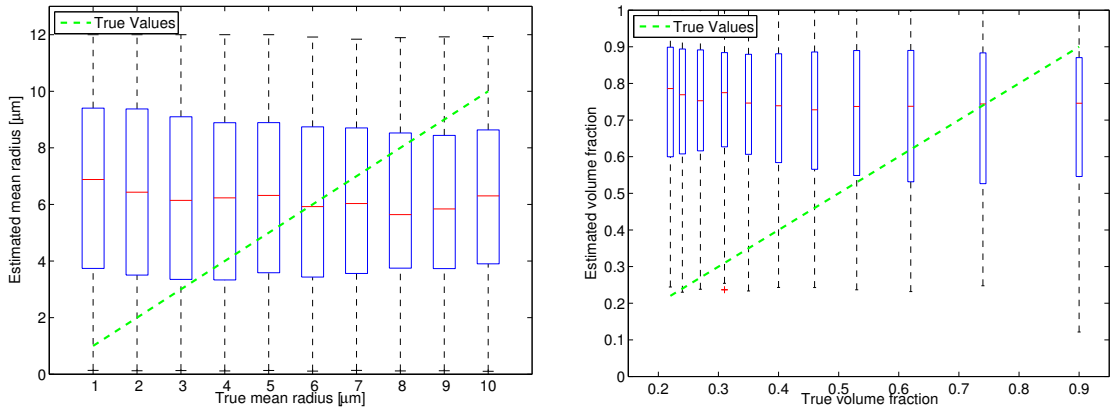

(a) (b)

Figure 5.15: Validation of the Generalised 1D model. (a) Results for mean axon radius (R), (b) Results for volume fraction (f)

calculations of the phase offsets of the particles undergoing DWMR measurements were presented. We used the phase information to construct the simulated DWMR signal. The simulations were implemented using MPI parallel programming paradigm on a Blue Gene supercomputer and the resultant DWMR signals were recorded. The datasets provided by this simulation framework were used later to analyse the accuracy of the models, by fitting to the simulated data using a Levenberg-Marquardt algorithm. In order to investigate the sensitivity of the estimations to the starting points in the fitting algorithm, the fitting process was repeated 1000 times with random starting points for each run.

The results demonstrated that none of the models were able to provide accurate estimations of the simulated tissue parameters. The more complex models like AxCaliber could provide a better estimations of the volume fraction and had lower sensitivity to the selection of starting points, while the simpler models like CHARMED and Generalised 1D failed to produce an accurate estimations of the tissue parameters and were highly sensitive to the choice of starting points in the fitting algorithm.

Comparing the results presented in this chapter, with the results in the previous chapter, we can conclude that more complex models can provide better noise-free estimations of the tissue-related parameters but have higher noise-related minimum uncertainty levels and lower performance, while simpler models perform better in terms of noise-related uncertainty levels but fail to present the tissue-related parameters accurately even in the noise-free situation. However, these results are not surprising and were predictable.

Conclusion

Diffusion Weighted Magnetic Resonance Imaging has the capability to reveal useful information about the microstructure of the central nervous system, through the measurement of diffusion of water in the biological tissue [1, 13, 93, 97].

There have been a number of techniques developed to derive geometric information from DWMR measurements. Most of the methods employ a model-based approach to relate DWMR signal decay to microstructure characteristics [13, 84, 88, 96, 99, 105, 106, 119, 162–164].

We presented an analysis of different models in terms of their assumptions and approximations used to derive them and noted the advantages and drawbacks of different models. The performance of the methods depend on both the quality of the proposed model and the experimental measurement setup e.g. SNR, number of measurements, gradient field strength, etc.

The quality of the model is broadly determined by how well the model can describe reality (bias error) and how sensitive the model parameters are to the measurements (variance error). Here, we ignored the bias error, hence we assumed that the models are "perfect" and indeed in our work we have used the models to generate the data (in this sense the models are perfect). Our focus has been to elucidate the variance error. To this end, we computed the CRLB for the model parameters (given a certain SNR). The CRLB is a simple function of the model itself.

Under a number of reasonable assumptions for the measurement setup, and the number of data points collected, we computed typical (normalised) error (variance) for estimated model parameters. We conclude that at present no single model is suitable for parameter estimation under presently feasible experimental conditions.

We demonstrated that in order to increase the performance of the models, the measurement setup should be improved in a way to increase the SNR, and increase the gradient field strength, which would not be possible using current scanners. On the other hand in-

creasing the SNR would require more number of measurements and longer scanning times and higher costs, which limits the applications of this methods in clinical scanners.

At the end, we presented a simulation framework to model the axon packings in nerve bundles. We utilised the resultant axon packing and modelled the Brownian motion of water particles and the resultant simulated datasets. The simulated data were used to investigate the validity of the models by fitting the models to the simulated data. The results indicated that none of the models were able to provide accurate estimations and the estimated parameters were extremely dependent on the fitting algorithm and the choice of starting points for the iterative fitting algorithm.

The results also showed that the more complex models can provide better estimations of the tissue-related parameters in noise-free conditions but have higher noise-related minimum uncertainty levels and perform poorly in noisy conditions, while simpler models perform better in terms of noise-related uncertainty levels but fail to present the tissue related parameters accurately even in noise-free conditions. Overcoming the challenge of complexity/performance of the models is the main problem facing the researchers in the field.

A future work might be to study the performance of the models under the real experimental setup and using empirical data. However, the performance of the models will be worse than what we presented here, as our results were based on the mathematical analysis under the best possible scenarios for each model.

Bibliography

[1] William S. Price. NMR Studies of Translational Motion: Principles and Applications. Cambridge University Press, 2009.

[2] Zhi-Pei Liang and Paul C. Lauterbur. Principles of magnetic resonance imaging: a signal processing perspective. SPIE Optical Engineering Press, 2000.

[3] S Cluskey and D B Ramsden. Mechanisms of neurodegeneration in amyotrophic lateral sclerosis. Mol Pathol, 54(6):386–392, December 2001.

[4] T Heads, M Pollock, A Robertson, W H Sutherland, and S Allpress. Sensory nerve pathology in amyotrophic lateral sclerosis. Acta Neuropathol, 82(4):316–320, 1991.

[5] J Piven, J Bailey, B J Ranson, and S Arndt. An mri study of the corpus callosum in autism. Am J Psychiatry, 154(8):1051–1056, August 1997.

[6] Masafumi Ihara, Tuomo M Polvikoski, Ros Hall, Janet Y Slade, Robert H Perry, Arthur E Oakley, Elisabet Englund, John T O'Brien, Paul G Ince, and Raj N Kalaria. Quantification of myelin loss in frontal lobe white matter in vascular dementia, alzheimer's disease, and dementia with lewy bodies. Acta Neuropathol, 119(5):579–589, May 2010.

[7] Anila B Syed, Richard A Armstrong, and Christopher U M Smith. A quantitative analysis of optic nerve axons in elderly control subjects and patients with alzheimer's disease. Folia Neuropathol, 43(1):1–7, 2005.

[8] G C DeLuca, G C Ebers, and M M Esiri. Axonal loss in multiple sclerosis: a pathological survey of the corticospinal and sensory tracts. Brain : a journal of neurology, 127(Pt 5):1009–18, May 2004.

[9] Qizhu Wu, Helmut Butzkueven, Melissa Gresle, Frank Kirchhoff, Anna Friedhuber, Qing Yang, Hong Wang, Ke Fang, Hao Lei, Gary F Egan, and Trevor J Kilpatrick. Mr diffusion changes correlate with ultra-structurally defined axonal degeneration in murine optic nerve. NeuroImage, 37(4):1138–47, October 2007.

[10] JM M Ritchie. On the relation between fibre diameter and conduction velocity in myelinated nerve fibres. Proceedings of the Royal Society of London, 217(1206):29–35, December 1982.

[11] S G Waxman. Determinants of conduction velocity in myelinated nerve fibers. Muscle Nerve, 3(2):141–150, 1980.

[12] Richard B. Buxton. Introduction to Functional Magnetic Resonance Imaging: Principles and Techniques. Cambridge University Press, 2009.

[13] Daniel C Alexander, Penny L Hubbard, Matt G Hall, Elizabeth A Moore, Maurice Ptito, Geoff J M Parker, and Tim B Dyrby. Orientationally invariant indices of axon diameter and density from diffusion mri. Neuroimage, 52(4):1374–1389, October 2010.

[14] Maximilian F. Reiser, Wolfhard Semmler, and Hedvig Hricak, editors. Magnetic Resonance Tomography. Springer Berlin Heidelberg, Berlin, Heidelberg, 2008.

[15] John Crank. The Mathematics of Diffusion. Oxford University Press, 1979.

[16] Liqiu Wang, Xuesheng Zhou, and Xiaohao Wei. Heat Conduction: Mathematical Models and Analytical Solutions. Springer Science & Business Media, 2007.

[17] Anatoliy Goldman. Mass Transport & Reactive Barriers in Packaging: Theory, Applications, & Design. DEStech Publications, Inc, 2008.

[18] Adolf Fick. Ueber diffusion. Annalen der Physik und Chemie, 170(1):59–86, 1855.

[19] Jean-Baptiste-Joseph Fourier. Theorie analytique de la chaleur. F. Didot, Paris, 1822.

[20] E. L. Cussler. Diffusion: Mass Transfer in Fluid Systems. Cambridge University Press, 1997.

[21] Bruce E. Poling, John M. Prausnitz, and John O' Connell. The Properties of Gases and Liquids, volume 6. McGraw Hill Professional, 2000.

[22] Ken A. Dill and Sarina Bromberg. Molecular Driving Forces: Statistical Thermodynamics in Chemistry and Biology. Garland Science, 2003.

[23] Albert Einstein. Investigations on the Theory of the Brownian Movement. Courier Dover Publications, 1956.

[24] Thomas M. de Swiet and Partha P. Mitra. Possible systematic errors in single-shot measurements of the trace of the diffusion tensor. Journal of Magnetic Resonance, Series B, 111(1):15–22, 1996.

[25] Robert Brown. Xxvii. a brief account of microscopical observations made in the months of june, july and august 1827, on the particles contained in the pollen of plants; and on the general existence of active molecules in organic and inorganic bodies. Philosophical Magazine Series 2, 4(21):161–173, September 1828.

[26] A. Einstein. Über die von der molekularkinetischen theorie der wärme geforderte bewegung von in ruhenden flüssigkeiten suspendierten teilchen. Annalen der Physik, 322(8):549–560, 1905.

[27] Horatio Scott Carslaw and J. John Conrad Jaeger. CONDUCTION OF HEAT IN SOLIDS. 2nde edition, Edition anglaise. Clarendo Press, 1986.

[28] Pabitra N. Sen. Time-dependent diffusion coefficient as a probe of geometry. Concepts in Magnetic Resonance, 23A(1):1–21, September 2004.

[29] PT T Callaghan. Pulsed-gradient spin-echo nmr for planar, cylindrical, and spherical pores under conditions of wall relaxation. Journal of Magnetic Resonance, Series A, 113(1):53–59, 1995.

[30] George B. Arfken, Hans J. Weber, and Frank E. Harris. Mathematical Methods for Physicists, Sixth Edition: A Comprehensive Guide. Academic Press, 2005.

[31] G. F. Roach. Green's Functions. Cambridge University Press, 1982.

[32] M. Necati Ozisik. Boundary Value Problems of Heat Conduction. Courier Dover Publications, 2002.

[33] G. Barton. Elements of Green's Functions and Propagation: Potentials, Diffusion, and Waves [Reprint] (Oxford Science Publications). Oxford University Press, USA, 1989.

[34] Dean G. Duffy. Green's Functions with Applications. Chapman and Hall/CRC, 2001.

[35] Dean G. Duffy. Advanced Engineering Mathematics with MATLAB, Third Edition. CRC Press, 2010.

[36] David Bergman, Keh-Jim Dunn, Lawrence Schwartz, and Partha Mitra. Self-diffusion in a periodic porous medium: A comparison of different approaches. Physical Review E, 51(4):3393–3400, April 1995.

[37] Kosma Szutkowski, Jacek Klinowski, and Stefan Jurga. Nmr studies of restricted diffusion in lyotropic systems. Solid state nuclear magnetic resonance, 22(2-3):394–408, January 2002.

[38] Partha P. Mitra and Pabitra N. Sen. Effects of surface relaxation on nmr pulsed field gradient experiments in porous media. Physica A: Statistical Mechanics and its Applications, 186(1):109–114, 1992.

[39] Partha Mitra, Pabitra Sen, Lawrence Schwartz, and Pierre Le Doussal. Diffusion propagator as a probe of the structure of porous media. Physical Review Letters, 68(24):3555–3558, June 1992.

[40] Partha Mitra and Pabitra Sen. Effects of microgeometry and surface relaxation on nmr pulsed-field-gradient experiments: Simple pore geometries. Physical Review B, 45(1):143–156, January 1992.

[41] Partha P. Mitra, Pabitra N. Sen, and Lawrence M. Schwartz. Short-time behavior of the diffusion coefficient as a geometrical probe of porous media. Physical Review B, 47(14):8565–8574, April 1993.

[42] L.L. Latour, P.P. Mitra, R.L. Kleinberg, and C.H. Sotak. Time-dependent diffusion coefficient of fluids in porous media as a probe of surface-to-volume ratio. Journal of Magnetic Resonance, Series A, 101(3):342–346, February 1993.

[43] Pabitra N. Sen. Time-dependent diffusion coefficient as a probe of the permeability of the pore wall. The Journal of Chemical Physics, 119(18):9871, October 2003.

[44] A Szafer, J Zhong, and J C Gore. Theoretical model for water diffusion in tissues. Magnetic Resonance in Medicine, 33(5):697–712, May 1995.

[45] Els Fieremans. Validation methods for diffusion weighted magnetic resonance imaging in brain white matter. PhD thesis, Ghent University, 2008.

[46] Joseph Klafter and J. M. Drake. Molecular dynamics in restricted geometries. Wiley, 1989.

[47] Rustem Valiullin and Vladimir Skirda. Time dependent self-diffusion coefficient of molecules in porous media. The Journal of Chemical Physics, 114(1):452, January 2001.

[48] Jacob Bear. Dynamics of Fluids in Porous Media (Dover Civil and Mechanical Engineering). Dover Publications, 1988.

[49] Matthieu Adam-Berret, Marine Boulard, Alain Riaublanc, and François Marie-ette. Evolution of fat crystal network microstructure followed by nmr. Journal of agricultural and food chemistry, 59(5):1767–73, March 2011.

[50] F. A.L. Dullien. Porous Media, Second Edition: Fluid Transport and Pore Structure. Academic Press, 1991.

[51] L.L. Latour, R.L. Kleinberg, P.P. Mitra, and C.H. Sotak. Pore-size distributions and tortuosity in heterogeneous porous media. Journal of Magnetic Resonance, Series A, 112(1):83–91, 1995.

[52] Stefan R. Heil and Manfred Holz. Electrical transport in a disordered medium: Nmr measurement of diffusivity and electrical mobility of ionic charge carriers. Journal of Magnetic Resonance, 135(1):17–22, 1998.

[53] Uzi Hizi and David J. Bergman. Molecular diffusion in periodic porous media. Journal of Applied Physics, 87(4):1704, February 2000.

[54] Charles Nicholson. Diffusion and related transport mechanisms in brain tissue. Reports on Progress in Physics, 64(7):815, 2001.

[55] Jan Hrabe, Sabina Hrabe, Sabina Hrabetova, and Karel Segeth. A model of effective diffusion and tortuosity in the extracellular space of the brain. Biophys J, 87(3):1606–1617, September 2004.

[56] B. Jonsson, H. Wennerstrom, P. G. Nilsson, and P. Linse. Self-diffusion of small molecules in colloidal systems. Colloid & Polymer Science, 264(1):77–88, January 1986.

[57] Bruce Alberts, Alexander Johnson, Julian Lewis, Martin Raff, Keith Roberts, and Peter Walter. Molecular Biology of the Cell. Garland Science, 2007.

[58] Eva Sykova and Charles Nicholson. Diffusion in brain extracellular space. Physiol Rev, 88(4):1277–1340, October 2008.

[59] Wang Zhan, Li Jiang, Murray H Loew, and Yihong Yang. Mapping spatiotemporal diffusion inside the human brain using a numerical solution of the diffusion equation. Magnetic resonance imaging, 26(5):694–702, June 2008.

[60] Julia M. Edgar and Ian R. Griffiths. Chapter 5 - white matter structure: A microscopists view. In Diffusion MRI, pages 74–103. Elsevier, 2009.

[61] A S Lamantia and P Rakic. Cytological and quantitative characteristics of four cerebral commissures in the rhesus monkey. The Journal of comparative neurology, 291(4):520–37, January 1990.

[62] Els Fieremans, Yves Deene, Steven Delputte, Eric Achten, Yves D'Asseler, and Ignace Lemahieu. Simulation of the diffusion in the interstitial space of a fiber

phantom. In 2007 4th IEEE International Symposium on Biomedical Imaging: From Nano to Macro, pages 788–791. IEEE, 2007.

[63] E. Hahn. Spin echoes. Physical Review, 80(4):580–594, November 1950.

[64] H. Carr and E. Purcell. Effects of diffusion on free precession in nuclear magnetic resonance experiments. Physical Review, 94(3):630–638, May 1954.

[65] D. E. Woessner. Effects of diffusion in nuclear magnetic resonance spin-echo experiments. The Journal of Chemical Physics, 34(6):2057, August 1961.

[66] E. O. Stejskal and J. E. Tanner. Spin diffusion measurements: Spin echoes in the presence of a time-dependent field gradient. The Journal of Chemical Physics, 42(1):288–292, 1965.

[67] E. O. Stejskal. Use of spin echoes in a pulsed magnetic-field gradient to study anisotropic, restricted diffusion and flow. The Journal of Chemical Physics, 43(10):3597, May 1965.

[68] John Tanner. Use of a pulsed magnetic-field gradient for measurements of self-diffusion by spin-echo nuclear magnetic resonance with applications to restricted diffusion in several tissues and emulsions. Phd thesis, University of Wisconsin–Madison, 1966.

[69] J. E. Tanner and E. O. Stejskal. Restricted self-diffusion of protons in colloidal systems by the pulsed-gradient, spin-echo method. The Journal of Chemical Physics, 49(4):1768, September 1968.

[70] Charles Sidney Johnson and Don A. Gabriel. Laser Light Scattering. Courier Dover Publications, 1994.

[71] Peter F. Green. Kinetics, Transport, and Structure in Hard and Soft Materials. CRC Press, 2005.

[72] Buckley Crist. Polymer self-diffusion measurements by small-angle neutron scattering. Journal of Non-Crystalline Solids, 131-133:709–714, June 1991.

[73] Xin-Cun Tang, Xia-Wei Song, Pei-Zhi Shen, and Dian-Zeng Jia. Capacity intermittent titration technique (citt): A novel technique for determination of li+ solid diffusion coefficient of limn2o4. Electrochimica Acta, 50(28):5581–5587, 2005.

[74] Antonie J. W. G. Visser and Mark A. Hink. New perspectives of fluorescence correlation spectroscopy. Journal of Fluorescence, 9(1):81–87, March 1999.

[75] Kevin Braeckmans, Liesbeth Peeters, Niek N Sanders, Stefaan C De Smedt, and Joseph Demeester. Three-dimensional fluorescence recovery after photobleaching with the confocal scanning laser microscope. Biophysical journal, 85(4):2240–52, October 2003.

[76] S. B. Lyon, L. Philippe, and E. Tsuousoglou. Direct measurements of ionic diffusion in protective organic coatings, July 2013.

[77] Allen P. Minton. Analytical centrifugation with preparative ultracentrifuges. Analytical Biochemistry, 176(2):209–216, February 1989.

[78] Charles R. Cantor and Paul R. Schimmel. Biophysical Chemistry, Part 2: Techniques for the Study of Biological Structure and Function (Pt. 2). W. H. Freeman and Company, 1980.

[79] Vadim Kuperman. Magnetic Resonance Imaging: Physical Principles and Applications. Academic Press, 2000.

[80] H. Torrey. Bloch equations with diffusion terms. Physical Review, 104(3):563–565, November 1956.

[81] F. Bloch. Nuclear induction. Physical Review, 70(7-8):460–474, October 1946.

[82] Paul Heitjans and Jörg Kärger, editors. Diffusion in Condensed Matter. Springer-Verlag, Berlin/Heidelberg, 2005.

[83] L.Z. Wang, A. Caprihan, and Eiichi Fukushima. The narrow-pulse criterion for pulsed-gradient spin-echo diffusion measurements. Journal of Magnetic Resonance, Series A, 117(2):209–219, 1995.

[84] Dmitriy A Yablonskiy and Alexander L Sukstanskii. Theoretical models of the diffusion weighted mr signal. NMR in biomedicine, 23(7):661–681, August 2010.

[85] PT T Callaghan, A Coy, D MacGowan, K J Packer, and F O Zelaya. Diffraction-like effects in nmr diffusion studies of fluids in porous solids. Nature, 351(6326):467–469, 1991.

[86] Paul T. Callaghan. Principles of Nuclear Magnetic Resonance Microscopy. Oxford University Press, 1993.

[87] Baldwin Robertson. Spin-echo decay of spins diffusing in a bounded region. Physical Review, 151(1):273–277, November 1966.

[88] C. H. Neuman. Spin echo of spins diffusing in a bounded medium. The Journal of Chemical Physics, 60(11):4508, August 1974.

[89] William S. Price. Pulsedfield gradient nuclear magnetic resonance as a tool for studying translational diffusion: Part 1. basic theory. Concepts in Magnetic Resonance, 9(5):299–336, 1997.

[90] William S. Price. Pulsedfield gradient nuclear magnetic resonance as a tool for studying translational diffusion: Part ii. experimental aspects. Concepts in Magnetic Resonance, 10(4):197–237, 1998.

[91] P van Gelderen, D DesPres, P C van Zijl, C T Moonen, and P Vangelderen. Evaluation of restricted diffusion in cylinders. phosphocreatine in rabbit leg muscle. Journal of magnetic resonance, Series B, 103(3):255–260, March 1994.

[92] P. Linse and O. Soderman. The validity of the short-gradient-pulse approximation in nmr studies of restricted diffusion. simulations of molecules diffusing between planes, in cylinders and spheres. Journal of Magnetic Resonance, Series A, 116(1):77–86, September 1995.

[93] Els Fieremans, Jens H Jensen, and Joseph A Helpern. White matter characterization with diffusional kurtosis imaging. NeuroImage, 58(1):177–88, September 2011.

[94] Daniel Barazany, Peter J Basser, and Yaniv Assaf. In vivo measurement of axon diameter distribution in the corpus callosum of rat brain. Brain, 132(Pt 5):1210–1220, May 2009.

[95] Christian Beaulieu. Diffusion MRI. Elsevier, 2009.

[96] Denis Le Bihan. Looking into the functional architecture of the brain with diffusion mri. Nature reviews. Neuroscience, 4(6):469–80, June 2003.

[97] D G Cory, A N Garroway, and J B Miller. Applications of spin transport as a probe of local geometry. Polymer Preprints – Papers Presented At The Boston, Massachusetts Meeting -, 31(1):149–150, 1990.

[98] Derek K Jones. Challenges and limitations of quantifying brain connectivity in vivo with diffusion mri. Imaging in Medicine, 2(3):341–355, June 2010.

[99] Yaniv Assaf, Tamar Blumenfeld-Katzir, Yossi Yovel, and Peter J Basser. Axcaliber: a method for measuring axon diameter distribution from diffusion mri. Magnetic Resonance in Medicine, 59(6):1347–1354, June 2008.

[100] Yaniv Assaf and Peter J Basser. Composite hindered and restricted model of diffusion (charmed) mr imaging of the human brain. NeuroImage, 27(1):48–58, August 2005.

[101] G J Stanisz, A Szafer, G a Wright, and R M Henkelman. An analytical model of restricted diffusion in bovine optic nerve. Magnetic Resonance in Medicine, 37(1):103–11, January 1997.

[102] Sune N Jespersen, Christopher D Kroenke, Leif Ostergaard, Joseph J H Ackerman, Dmitriy a Yablonskiy, and Leif Ø stergaard. Modeling dendrite density from magnetic resonance diffusion measurements. Neuroimage, 34(4):1473–1486, February 2007.

[103] L A Johnston, D Wright, R H H M Philipsen, S C Kolbe, J A Bourne, Iven Mareels, and Gary Egan. Inferring micron-scale tissue structure using extreme value theory for cylindrically-restricted diffusion. In 19th Annual Meeting of International Society for Magnetic Resonance in Medicine (ISMRM), Montreal, Canada, May 2011.

[104] Leigh A Johnston, David Wright, and Iven M Mareels. Exploiting non-gaussian phase distributions to model micron-scale restricted diffusion. In 20th Annual Meeting of International Society for Magnetic Resonance in Medicine (ISMRM), Melbourne, Australia, May 2012.

[105] Yaniv Assaf, Raisa Z Freidlin, Gustavo K Rohde, and Peter J Basser. New modeling and experimental framework to characterize hindered and restricted water diffusion in brain white matter. Magnetic Resonance in Medicine, 52(5):965–78, November 2004.

[106] Daniel C Alexander. A general framework for experiment design in diffusion mri and its application in measuring direct tissue-microstructure features. Magnetic Resonance in Medicine, 60(2):439–448, August 2008.

[107] Hui Zhang, Tim B Dyrby, and Daniel C Alexander. Axon diameter mapping in crossing fibers with diffusion mri. Med Image Comput Comput Assist Interv, 14(Pt 2):82–89, 2011.

[108] Hui Zhang, Torben Schneider, Claudia A Wheeler-Kingshott, and Daniel C Alexander. Noddi: practical in vivo neurite orientation dispersion and density imaging of the human brain. Neuroimage, 61(4):1000–1016, July 2012.

[109] D Le Bihan, E Breton, D Lallemand, P Grenier, E Cabanis, and M Laval-Jeantet. Mr imaging of intravoxel incoherent motions: application to diffusion and perfusion in neurologic disorders. Radiology, 161(2):401–7, November 1986.

[110] M E Moseley, Y Cohen, J Mintorovitch, L Chileuitt, H Shimizu, J Kucharczyk, M F Wendland, and P R Weinstein. Early detection of regional cerebral ischemia in cats:

comparison of diffusion- and t2-weighted mri and spectroscopy. Magnetic Resonance in Medicine, 14(2):330–346, May 1990.

[111] A L Sukstanskii, J J H Ackerman, and D A Yablonskiy. Effects of barrier-induced nuclear spin magnetization inhomogeneities on diffusion-attenuated mr signal. Magnetic Resonance in Medicine, 50(4):735–742, October 2003.

[112] Karsten Tabelow, Jörg Polzehl, Vladimir Spokoiny, and Henning U Voss. Diffusion tensor imaging: structural adaptive smoothing. NeuroImage, 39(4):1763–73, February 2008.

[113] P J Basser, J Mattiello, and D LeBihan. Estimation of the effective self-diffusion tensor from the nmr spin echo. Journal of magnetic resonance. Series B, 103(3):247–54, March 1994.

[114] Derek K Jones. The effect of gradient sampling schemes on measures derived from diffusion tensor mri: a monte carlo study. Magnetic resonance in medicine : official journal of the Society of Magnetic Resonance in Medicine / Society of Magnetic Resonance in Medicine, 51(4):807–15, April 2004.

[115] Derek K Jones and Peter J Basser. "squashing peanuts and smashing pumpkins": how noise distorts diffusion-weighted mr data. Magnetic resonance in medicine : official journal of the Society of Magnetic Resonance in Medicine / Society of Magnetic Resonance in Medicine, 52(5):979–93, November 2004.

[116] Miriam Helen Anna Bauer, Sebastiano Barbieri, Jan Klein, Jan Egger, Daniela Kuhnt, Bernd Freisleben, Horst Karl Hahn, and Christopher Nimsky. Boundary estimation of fiber bundles derived from diffusion tensor images. International journal of computer assisted radiology and surgery, 6(1):1–11, January 2011.

[117] Liya Wang, Felicia C Goldstein, Allan I Levey, James J Lah, Carolyn C Meltzer, Chad A Holder, and Hui Mao. White matter hyperintensities and changes in white matter integrity in patients with alzheimer's disease. Neuroradiology, 53(5):373–81, May 2011.

[118] Denis Le Bihan. Molecular diffusion, tissue microdynamics and microstructure. NMR in Biomedicine, 8(7):375–386, November 1995.

[119] T Niendorf, R M Dijkhuizen, D G Norris, M van Lookeren Campagne, and K Nicolay. Biexponential diffusion attenuation in various states of brain tissue: implications for diffusion-weighted imaging. Magnetic Resonance in Medicine, 36(6):847–857, December 1996.

[120] Y Assaf and Y Cohen. Non-mono-exponential attenuation of water and n-acetyl aspartate signals due to diffusion in brain tissue. Journal of Magnetic Resonance, 131(1):69–85, March 1998.

[121] Y Assaf and Y Cohen. In vivo and in vitro bi-exponential diffusion of n-acetyl aspartate (naa) in rat brain: a potential structural probe? NMR in biomedicine, 11(2):67–74, April 1998.

[122] Y Assaf and Y Cohen. Structural information in neuronal tissue as revealed by q-space diffusion nmr spectroscopy of metabolites in bovine optic nerve. NMR in biomedicine, 12(6):335–44, October 1999.

[123] D L Buckley, J D Bui, M I Phillips, T Zelles, B A Inglis, H D Plant, and S J Blackband. The effect of ouabain on water diffusion in the rat hippocampal slice measured by high resolution nmr imaging. Magnetic Resonance in Medicine, 41(1):137–142, January 1999.

[124] Chih-Liang Chin, Felix W Wehrli, Scott N Hwang, Masaya Takahashi, and David B Hackney. Biexponential diffusion attenuation in the rat spinal cord: computer simulations based on anatomic images of axonal architecture. Magnetic Resonance in Medicine, 47(3):455–460, March 2002.

[125] C A Clark and D Le Bihan. Water diffusion compartmentation and anisotropy at high b values in the human brain. Magnetic Resonance in Medicine, 44(6):852–859, December 2000.

[126] B A Inglis, E L Bossart, D L Buckley, E D 3rd Wirth, and T H Mareci. Visualization of neural tissue water compartments using biexponential diffusion tensor mri. Magnetic Resonance in Medicine, 45(4):580–587, April 2001.

[127] Y Ke, B M Cohen, S Lowen, F Hirashima, L Nassar, and P F Renshaw. Biexponential transverse relaxation (t(2)) of the proton mrs creatine resonance in human brain. Magnetic Resonance in Medicine, 47(2):232–238, February 2002.

[128] R V Mulkern, S Vajapeyam, R L Robertson, P A Caruso, M J Rivkin, and S E Maier. Biexponential apparent diffusion coefficient parametrization in adult vs newborn brain. Magnetic resonance imaging, 19(5):659–668, June 2001.

[129] R V Mulkern, H P Zengingonul, R L Robertson, P Bogner, K H Zou, H Gudbjartsson, C R Guttmann, D Holtzman, W Kyriakos, F a Jolesz, and S E Maier. Multi-component apparent diffusion coefficients in human brain: relationship to spin-lattice relaxation. Magnetic Resonance in Medicine, 44(2):292–300, August 2000.

[130] J Pfeuffer, S W Provencher, and R Gruetter. Water diffusion in rat brain in vivo as detected at very large b values is multicompartmental. MAGMA, 8(2):98–108, May 1999.

[131] T Yoshiura, O Wu, A Zaheer, T G Reese, and A G Sorensen. Highly diffusion-sensitized mri of brain: dissociation of gray and white matter. Magnetic Resonance in Medicine, 45(5):734–740, May 2001.

[132] Els Fieremans, Yves De Deene, and Ignace Lemahieu. Validation of models for the diffusion weighted mr signal in brain white matter. In 2008 5th IEEE International Symposium on Biomedical Imaging: From Nano to Macro, pages 915–918. IEEE, May 2008.

[133] Dmitriy a Yablonskiy, G Larry Bretthorst, and Joseph J H Ackerman. Statistical model for diffusion attenuated mr signal. Magnetic Resonance in Medicine, 50(4):664–669, October 2003.

[134] Els Fieremans, Yves De Deene, Steven Delputte, Mahir S Ozdemir, Yves D'Asseler, Jelle Vlassenbroeck, Karel Deblaere, Eric Achten, and Ignace Lemahieu. Simulation and experimental verification of the diffusion in an anisotropic fiber phantom. Journal of magnetic resonance (San Diego, Calif. : 1997), 190(2):189–99, February 2008.

[135] Jimmy Lätt, Markus Nilsson, Ronnie Wirestam, Edvin Johansson, Elna-Marie Larsson, Freddy Stahlberg, and Sara Brockstedt. In vivo visualization of displacement-distribution-derived parameters in q-space imaging. Magnetic resonance imaging, 26(1):77–87, January 2008.

[136] Jens H Jensen, Joseph A Helpern, Anita Ramani, Hanzhang Lu, and Kyle Kaczynski. Diffusional kurtosis imaging: the quantification of non-gaussian water diffusion by means of magnetic resonance imaging. Magnetic Resonance in Medicine, 53(6):1432–1440, June 2005.

[137] Astrid F. Frø hlich, Leif Ø stergaard, and Valerij G. Kiselev. Effect of impermeable boundaries on diffusion-attenuated mr signal. Journal of Magnetic Resonance, 179(2):223–233, 2006.

[138] David Laidlaw and Joachim Weickert, editors. Visualization and Processing of Tensor Fields. Mathematics and Visualization. Springer Berlin Heidelberg, Berlin, Heidelberg, 2009.

[139] Jaime E Cisternas. Can axcaliber be extended to estimate axonal radius and orientation at the same time? 18th Annual Meeting of International Society for Magnetic Resonance in Medicine (ISMRM), 2010.

[140] DS Tuch, RM Weisskoff, JW Belliveau, and VJ Wedeen. High angular resolution diffusion imaging of the human brain. In 7th Annual Meeting of International Society for Magnetic Resonance in Medicine (ISMRM), Philadelphia, 1999.

[141] D K Jones, M A Horsfield, and A Simmons. Optimal strategies for measuring diffusion in anisotropic systems by magnetic resonance imaging. Magnetic resonance in medicine : official journal of the Society of Magnetic Resonance in Medicine / Society of Magnetic Resonance in Medicine, 42(3):515–25, September 1999.

[142] David S Tuch, Timothy G Reese, Mette R Wiegell, Nikos Makris, John W Belliveau, and Van J Wedeen. High angular resolution diffusion imaging reveals intravoxel white matter fiber heterogeneity. Magnetic resonance in medicine : official journal of the Society of Magnetic Resonance in Medicine / Society of Magnetic Resonance in Medicine, 48(4):577–82, October 2002.

[143] Ivana Drobnjak and Daniel C Alexander. Optimising time-varying gradient orientation for microstructure sensitivity in diffusion-weighted mr. Journal of magnetic resonance (San Diego, Calif. : 1997), 212(2):344–54, October 2011.

[144] Sl Codd, Pt Callaghan, Codd, and Callaghan. Spin echo analysis of restricted diffusion under generalized gradient waveforms: Planar, cylindrical, and spherical pores with wall relaxivity. Journal of Magnetic Resonance, 137(2):358–372, April 1999.

[145] Daniel Alexander, Yaniv Assaf, Daniel Barazany, Tim Dyrby, Henrik Lundell, and Hui Zhang. A comparative study of axon diameter imaging techniques using diffusion mri. In International Society for Magnetic Resonance in Medicine, editor, 19th Annual Meeting of International Society for Magnetic Resonance in Medicine (ISMRM), Montreal, Canada, 2011.

[146] Daniel C. Alexander. Axon radius measurements in vivo from diffusion mri: a feasibility study. In 2007 IEEE 11th International Conference on Computer Vision, pages 1–8. Ieee, 2007.

[147] Tim B Dyrby, Lise V Sø gaard, Matt G Hall, Maurice Ptito, and Daniel C Alexander. Contrast and stability of the axon diameter index from microstructure imaging with diffusion mri. Magnetic resonance in medicine : official journal of the Society of Magnetic Resonance in Medicine / Society of Magnetic Resonance in Medicine, September 2012.

[148] J. S. Murday and R. M. Cotts. Self-diffusion coefficient of liquid lithium. The Journal of Chemical Physics, 48(11):4938, September 1968.

[149] P J Basser, J Mattiello, and D LeBihan. Mr diffusion tensor spectroscopy and imaging. Biophys J, 66(1):259–267, January 1994.

[150] Eleftheria Panagiotaki, Torben Schneider, Bernard Siow, Matt G Hall, Mark F Lythgoe, and Daniel C Alexander. Compartment models of the diffusion mr signal in brain white matter: a taxonomy and comparison. NeuroImage, 59(3):2241–54, February 2012.

[151] Peter J Basser and Carlo Pierpaoli. Microstructural and physiological features of tissues elucidated by quantitative-diffusion-tensor mri. Journal of Magnetic Resonance, 111(2):209–219, December 1996.

[152] Marco Catani, Robert J. Howard, Sinisa Pajevic, and Derek K. Jones. Virtual in vivo interactive dissection of white matter fasciculi in the human brain. Neuroimage, 17(1):77–94, September 2002.

[153] T E Conturo, N F Lori, T S Cull, E Akbudak, A Z Snyder, J S Shimony, R C McKinstry, H Burton, and M E Raichle. Tracking neuronal fiber pathways in the living human brain. Proc Natl Acad Sci U S A, 96(18):10422–10427, August 1999.

[154] Christopher H Sotak. The role of diffusion tensor imaging in the evaluation of ischemic brain injury - a review. NMR in biomedicine, 15(7-8):561–9, 2002.

[155] Steven M. Kay. Fundamentals of Statistical Signal Processing: Estimation Theory, Volume 1. Prentice-Hall PTR, 1998.

[156] HáKon Gudbjartsson and Samuel Patz. The rician distribution of noisy mri data. Magnetic Resonance in Medicine, 34(6):910–914, December 1995.

[157] C. Radhakrishna Rao and J. Wishart. Minimum variance and the estimation of several parameters. Mathematical Proceedings of the Cambridge Philosophical Society, 43(02):280, October 1947.

[158] Azeddine Benabbou, Houman Borouchaki, Patrick Laug, and Jian Lu. Sphere packing and applications to granular structure modeling. Proceedings of the 17th International Meshing Roundtable, pages 1–18, 2008.

[159] Charles R Collins and Kenneth Stephenson. A circle packing algorithm. Computational Geometry, 25(3):233–256, 2003.

[160] John A. Rice. Mathematical Statistics and Data Analysis. Cengage Learning, 2001.

[161] A. Einstein. Zur elektrodynamik bewegter körper. Annalen der Physik, 322(10):891–921, 1905.

[162] Thoralf Niendorf, David G. Norris, and Dieter Leibfritz. Detection of apparent restricted diffusion in healthy rat brain at short diffusion times. Magnetic Resonance in Medicine, 32(5):672–677, November 1994.

[163] Alexander L Sukstanskii and Dmitriy A Yablonskiy. Effects of restricted diffusion on mr signal formation. Journal of Magnetic Resonance, 157(1):92–105, July 2002.

[164] A.L. Sukstanskii, D.A. Yablonskiy, and J.J.H. Ackerman. Effects of permeable boundaries on the diffusion-attenuated mr signal: insights from a one-dimensional model. Journal of Magnetic Resonance, 170(1):56–66, 2004.

[165] E. Purcell, H. Torrey, and R. Pound. Resonance absorption by nuclear magnetic moments in a solid. Physical Review, 69(1-2):37–38, January 1946.

[166] F. Bloch, W. Hansen, and M. Packard. The nuclear induction experiment. Physical Review, 70(7-8):474–485, October 1946.

Appendices

A Principles of Magnetic Resonance Imaging

Since a good understanding of the fundamentals of NMR and MRI is crucial for a better understanding of the DWMR techniques presented in this work, here we present a brief review on basic physical principles of MRI. This appendix is mainly adopted from the textbook by Liang et al. [2]. More complete descriptions can be found in the literature [2, 79, 86].

A.1 Nuclear Magnetic Resonance phenomenon

MRI is based on the NMR phenomenon discovered independently by Bloch and Purcell in 1946 [81,165,166]. NMR is due to the interaction between nuclei with a non-zero magnetic moment and an external oscillating magnetic field [2, 79]. A fundamental property of the nuclei having odd atomic mass number (number of protons and neutrons) e.g. nucleus of Hydrogen atom (^1H) is that they have intrinsic nuclear spin with angular moment $\vec{J}$. The magnitude of angular moment for spins is given by

$$J = \frac{\mathrm{h}}{2\pi}\sqrt{I(I+1)} \tag{A.1}$$

where, h is Planck's constant (6.63×10^{-34} [J.s]) and I is the nuclear spin quantum number which is an integer multiple of $\frac{1}{2}$ i.e.

$$I = 0,\ \frac{1}{2},\ 1,\ \frac{3}{2},\ 2,\ ... \tag{A.2}$$

For ^{1}H, ^{13}C, ^{19}F and ^{31}P nuclei, $I = \frac{1}{2}$ and such a spin system is called a spin-$\frac{1}{2}$ system [2]. A nucleus is NMR active if $I \neq 0$. Since the nucleus of atoms has electric charge (because of protons), like any spinning charged object, the spinning of nucleus around its own axis creates a magnetic moment $\vec{\mu}$ which can be modelled by:

Table A.1: NMR properties of some nuclei

Element	Spin quantum number (I)	Gyromagnetic ratio (γ) [MHz.T^{-1}]
^{1}H	1/2	42.576
^{13}C	1/2	10.705
^{19}F	1/2	40.053
^{23}Na	3/2	11.262
^{31}P	1/2	17.235

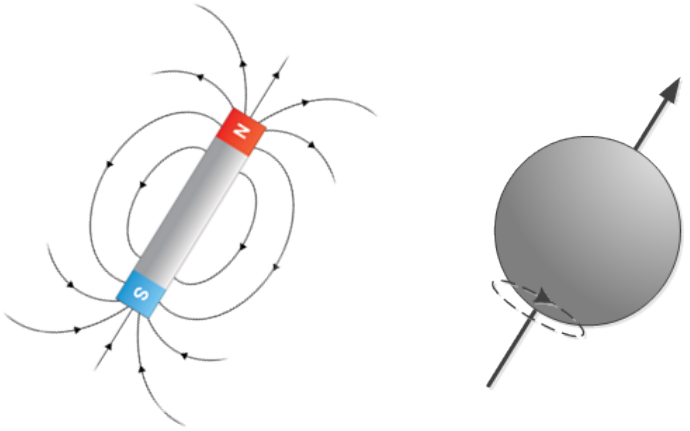

Figure A.1: Spinning nucleus will create magnetic moment.

$$\vec{\mu} = 2\pi\gamma\vec{J} \tag{A.3}$$

where γ [Hz.T^{-1}] is a nucleus dependent physical constant known as the gyromagnetic ratio [2, 79]. The values for gyromagnetic ratio for some important nuclei are presented in Table A.1. Figure A.1 depicts a simple visualisation of spinning nucleus and resulting magnetic moment.

Based on quantum mechanics and using Eq. (A.3) and Eq. (A.1), the magnitude of $\vec{\mu}$ can be calculated as

$$\mu = \gamma \mathrm{h}\sqrt{I(I+1)} \tag{A.4}$$

The magnetic moments for NMR active nuclei at thermal equilibrium (but not absolute zero) are in random directions and as a result, the net macroscopic magnetic field is zero. However, if a NMR active spin system is placed in an external magnetic field, B_0, the magnetic moments can have one of a discrete set of $(2I+1)$ orientations. For spin-$\frac{1}{2}$ system, $I = \frac{1}{2}$ and the magnetic moments can obtain one of the two possible orientations

as depicted in Figure 5.2(a). The torque that a magnetic moment experiences due to an external magnetic field without considering any interaction between different magnetic moments can be calculated using

$$\vec{\tau} = \vec{\mu} \times B_0 \vec{k} \tag{A.5}$$

where we considered the external magnetic field to be of magnitude B_0 and aligned with $\vec{k}$, a unit vector in z direction. The rate of change of angular momentum is equal to the torque being applied hence

$$\frac{d\vec{J}}{dt} = \vec{\mu} \times B_0 \vec{k} \tag{A.6}$$

Replacing Eq. (A.3) into Eq. (A.6), the equation for motion of magnetic moments in external magnetic field can be written as:

$$\frac{d\vec{\mu}}{dt} = 2\pi\gamma \vec{\mu} \times B_0 \vec{k} \tag{A.7}$$

where $\vec{\mu}$ can be defined in Cartesian coordinate system as

$$\vec{\mu} = \mu_x \vec{i} + \mu_y \vec{j} + \mu_z \vec{k} \tag{A.8}$$

Eq. (A.7) can be written in scalar form as

$$\begin{cases} \dfrac{d\mu_x}{dt} = 2\pi\gamma\, B_0\, \mu_y = \omega_0\, \mu_y \\ \dfrac{d\mu_y}{dt} = -2\pi\gamma\, B_0\, \mu_x = -\omega_0\, \mu_x \\ \dfrac{d\mu_z}{dt} = 0 \end{cases} \tag{A.9}$$

Taking second derivatives with respect to time from the first two equations we have

$$\begin{cases} \dfrac{d^2\mu_x}{dt^2} = -\omega_0^2\, \mu_x \\ \dfrac{d\mu_y}{dt} = -\omega_0^2\, \mu_y \end{cases} \tag{A.10}$$

which has solutions of the form

$$\begin{cases} \mu_x(t) = \mu_x(0)\cos(\omega_0 t) + \mu_y(0)\sin(\omega_0 t) \\ \mu_y(t) = -\mu_x(0)\sin(\omega_0 t) + \mu_y(0)\cos(\omega_0 t) \\ \mu_z(t) = \mu_z(0) \end{cases} \tag{A.11}$$

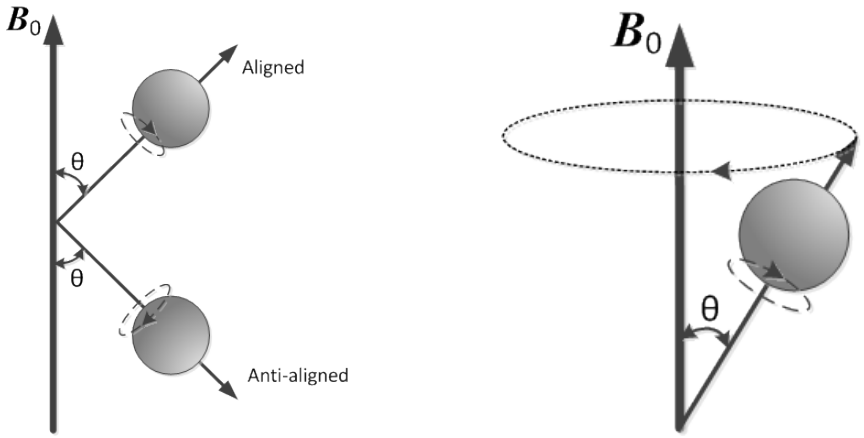

(a) (b)

Figure A.2: Spinning nucleus in external magnetic field (a) A spinning nucleus in spin-$\frac{1}{2}$ system can have one of the two positions when being placed in an external magnetic field B_0 (b) A spinning nucleus will start to precess around the axis parallel to B_0 filed.

Using the complex notation for the vectors in the transverse plane, the equation of motion of magnetic moment is described as

$$\begin{cases} \mu_{xy}(t) = \mu_{xy}(0)\exp(-\mathrm{j}\omega_0 t) \\ \mu_z(t) = \mu_z(0) \end{cases} \tag{A.12}$$

where $\mu_{xy}(t) = \mu_x(t) + \mathrm{j}\mu_y(t)$; $\mu_{xy}(0)$ and $\mu_z(0)$ are the initial values of magnetic moment the in transverse (perpendicular to the direction of the external magnetic field) and longitudinal (parallel with the direction of the external magnetic field) planes respectively and

$$\mu(0) = \sqrt{\mu_{xy}(0)^2 + \mu_z(0)^2} \tag{A.13}$$

Eq. (A.12) indicates that the magnetic moments placed in external magnetic field exhibit precession around the axis parallel to the external magnetic field as depicted in Figure 5.2(b). The angular frequency of nuclear precession is given by:

$$\omega_0 = 2\pi\gamma B_0 \tag{A.14}$$

which is the well-known Larmor frequency relation. In order to be able to analyse the macroscopic behaviour of the spin system, the bulk magnetisation vector $\vec{M}$ is introduced as the vector sum of all microscopic magnetic moments in the object being investigated and is described as:

$$\vec{M} = \sum_{n=1}^{N_s} \vec{\mu}_n \tag{A.15}$$

where $\vec{\mu}_n$ is the n-th microscopic magnetic moment and N_s is the total number of magnetic moments in the object. In the absence of external magnetic field $\vec{M} = 0$. As discussed before, for a spin-$\frac{1}{2}$ system and when placed in an external magnetic field, the magnetic moments will become either aligned or anti-aligned with the external field (Figure 5.2(a)). Spins in different directions have different energy. Based on the relations from quantum mechanics, the energy of the magnetic moments aligned with the magnetic field is calculated as:

$$E = -\vec{\mu} \cdot \vec{B}_0 = -\mu_z B_0 = -\frac{1}{2}\gamma \mathrm{h} B_0 \tag{A.16}$$

and for the moment in the reverse direction is

$$E = \frac{1}{2}\gamma \mathrm{h} B_0 \tag{A.17}$$

Hence, the energy difference between two states is

$$\Delta E = \gamma \mathrm{h} B_0 \tag{A.18}$$

which is known as the Zeeman splitting phenomenon. According to Boltzmann relationship, the ratio of the spins aligned and anti-aligned can be calculated as:

$$\frac{N_1}{N_2} = \exp\left(\frac{\Delta E}{\mathrm{k}T}\right) \tag{A.19}$$

where k is the Boltzmann's constant (1.38×10^{-23} [J.K^{-1}]), T is the temperature in [K] and N_1 and N_2 are the number of aligned and anti-aligned spins respectively. Considering $\Delta E << \mathrm{k}T$, and using first order approximation:

$$\frac{N_1}{N_2} \approx 1 + \frac{\gamma \mathrm{h} B_0}{\mathrm{k}T} \tag{A.20}$$

and

$$N_1 - N_2 \approx N_s \frac{\gamma \mathrm{h} B_0}{2\mathrm{k}T} \tag{A.21}$$

where $N_s = N_1 + N_2$ denotes the total number of spins.

Eq. (A.20) indicates that the number of spins in lower energy state are slightly more than the number of spin in higher energy state. This difference results in an observable bulk magnetisation vector $\vec{M}$ aligned with the external magnetic field. The magnitude of the magnetisation vector can be calculated using the following equation

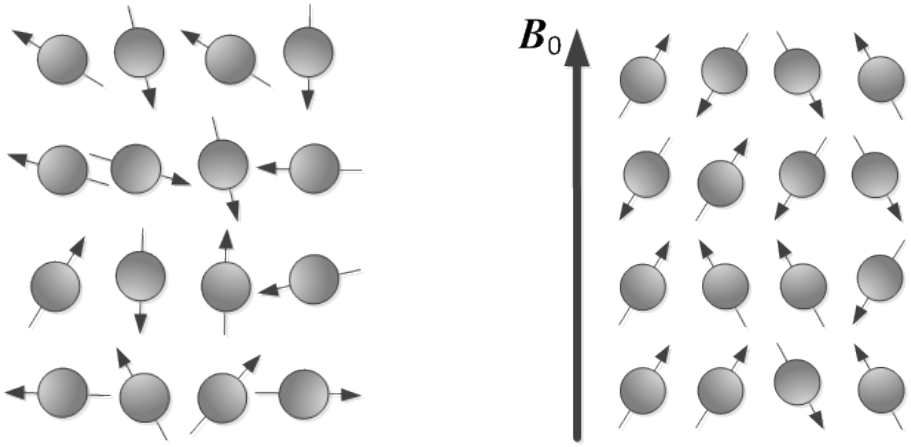

(a) (b)

Figure A.3: The effect of external magnetic field on magnetic moments (a) Without the external field, the magnetic moments are aligned randomly so the net magnetisation vector is zero. (b) Magnetic moments placed in an external magnetic field take one of the two aligned or anti-aligned states. However, the number of magnetic moments in aligned state is more so the net magnetisation vector will be aligned to the external magnetic field.

$$M_0 = |\vec{M}| = (N_1 - N_2)\,\frac{1}{2}\gamma\mathrm{h} = \frac{\gamma^2 \mathrm{h}^2 N_s B_0}{4\mathrm{k}T} \tag{A.22}$$

Eq. (A.22) depicts the linear dependence of the bulk magnetisation on the external magnetic field strength B_0 and the total number of spins N_s [2].

A.2 RF excitation

As discussed in the previous section, the magnetic moments placed in an external magnetic field start to precess around the external field. From a macroscopic point of view, we can describe an ensemble of a large number of spins with a bulk magnetisation vector $\vec{M}$ which is aligned with the external magnetic field. Although there exists a microscopic transverse component for each magnetic moment vector, the transverse component of the bulk magnetisation vector $\vec{M}$ is zero. This is due to the random distribution of phases for different magnetic moments as expressed in Eq. (A.12). The phases of the precessions in the transverse plane for an ensemble of magnetic moments are distributed uniformly in $[-\pi\,,\,\pi]$, as depicted in Figure A.4.

By applying a second oscillating magnetic field $\vec{B}_1(t)$ perpendicular to $\vec{B}_0$ and with the same frequency of the precession frequency of spins, it is possible to establish a coherence in the spin phases. This phenomenon is called resonance. Since the Larmor frequency of

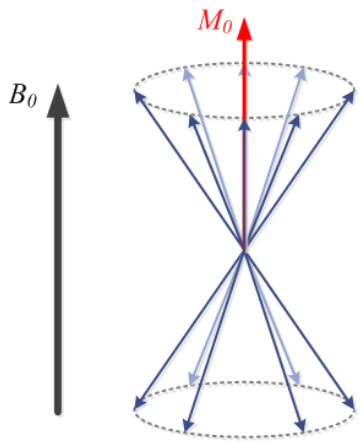

Figure A.4: Snapshot of an ensemble of magnetic moments placed in external magnetic field $\vec{B}_0$. The number of moments aligned with the external magnetic field is slightly more than the number of moments aligned in opposite direction and results a bulk magnetisation vector $\vec{M}$.

the spins are usually in the RF range, it is possible to generate the B_1 field using a RF pulse. For the ease of vector operations, we use complex notation to illustrate vectors in the transverse (xy) plane. A typical B_1 field using the complex notation takes the form:

$$\vec{B}_1(t) = B_1^e(t)\ \exp\left(-\mathrm{j}(2\pi\nu t + \phi)\right) \tag{A.23}$$

where $B_1^e(t)$ is the pulse envelope function, ν is the frequency of oscillations of B_1 field in [Hz] and ϕ is the phase offset in [rad]. j is the unit imaginary number where $\mathrm{j}^2 = -1$. The envelope function $B_1^e(t)$ determines the frequency selectivity of the RF pulse which will be explained later in this chapter. Figure A.5 depicts the RF pulses with two different envelope functions.

Based on Planck's law, an electromagnetic radiation with frequency ν carries the energy:

$$E = \mathrm{h}\nu \tag{A.24}$$

In order for a spin to transit from one energy state to another, the amount of energy it receives must be equal to the energy difference between the two energy states as described in Eq. (A.18). As a result,

$$\mathrm{h}\nu = \gamma \mathrm{h} B_0 = \frac{1}{2\pi}\mathrm{h}\omega_0 \tag{A.25}$$

Therefore, the angular frequency of the oscillations should be equal to the Larmor frequency of the spins, which is called the resonance condition:

$$\omega_{RF} = \omega_0 \tag{A.26}$$

where $\omega_{RF} = 2\pi\nu$ is the angular frequency of the oscillating RF magnetic field in [rad.s^{-1}].

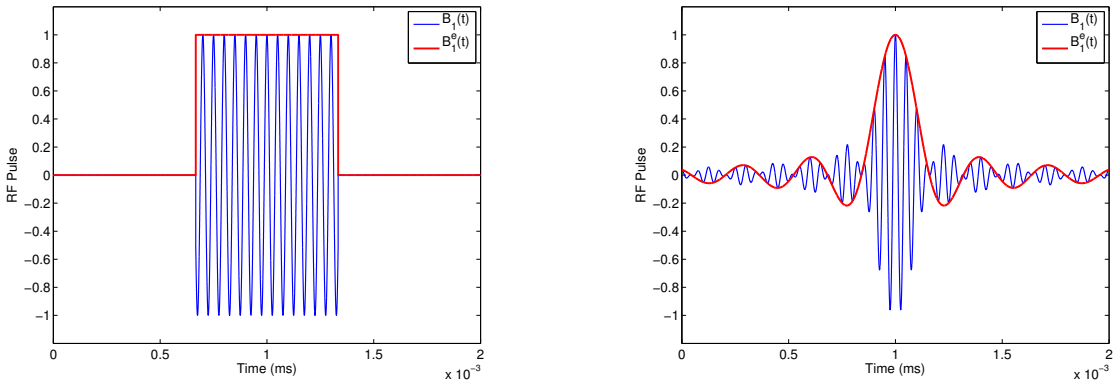

(a) (b)

Figure A.5: RF excitation pulses with (a) Rectangular and (b) Sinc envelope functions

In order to analyse the motion of the magnetic moments during the application of RF pulse, we use the rotating coordinate system, for which the transverse plane rotates clockwise with the angular frequency ω_0. For the rotating coordinate system, we use $\vec{i}'$, $\vec{j}'$ and $\vec{k}'$ to depict the unit vectors in rotating x', y' and z' directions [2]. The transformation of laboratory frame to rotating frame is given by:

$$\begin{cases} \vec{i}' = \cos(\omega_0 t)\vec{i} - \sin(\omega_0 t)\vec{j} \\ \vec{j}' = \sin(\omega_0 t)\vec{i} + \cos(\omega_0 t)\vec{j} \\ \vec{k}' = \vec{k} \end{cases} \tag{A.27}$$

We consider a simple case where the spin system consists of an ensemble of magnetic moments with identical Larmor frequency $\omega_0 = 2\pi\gamma B_0$. Without loss of generality, we assume that the initial phase offset (ϕ) of the oscillating magnetic field in Eq. (A.23) is zero. Therefore, the oscillating magnetic field in rotating coordinate system denoted by B_1', can be written as:

$$\vec{B_1'}(t) = B_1^e(t)\vec{i}' \tag{A.28}$$

Using the equation of motion for a single magnetic moment in Eq. (A.7), the equation of motion for bulk magnetisation vector $\vec{M}$, can be written as:

$$\frac{d\vec{M}}{dt} = 2\pi\gamma\, \vec{M} \times \vec{B} \tag{A.29}$$

which can be written in the rotating coordinate system as:

$$\frac{\partial \vec{M}'}{\partial t} = 2\pi\gamma\, \vec{M}' \times \vec{B}' - \vec{\omega}' \times \vec{M}' \tag{A.30}$$

$$= 2\pi\gamma\, \vec{M}' \times \left(\vec{B}' + \frac{\vec{\omega}'}{2\pi\gamma}\right) \tag{A.31}$$

$$= 2\pi\gamma\, \vec{M}' \times \vec{B}'_{eff} \tag{A.32}$$

where $\vec{M}'$ and $\vec{B}'$ are the bulk magnetisation and magnetic field vectors respectively. $\vec{\omega}'$ denotes the rotation of the coordinates and is defined as:

$$\vec{\omega}' = -\omega_0 \vec{k} \tag{A.33}$$

for a clockwise rotation. $\vec{B'_{eff}}$ is the effective magnetic field that the bulk magnetisation vector experiences in the rotating coordinate system [2]. In the case that the applied magnetic field to the spin system is only $\vec{B} = B_0\vec{k}$, the effective field is zero:

$$\vec{B'_{eff}} = \vec{B}' - \frac{2\pi\gamma B_0 \vec{k}'}{2\pi\gamma} = B_0\vec{k}' - B_0\vec{k}' = 0 \tag{A.34}$$

which confirms that the bulk magnetisation is aligned with the magnetic field and there is not any force to move it.

However, in the presence of the oscillating magnetic field, $\vec{B}_1(t)$, satisfying the resonance condition and using Eq. (A.28), the effective magnetic field is calculated as:

$$\vec{B}'_{eff} = \vec{B}' - \frac{2\pi\gamma B_0 \vec{k}'}{2\pi\gamma} = \left(B_0\vec{k}' + B_1^e(t)\vec{i}'\right) - B_0\vec{k}' = B_1^e(t)\vec{i}' \tag{A.35}$$

Therefore, the equation of motion for the bulk magnetisation vector is:

$$\frac{\partial \vec{M}'}{\partial t} = 2\pi\gamma\, \vec{M}' \times B_1^e(t)\vec{i}' \tag{A.36}$$

For a rectangular RF pulse envelope given by:

$$B_1^e(t) = B_1 \Pi\left(\frac{t - T_p/2}{T_p}\right) = \begin{cases} B_1 & 0 \le t \le T_p\,, \\ 0 & \text{otherwise}\,, \end{cases} \tag{A.37}$$

in which T_p is the pulse width in [s], and considering the initial conditions $M_{x'}(0) = M_{y'}(0) = 0$ and $M_{z'}(0) = M_0$, the solution of Eq. (A.36), can be written as

$$\begin{cases} M_{x'}(t) = 0 \\ M_{y'}(t) = M_0 \sin(\omega_1 t) \\ M_{z'}(t) = M_0 \cos(\omega_1 t) \end{cases} \tag{A.38}$$

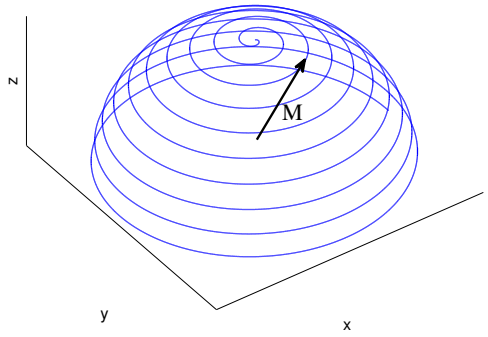

Figure A.6: The trajectory of magnetisation vector in response to a rectangular 90° RF pulse.

where $\omega_1 = 2\pi\gamma B_1$. This solution shows that the bulk magnetisation vector $\vec{M}'$ precesses around x' axis with angular frequency $\vec{\omega}_1 = -2\pi\gamma\vec{B}_1$. The flip angle α is defined as the angle between $\vec{M}$ and the z- axis can be calculated using:

$$\alpha = \int_0^{T_p} \omega_1(t)dt = \int_0^{T_p} 2\pi\gamma B_1^e(t)dt \tag{A.39}$$

For the case of rectangular pulse envelope, the flip angle is calculated as:

$$\alpha = \omega_1 T_p = 2\pi\gamma B_1 T_p \tag{A.40}$$

A pulse which causes the rotation of α° degree is called an α° pulse (like 90° pulse or 180° pulse). A simple visualisation of the tip of the magnetisation vector during a rectangular 90° excitation pulse is illustrated in Figure A.6.

The analysis presented above, was based on the case in which the resonance frequency for all spins is the same. In practice, because of field inhomogeneity and chemical shift effect, excitations are not on-resonance for all the magnetic moments. Therefore, the effective magnetic field in the case of off-resonance excitations and in the rotating frame can be calculated as:

$$\vec{B}'_{eff} = \left(B_0 - \frac{\nu}{\gamma}\right)\vec{k}' + B_1^e(t)\vec{i}' \tag{A.41}$$

Here ν is the frequency of RF pulse oscillations. This relationship indicates that, in the case of off-resonance excitations, the effective magnetic field has two components in the rotating coordinate system, a B_1 related component along the x'-axis and a residual $(B_0 - \nu/\gamma)$ component along the z'-axis. As a result, the transverse magnetisation vector

immediately after the RF pulse for the case of off-resonance excitation is no longer along the y' axis and has a phase shift ϕ_0 from y' axis toward x' axis.

The frequency selectivity of an RF pulse is determined using the Fourier transform of its envelope function and can be approximated as:

$$\frac{\alpha(\Delta\omega_0)}{\alpha(0)} \approx \frac{\mathcal{F}\{B_1^e(t)\}(\Delta\omega_0)}{\mathcal{F}\{B_1^e(t)\}(0)} \tag{A.42}$$

where $\Delta\omega_0 = \omega_0 - \omega_{RF}$, $\alpha(\Delta\omega_0)$ is the flip angle for a pulse with $\Delta\omega_0$ deviation from Larmor frequency and $\mathcal{F}\{B_1^e(t)\}(\omega)$ is the Fourier transform of the envelop function calculated as:

$$\mathcal{F}\{B_1^e(t)\}(\omega) = \int_{-\infty}^{\infty} B_1^e(t) \exp\left(-\mathrm{j}\omega t\right) dt \tag{A.43}$$

A.3 Spin relaxation and the Bloch equations

In the previous section, we described the process of excitation of the magnetic moments using an external oscillating magnetic field. However, quantum mechanics indicate that, the spins will return to their thermal equilibrium state after a certain time provided that the external force is removed. This process is called relaxation [2,79]. The recovery of the longitudinal magnetisation $\vec{M}_z$ is called longitudinal relaxation and the destruction of the transverse magnetisation M_{xy} is called transverse relaxation.

The complete time dependent behaviour of the motion of bulk magnetisation vector $\vec{M}$ is described using the Bloch equations [81].

$$\frac{d\vec{M}}{dt} = 2\pi\gamma\, \vec{M} \times \vec{B} - \frac{M_x\vec{i} + M_y\vec{j}}{T_2} - \frac{(M_z - M_0)\,\vec{k}}{T_1} \tag{A.44}$$

where $\vec{M}_0 = M_0\vec{k}$ is the longitudinal magnetisation vector at thermal equilibrium in the presence of $\vec{B}_0$ field only and can be calculated from Eq. (A.22). T_1 and T_2 are the time constants describing the relaxation in longitudinal and transverse planes, respectively [2, 79]. By transforming Eq. (A.44) into rotating frame coordinates and considering the case of on-resonance excitation, the Bloch equations in rotating coordinates are described as:

$$\begin{cases} \dfrac{dM_{z'}}{dt} = -\dfrac{M_{z'} - M_0}{T_1} \\ \dfrac{dM_{x'y'}}{dt} = -\dfrac{M_{x'y'}}{T2} \end{cases} \tag{A.45}$$

where $\vec{M}_{x'y'} = M_{x'}\vec{i}' + M_{y'}\vec{j}'$. The solutions of Eq. (A.45) are of the form:

$$\begin{cases} M_{x'y'}(t) = M_{x'y'}(0^+)\exp\left(-\dfrac{t}{T_2}\right) \\ M_{z'}(t) = M_0\left(1-\exp\left(-\dfrac{t}{T_1}\right)\right) + M_{z'}(0^+)\exp\left(-\dfrac{t}{T_1}\right) \end{cases} \tag{A.46}$$

where $M_{x'y'}(0^+)$ and $M_{z'}(0^+)$ are the magnetisation on transverse and longitudinal planes immediately after the RF pulse. These results show that the relaxation processes follow exponential functions. The values of T_1 and T_2 depend on tissue structure and its surroundings and for a given spin system T_1 is always longer than T_2.

The combined effect of free precession and relaxation can be shown in the laboratory coordinates and using the complex notation as

$$\begin{cases} M_{xy}(t) = M_{xy}(0^+)\exp\left(-\dfrac{t}{T_2}\right)\exp\left(-\mathrm{j}\omega_0 t\right) \\ M_z(t) = M_0\left(1-\exp\left(-\dfrac{t}{T_1}\right)\right) + M_z(0^+)\exp\left(-\dfrac{t}{T_1}\right) \end{cases} \tag{A.47}$$

where $M_{xy} = M_x + \mathrm{j}M_y$ is the transverse component of bulk magnetisation in the laboratory frame and

$$\begin{cases} M_{xy}(0^+) = M_0\sin(\alpha) \\ M_z(0^+) = M_0\cos(\alpha) \end{cases} \tag{A.48}$$

and α is the flip angle [2, 79]. A simple visualisation of the relaxation of magnetisation vector in longitudinal and transverse planes is illustrated in Figure A.7.

A.4 Signal detection

Detection of the NMR signal is performed based on the Faraday's law of electromagnetic induction which states that time-varying magnetic flux through a coil will induce a time varying electric voltage [2]. Based on Faraday's law, the voltage, $V(t)$, induced in the coil is calculated using:

$$V(t) = -\frac{\partial\Phi(t)}{\partial t} = -\frac{\partial}{\partial t}\int_{\text{object}} \vec{B}_r(\mathbf{r})\cdot\vec{M}(\mathbf{r},t)d\mathbf{r} \tag{A.49}$$

where $\vec{B}_r(\mathbf{r})$ is the magnetic field at location $\mathbf{r}$ and $\vec{M}(\mathbf{r},t)$ is the time varying bulk magnetisation vector at location $\mathbf{r}$.

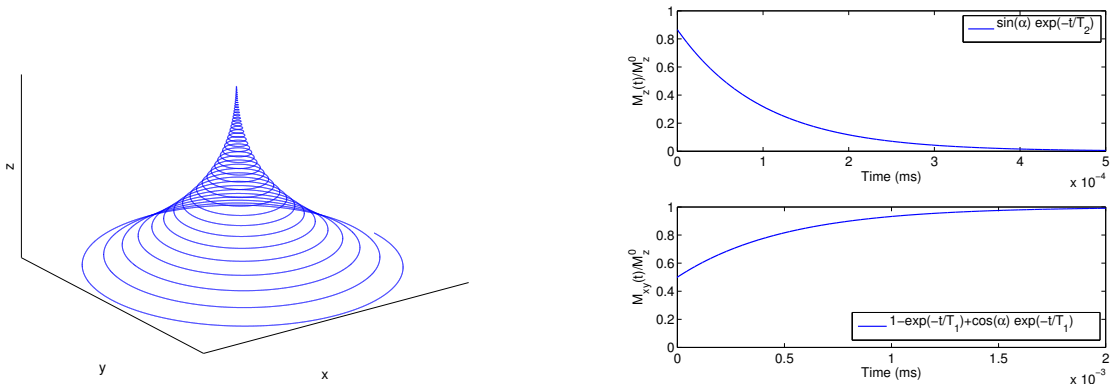

(a) (b)

Figure A.7: (a) The trajectory of the tip of magnetisation vector during relaxation period in laboratory frame (b) Relaxation curves in longitudinal and transverse planes after 60° excitation pulse

Assuming that the magnetic field $\vec{B}_r(\mathbf{r})$ is only a function of location $\mathbf{r}$, the voltage induced in the coil can be written as:

$$V(t) = -\frac{\partial \Phi(t)}{\partial t} = -\int_{\text{object}} \vec{B}_r(\mathbf{r}) \cdot \frac{\partial}{\partial t}\vec{M}(\mathbf{r},t)d\mathbf{r} \tag{A.50}$$

The magnetisation vector at location $\mathbf{r}$ and time t can be expressed in the laboratory frame as:

$$\vec{M}(\mathbf{r},t) = M_x(\mathbf{r},t)\vec{i} + M_y(\mathbf{r},t)\vec{j} + M_z(\mathbf{r},t)\vec{k} \tag{A.51}$$

in which using Eq. (A.47) and Eq. (A.48), we can write

$$\begin{cases} M_x(\mathbf{r},t) = M_0(\mathbf{r})\ \sin(\alpha) \exp\left(-\dfrac{t}{T_2(\mathbf{r})}\right) \cos\left(-\omega(\mathbf{r})t + \phi_e(\mathbf{r})\right) \\ M_y(\mathbf{r},t) = M_0(\mathbf{r})\ \sin(\alpha) \exp\left(-\dfrac{t}{T_2(\mathbf{r})}\right) \sin\left(-\omega(\mathbf{r})t + \phi_e(\mathbf{r})\right) \\ M_z(\mathbf{r},t) = M_0(\mathbf{r}) \left(1 - \exp\left(-\dfrac{t}{T_1(\mathbf{r})}\right)\right) + M_0(\mathbf{r}) \cos(\alpha) \exp\left(-\dfrac{t}{T_1(\mathbf{r})}\right) \end{cases} \tag{A.52}$$

where $\omega(\mathbf{r})$ is the Larmor frequency at location $\mathbf{r}$, $M_0(\mathbf{r})$ is the bulk magnetisation at location $\mathbf{r}$ before RF excitation and can be calculated using Eq. (A.22), α is the flip angle, and $\phi_e(\mathbf{r})$ is the initial phase shift induced by the RF excitation at location $\mathbf{r}$.

The derivative of magnetisation vector with respect to time at location $\mathbf{r}$ can be calculated as:

$$\frac{\partial}{\partial t}\vec{M}(\mathbf{r},t) = \frac{\partial}{\partial t}M_x(\mathbf{r},t)\vec{i} + \frac{\partial}{\partial t}M_y(\mathbf{r},t)\vec{j} + \frac{\partial}{\partial t}M_z(\mathbf{r},t)\vec{k} \tag{A.53}$$

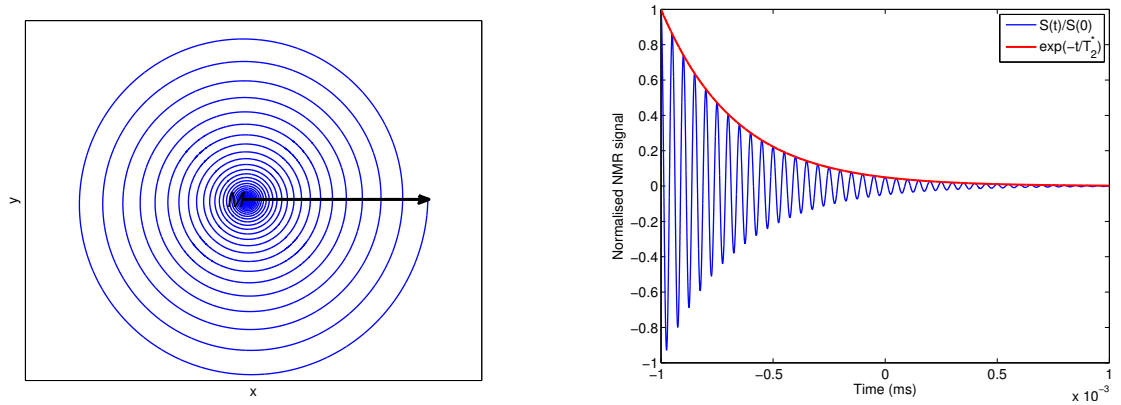

(a) (b)

Figure A.8: (a) Relaxation of transverse magnetisation vector in xy plane and (b) resultant NMR signal

where

$$\frac{\partial}{\partial t}M_x(\mathbf{r},t) = M_0(\mathbf{r})\,\sin(\alpha)\Bigg[-\frac{1}{T_2(\mathbf{r})}\exp\left(-\frac{t}{T_2(\mathbf{r})}\right)\cos\big(-\omega(\mathbf{r})t+\phi_e(\mathbf{r})\big) + \omega(\mathbf{r})\sin\big(-\omega(\mathbf{r})t+\phi_e(\mathbf{r})\big)\exp\left(-\frac{t}{T_2(\mathbf{r})}\right)\Bigg] \tag{A.54}$$

$$\frac{\partial}{\partial t}M_y(\mathbf{r},t) = M_0(\mathbf{r})\,\sin(\alpha)\Bigg[-\frac{1}{T_2(\mathbf{r})}\exp\left(-\frac{t}{T_2(\mathbf{r})}\right)\sin\big(-\omega(\mathbf{r})t+\phi_e(\mathbf{r})\big) - \omega(\mathbf{r})\cos\big(-\omega(\mathbf{r})t+\phi_e(\mathbf{r})\big)\exp\left(-\frac{t}{T_2(\mathbf{r})}\right)\Bigg] \tag{A.55}$$

and

$$\frac{\partial}{\partial t}M_z(\mathbf{r},t) = M_0(\mathbf{r})\left[\frac{1}{T_1(\mathbf{r})}\exp\left(-\frac{t}{T_1(\mathbf{r})}\right) - \frac{\cos(\alpha)}{T_1(\mathbf{r})}\exp\left(-\frac{t}{T_1(\mathbf{r})}\right)\right] \tag{A.56}$$

In practice, $\omega(\mathbf{r}) \gg \frac{1}{T_2(\mathbf{r})} > \frac{1}{T_1(\mathbf{r})}$. Hence the first terms in Eq. (A.54) and Eq. (A.55) can be neglected. The derivative of longitudinal magnetisation given in Eq. (A.56) also is small in comparison with the free precession rate. Hence the derivatives can be simplified to:

$$\frac{\partial}{\partial t}M_x(\mathbf{r},t) = M_0(\mathbf{r})\,\sin(\alpha)\,\omega(\mathbf{r})\,\exp\left(-\frac{t}{T_2(\mathbf{r})}\right)\sin\big(-\omega(\mathbf{r})t+\phi_e(\mathbf{r})\big) \tag{A.57}$$

and

$$\frac{\partial}{\partial t}M_y(\mathbf{r},t) = -M_0(\mathbf{r})\,\sin(\alpha)\,\omega(\mathbf{r})\,\exp\left(-\frac{t}{T_2(\mathbf{r})}\right)\cos\big(-\omega(\mathbf{r})t+\phi_e(\mathbf{r})\big) \tag{A.58}$$

A simple visualisation of the relaxation of the transverse magnetisation vector is depicted in Figure A.8. The magnetic field at location $\mathbf{r}$ can be expressed as:

$$\vec{B}_r(\mathbf{r}) = B_{r,x}(\mathbf{r})\vec{i} + B_{r,y}(\mathbf{r})\vec{j} + B_{r,z}(\mathbf{r})\vec{k} \tag{A.59}$$

where

$$\begin{aligned} B_{r,x}(\mathbf{r}) &= B_{r,xy}(\mathbf{r})\cos(\phi_r(\mathbf{r})) \\ B_{r,y}(\mathbf{r}) &= B_{r,xy}(\mathbf{r})\sin(\phi_r(\mathbf{r})) \end{aligned} \tag{A.60}$$

Here $\phi_r(\mathbf{r})$ is the reception phase angle. Substituting Eq. (A.57), Eq. (A.58) and Eq. (A.60) into Eq. (A.50), the voltage induced in coil is calculated as:

$$\begin{aligned} &V(t) = \\ &-\int_{\text{object}} M_0(\mathbf{r})\,\sin(\alpha)\,B_{\mathbf{r},xy}(\mathbf{r})\,\omega(\mathbf{r})\,\exp\left(-\frac{t}{T_2(\mathbf{r})}\right)\sin\big(-\omega(\mathbf{r})t+\phi_e(\mathbf{r})-\phi_r(\mathbf{r})\big)d\mathbf{r} = \\ &\int_{\text{object}} M_0(\mathbf{r})\,\sin(\alpha)\,B_{\mathbf{r},xy}(\mathbf{r})\,\omega(\mathbf{r})\,\exp\left(-\frac{t}{T_2(\mathbf{r})}\right)\cos\big(-\omega(\mathbf{r})t+\phi_e(\mathbf{r})-\phi_r(\mathbf{r})+\frac{\pi}{2}\big)d\mathbf{r} \end{aligned} \tag{A.61}$$

Most of modern scanners use a quadrature detection method in which the detection is performed using two coils perpendicular to each other. Therefore, if we consider that the second RF coil has a reception angle with $\frac{\pi}{2}$ difference with respect to the first coil, i.e. $\phi'_r(\mathbf{r}) = \phi_r(\mathbf{r}) + \frac{\pi}{2}$, the signal detected using the second coil can be calculated as:

$$\begin{aligned} &V'(t) = \\ &-\int_{\text{object}} M_0(\mathbf{r})\,\sin(\alpha)\,B_{\mathbf{r},xy}(\mathbf{r})\,\omega(\mathbf{r})\,\exp\left(-\frac{t}{T_2(\mathbf{r})}\right)\sin\big(-\omega(\mathbf{r})t+\phi_e(\mathbf{r})-\phi_r(\mathbf{r})-\frac{\pi}{2}\big)d\mathbf{r} \\ &=\int_{\text{object}} M_0(\mathbf{r})\,\sin(\alpha)\,B_{\mathbf{r},xy}(\mathbf{r})\,\omega(\mathbf{r})\,\exp\left(-\frac{t}{T_2(\mathbf{r})}\right)\sin\big(\omega(\mathbf{r})t-\phi_e(\mathbf{r})+\phi_r(\mathbf{r})+\frac{\pi}{2}\big)d\mathbf{r} \end{aligned} \tag{A.62}$$

Therefore, it is possible to consider the signals from two coils as a complex valued signal

$$\begin{aligned} S(t) &= V(t) + \mathrm{j}V'(t) \\ &= \exp\left(\mathrm{j}\frac{\pi}{2}\right) \int_{\text{object}} \vec{B}_{\mathbf{r},xy}(\mathbf{r}) \cdot \vec{M}_{xy}(\mathbf{r}, 0^+)\, \omega(\mathbf{r})\, \exp\left(-\frac{t}{T_2(\mathbf{r})}\right) \exp\left(-\mathrm{j}\omega(\mathbf{r})t\right) d\mathbf{r} \end{aligned} \tag{A.63}$$

where using complex notation we can define

$$\begin{cases} B_{\mathbf{r},xy}(\mathbf{r}) = B_{\mathbf{r},xy}(\mathbf{r})\, \exp\left(\mathrm{j}\phi_r(\mathbf{r})\right) \\ M_{xy}(\mathbf{r}, 0^+) = M_0(\mathbf{r}) \sin(\alpha)\, \exp\left(\mathrm{j}\phi_e(\mathbf{r})\right) \end{cases} \tag{A.64}$$

Considering a receiver coil considering a receiver coil with homogeneous reception field the MR signal induced in the coil can be simplified to:

$$S(t) = \exp\left(\mathrm{j}\frac{\pi}{2}\right) \int_{\text{object}} \omega(\mathbf{r})\, M_{xy}(\mathbf{r}, 0^+)\, \exp\left(-\frac{t}{T_2(\mathbf{r})}\right) \exp\left(-\mathrm{j}\omega(\mathbf{r})t\right) d\mathbf{r} \tag{A.65}$$

which can be simplified using Eq. (A.47) as

$$S(t) = \exp\left(\mathrm{j}\frac{\pi}{2}\right) \int_{\text{object}} \omega(\mathbf{r})\, M_{xy}(\mathbf{r}, t)\, d\mathbf{r} \tag{A.66}$$

Eq. (A.66) shows that the MR signal is only dependent on the transverse magnetisation. This expression can further be simplified by ignoring the initial phase of the transverse magnetisation ($\phi_e(\mathbf{r})$) and using the Eq. (A.64) which results in:

$$S(t) = \exp\left(\mathrm{j}\frac{\pi}{2}\right) \sin(\alpha) \int_{\text{object}} M_0(\mathbf{r})\, \omega(\mathbf{r})\, \exp\left(-\frac{t}{T_2(\mathbf{r})}\right) \exp\left(-\mathrm{j}\omega(\mathbf{r})t\right) d\mathbf{r} \tag{A.67}$$

Since the transverse magnetisation vector precesses at Larmor frequency, the received signal is modulated with a high frequency component. Therefore, in order to decrease the complexity of the electronic circuits needed for further processing the signal, the received signal is demodulated by a reference signal with Larmor frequency. The demodulation is performed using mixing the signal with a local oscillator with frequency equal to Larmor frequency and filtering out the high frequency component using a low-pass filter. Therefore, the output signal of the demodulator can be written as:

$$S_d(t) = \omega_0 \exp\left(\mathrm{j}\frac{\pi}{2}\right) \sin(\alpha) \int_{\text{object}} M_0(\mathbf{r})\, \exp\left(-\frac{t}{T_2(\mathbf{r})}\right) \exp\left(-\mathrm{j}\Delta\omega(\mathbf{r})t\right) d\mathbf{r} \tag{A.68}$$

where $\Delta\omega = \omega(\mathbf{r}) - \omega_0$ is the position related deviation of the Larmor frequency of the magnetisation vector. The scaling factor $\omega_0 \exp\left(\mathrm{j}\frac{\pi}{2}\right)$ is often omitted and the demodulated signal is expressed as:

$$S_d(t) = \sin(\alpha) \int_{\text{object}} M_0(\mathbf{r}) \exp\left(-\frac{t}{T_2(\mathbf{r})}\right) \exp\Big(-\mathrm{j}\Delta\omega(\mathbf{r})t\Big)\, d\mathbf{r} \tag{A.69}$$

For a heterogenous system, the distribution of the frequency deviations ($\Delta\omega$) can be described by a function $\rho(\omega)$. where,

$$M_0 = \int_{-\infty}^{\infty} \rho(\omega) d\omega \tag{A.70}$$

As a result, Eq. (A.67) can be written with resect to the spin spectral density function $\rho(\omega)$ as:

$$S(t) = \sin(\alpha) \int_{-\infty}^{\infty} \rho(\omega) \exp\left(-\frac{t}{T_2}\right) \exp\left(-\mathrm{j}\omega t\right) d\omega \tag{A.71}$$

where α is the flip angle.

A.5 Free Induction Decay

Free Induction Decay (FID) signal as can be expected from its name, is generated by the free precession of the excited bulk magnetisation vector $\vec{M}$ about the $\vec{B}_0$ field [2]. The free induction decay signal after an α pulse can be expressed using Eq. (A.71), in which the decay rate depends on T_2 and the spin spectral density function $\rho(\omega)$. If the sample and external magnetic field are both homogeneous the FID signal posseses the T_2 characteristic decay. However, this is not true in reality and usually the sample and magnetic field are heterogenous. As a result, the decay characteristic is much faster which is shown by T_2^*. For the case in which the magnetic field inhomogeneity can be modelled using a Lorentzian distribution:

$$\rho(\omega) = M_0 \frac{(\gamma\Delta B_0)^2}{(\gamma\Delta B_0)^2 + (\omega - \omega_0)^2} \tag{A.72}$$

the resultant FID signal can be calculated using Eq. (A.71) as:

$$\begin{aligned} S(t) &= \sin(\alpha) \int_{-\infty}^{\infty} M_0 \frac{(\gamma \Delta B_0)^2}{(\gamma \Delta B_0)^2 + (\omega - \omega_0)^2} \exp\left(-\frac{t}{T_2}\right) \exp\left(-\mathrm{j}\omega t\right) d\omega \\ &= \sin(\alpha) \int_{-\infty}^{\infty} \left[M_0 \frac{(\gamma \Delta B_0)^2}{(\gamma \Delta B_0)^2 + \omega^2} \exp\left(-\mathrm{j}\omega t\right) \right] \exp\left(-\frac{t}{T_2}\right) \exp\left(-\mathrm{j}\omega_0 t\right) d\omega \\ &= \pi M_0 \gamma \Delta B_0 \sin\left(\alpha\right) \exp\left(-\gamma \Delta B_0 t\right) \exp\left(-\frac{t}{T_2}\right) \exp\left(-\mathrm{j}\omega_0 t\right) \\ &= \pi M_0 \gamma \Delta B_0 \sin\left(\alpha\right) \exp\left(-\frac{t}{T_2^*}\right) \exp\left(-\mathrm{j}\omega_0 t\right) \qquad \forall t \geq 0 \end{aligned} \tag{A.73}$$

where

$$\frac{1}{T_2^*} = \frac{1}{T_2} + \gamma \Delta B_0 \tag{A.74}$$

T_2^* indicates the decay characteristics of the MR signal created after the RF excitation pulse. Eq. (A.74) is valid only when the field inhomogeneity could be modelled by Lorentzian distribution. For other types of spectral density functions the decay curve will not posses an exponential envelope function. In this case T_2^* is approximated by the time constant of the effective exponential envelope.

A.6 Spin Echoes

Spin echo is another form of MR signal which are created by refocusing and dephasing of the transverse magnetisation vector components [63]. Spin echo is generated by application of multiple RF pulses [2]. The simplest form of pulse sequence for producing a spin echo consists of a 90° pulse followed by a 180° pulse after certain time ($TE/2$) as depicted in Figure A.9. The total time from the first pulse until occurring echo signal is called Echo time (TE).

A.7 Gradient Echoes

Gradient echoes are another form of echo signals which are generated by application of time varying gradient fields to rephase the excited transverse magnetisation vectors. [2]. A gradient field, $\vec{B}_G$, is defined as an inhomogeneous magnetic field whose z-component, $B_{G,z}$, varies linearly with respect to certain spatial direction. The direction by which the gradient field varies linearly is called the gradient direction. The gradient system consists of three gradient coils referred to as x-gradient, y-gradient and z-gradient fields for which $B_{G,z} = G_x x$, $B_{G,z} = G_y y$ and $B_{G,z} = G_z z$ respectively. The gradient fields have also components in the x and y directions but these components are very small in comparison with the B_0 field in the z direction and are neglected [2].

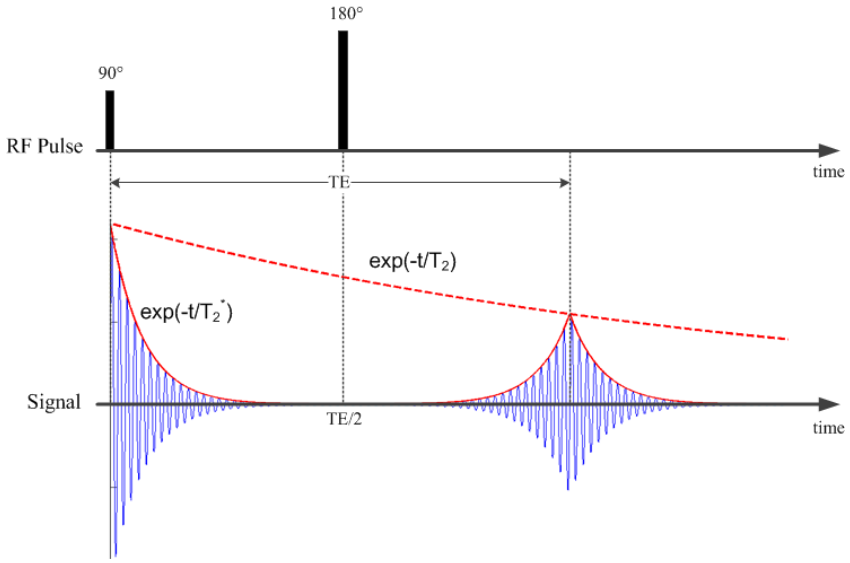

Figure A.9: A simple Spin Echo sequence. The dephased transverse magnetisation vectors created by the first RF pulse are refocused using the second RF pulse to create the echo signal. The decay of the FID signal follows T_2^* characteristics while the amplitude of the echo signal is related to the T_2 value of the sample.

The total gradient field at any local point ($\mathbf{r}$) can be written as:

$$B_G = G_x x + G_y y + G_z z \tag{A.75}$$

which can be written as an inner product of the gradient vector $\vec{G}$ and the spatial position $\mathbf{r} = x\vec{i} + y\vec{j} + z\vec{k}$, where the gradient vector is defined as:

$$\vec{G} = \vec{\nabla} B_{G,z} = G_x\vec{i} + G_y\vec{j} + G_z\vec{k} \tag{A.76}$$

where $\vec{\nabla}$ operator is defined as:

$$\vec{\nabla} = \frac{\partial}{\partial x}\vec{i} + \frac{\partial}{\partial y}\vec{j} + \frac{\partial}{\partial z}\vec{k} \tag{A.77}$$

As a result, the total magnetic field at point $\mathbf{r}$ is the sum of the static field B_0 and the gradient field at position $\mathbf{r}$ and time t

$$\vec{B}(\mathbf{r}, t) = (B_0 + \vec{G}(t) \cdot \mathbf{r})\vec{k} \tag{A.78}$$

As a result of application of location dependent gradient magnetic field, the spins at different locations experience different total magnetic field $\vec{B}(\mathbf{r})$. Therefore, the angular frequency of a particle at point $\mathbf{r}$ can be calculated according to Eq. (A.14) as:

$$\vec{\omega}(\mathbf{r}, t) = 2\pi\gamma\vec{B}(\mathbf{r}, t) = 2\pi\gamma\left(B_0 + \vec{G}(t) \cdot \mathbf{r}\right)\vec{k} \tag{A.79}$$

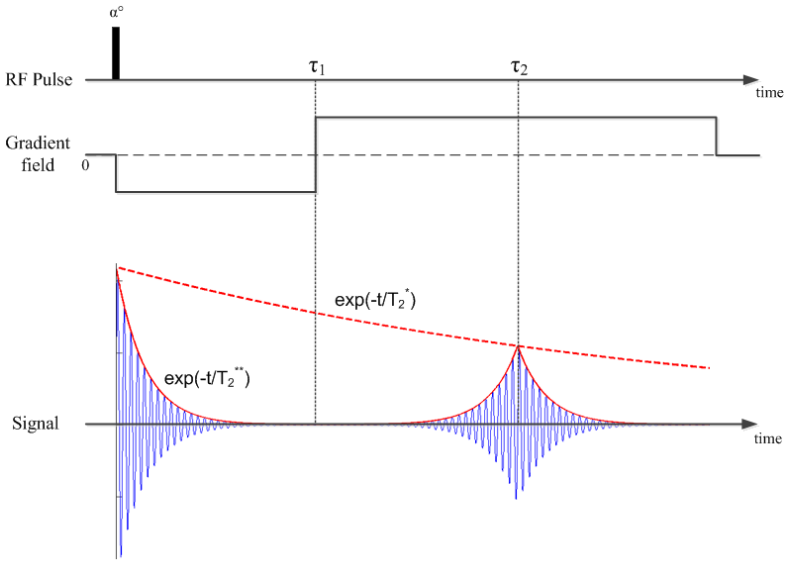

Figure A.10: A simple Gradient Echo sequence. The dephased transverse magnetisation vectors during the negative gradient field are refocused during the positive gradient field. The decay of the FID signal in this case follows T_2^{**} time constant while the amplitude of the echo signal is related to the T_2^* characteristics.

Hence, the offset in the angular frequency of particles with respect to the case when the gradient field was not applied is:

$$\begin{aligned}\Delta\omega(\mathbf{r},t) &= \omega(\mathbf{r},t) - \omega_0 \\ &= 2\pi\gamma(B_0 + \vec{G}(t)\cdot\mathbf{r} - B_0) \\ &= 2\pi\gamma\,\vec{G}(t)\cdot\mathbf{r}\end{aligned} \tag{A.80}$$

where $\omega_0 = 2\pi\gamma B_0$ is the Larmor frequency in the absence of the gradient field. The change in the precession frequency of particles will induce a location dependent phase offset

$$\begin{aligned}\Delta\phi(\mathbf{r},t) &= \int_0^t \Delta\omega(\mathbf{r},t')\,dt' \\ &= 2\pi\gamma\int_0^t \vec{G}(t')\cdot\mathbf{r}\,dt'\end{aligned} \tag{A.81}$$

Therefore, the transverse magnetisation vector at location $\mathbf{r}$ in the presence of a gradient field $\vec{G}$ and considering the static field inhomogeneity is calculated as:

$$\vec{M}_{xy}(\mathbf{r},t) = \vec{M}_{xy}(\mathbf{r},0^+)\exp\left[-\frac{t}{T_2(\mathbf{r})} - \mathrm{j}\,(\omega_0 t + \Delta\phi(\mathbf{r},t))\right] \tag{A.82}$$

where $\vec{M}_{xy}(\mathbf{r}, 0^+)$ is the transverse magnetisation vector immediately after RF excitation pulse. The MR signal in presence of gradient field is calculated by substituting Eq. (A.82) and Eq. (A.64) into Eq. (A.66) which results in:

$$S(t) = \exp\left(\mathrm{j}\frac{\pi}{2}\right)\omega_0 \sin(\alpha) \int_{\text{object}} M_0(\mathbf{r}) \exp\left[-\frac{t}{T_2(\mathbf{r})} - \mathrm{j}\left(\omega_0 t + \Delta\phi(\mathbf{r}, t)\right)\right] d\mathbf{r} \quad \text{(A.83)}$$

where $M_0(\mathbf{r})$ is the magnetisation before application of RF excitation pulse at location $\mathbf{r}$ and α is the flip angle after application of RF pulse. $\Delta\phi(\mathbf{r}, t)$ is the phase offset induced by the application of gradient field which can be calculated using Eq. (A.81) for the case of single gradient $\vec{G}(t)$.

Application of gradient fields for producing gradient echo signals is depicted in Figure A.10. A negative gradient $-\vec{G}_1$ is turned on after an RF pulse excites the magnetisation vector. As a result of gradient field the spins in different spatial positions acquire different phase offsets which can be expressed as:

$$\Delta\phi(\mathbf{r}, t) = 2\pi\gamma \int_0^t -\vec{G}_1 \cdot \mathbf{r}\, dt' = -2\pi\gamma(\vec{G}_1 \cdot \mathbf{r})t \qquad 0 \leq t \leq \tau_1 \quad \text{(A.84)}$$

Eq. (A.84) depicts that the phase difference increases as the time elapses and results in the decay of the signal which is characterised by another time constant T_2^{**}. At time τ, the gradient field changes its polarity resulting in a positive gradient field $\vec{G}_2$. The phase offset of spins after the second gradient pulse is calculated as:

$$\Delta\phi(\mathbf{r}, t) = -2\pi\gamma(\vec{G}_1 \cdot \mathbf{r})\tau_1 + 2\pi\gamma \int_{\tau_1}^t \vec{G}_2 \cdot \mathbf{r}\, dt' = 2\pi\gamma\left(-(\vec{G}_1 \cdot \mathbf{r})\,\tau_1 + (\vec{G}_2 \cdot \mathbf{r})(t - \tau_1)\right)$$
$$\tau_1 \leq t \leq \tau_2 \quad \text{(A.85)}$$

The total MR signal during the application of gradient echo signal can be calculated by substituting Eq. (A.85) into Eq. (A.83).

In the particular case when $\vec{G}_1 = \vec{G}_2 = \vec{G}$, the phase offset can be simplified as:

$$\Delta\phi(\mathbf{r}, t) = 2\pi\gamma\left(\vec{G} \cdot \mathbf{r}\right)(-2\,\tau_1 + t) \quad \text{(A.86)}$$

and the phase offset will become zero at time $t = 2\tau_1$. The analysis presented above was under the assumption of static magnetic field homogeneity. However, it should be noted that in the case that the static magnetic field B_0 is inhomogeneous, the spins will not be completely rephased by the gradient reversal and the amplitude of echo signal will follow T_2^* characteristics in this case, which differs from the spin echo [2].

B Solution to diffusion equation

Based on Fick's second law, the diffusion equation is presented as:

$$\frac{\partial c(\mathbf{r},t)}{\partial t} = D_0 \nabla^2 c(\mathbf{r},t) \tag{B.1}$$

where $c(\mathbf{r},t)$ is the concentration density at position $\mathbf{r} = [r_{x_1}, r_{x_2}, ..., r_{x_n}]^T$ and time t and D_0 is the diffusion coefficient (diffusivity).

The concentration of particles can be written in term of the conditional probability density function as:

$$c(\mathbf{r},t) = \int_{-\infty}^{\infty} c(\mathbf{r}_0,0) P(\mathbf{r}|\mathbf{r_0},t) d\mathbf{r_0} \tag{B.2}$$

where $P(\mathbf{r}|\mathbf{r_0},t)$ is the conditional probability density for a particle starting at position $\mathbf{r}_0$ ending up at position $\mathbf{r}$ during time t.

We assume that the diffusion is independent of the starting point. Hence, the concentration density can be replaced by the conditional probability density $P(\mathbf{r}|\mathbf{r_0},t)$ and the diffusion equation can be written as:

$$\frac{\partial P(\mathbf{r}|\mathbf{r_0},t)}{\partial t} = D_0 \nabla^2 P(\mathbf{r}|\mathbf{r_0},t) \tag{B.3}$$

We wish to solve:

$$\frac{\partial P(\mathbf{r}|\mathbf{r_0},t)}{\partial t} = D_0 \frac{\partial}{\partial \mathbf{r}} \cdot \frac{\partial}{\partial \mathbf{r}} P(\mathbf{r}|\mathbf{r_0},t) \tag{B.4}$$

with the initial condition:

$$P(\mathbf{r}|\mathbf{r_0},0) = \delta(\mathbf{r} - \mathbf{r}_0) \tag{B.5}$$

and boundary condition as:

$$\lim_{|\mathbf{r}|\to\infty} P(\mathbf{r}|\mathbf{r_0},t) = 0 \qquad \forall t > 0 \tag{B.6}$$

which depicts that the particle is at position $\mathbf{r}_0$ at time $t = 0$ and the probability for a particle to reach $r = \pm\infty$ is zero. We utilise the Fourier transform in spatial domain defined as:

$$\tilde{P}(\mathbf{k}_r,t) = \int_{-\infty}^{\infty} P(\mathbf{r}|\mathbf{r}_0,t)\, \exp\left(-\mathrm{j}\, 2\pi \mathbf{k}_r \cdot \mathbf{r}\right) d\mathbf{r} \tag{B.7}$$

to solve the partial differential equation (PDE). $\mathbf{k}_r = [k_{x_1}, k_{x_2}, ..., k_{x_n}]^T$ denotes the wavenumber in different directions. Taking the Fourier transform of Eq. (B.4) we have

$$\begin{aligned}\frac{\partial \tilde{P}(\mathbf{k}_r, t)}{\partial t} &= D_0 \int_{-\infty}^{\infty} \frac{\partial}{\partial \mathbf{r}} \cdot \frac{\partial}{\partial \mathbf{r}} P(\mathbf{r}|\mathbf{r_0}, t) \, \exp\left(-\mathrm{j}\, 2\pi \mathbf{k}_r \cdot \mathbf{r}\right) d\mathbf{r} \\ &= -4\pi^2 \, D_0 \, |\mathbf{k}_r|^2 \, \tilde{P}(\mathbf{k}_r, t) \end{aligned} \tag{B.8}$$

where we have used the differentiation property of the Fourier transform. Using the Fourier transform, we converted the PDE in Eq. (B.4) to a simple first order Ordinary Differential Equation (ODE) in Eq. (B.8). The solution for this ODE is in the form:

$$\tilde{P}(\mathbf{k}_r, t) = \tilde{P}(\mathbf{k}_r, 0) \, \exp\left(-4\pi^2 \, D_0 \, |\mathbf{k}_r|^2 \, t\right) \qquad \forall t > 0 \tag{B.9}$$

where $\tilde{P}(\mathbf{k}_r, 0)$ is the Fourier transform of the initial condition as:

$$\begin{aligned}\tilde{P}(\mathbf{k}_r, 0) &= \int_{-\infty}^{\infty} \delta(\mathbf{r} - \mathbf{r}_0) \, \exp\left(-\mathrm{j}\, 2\pi \mathbf{k}_r \cdot \mathbf{r}\right) d\mathbf{r} \\ &= \exp\left(-\mathrm{j}\, 2\pi \mathbf{k}_r \cdot \mathbf{r}_0\right) \end{aligned} \tag{B.10}$$

Taking inverse Fourier transform of Eq. (B.9), we have

$$\begin{aligned}P(\mathbf{r}|\mathbf{r_0}, t) &= \int_{-\infty}^{+\infty} \tilde{P}(\mathbf{k}_r, t) \, \exp\left(\mathrm{j}\, 2\pi \mathbf{k}_r \cdot \mathbf{r}\right) d\mathbf{k}_r \\ &= \int_{-\infty}^{+\infty} \exp\left(-4\pi^2 \, D_0 \, |\mathbf{k}_r|^2 \, t\right) \, \exp\left(\mathrm{j}\, 2\pi \mathbf{k}_r \cdot [\mathbf{r} - \mathbf{r}_0]\right) d\mathbf{k}_r \end{aligned} \tag{B.11}$$

Considering the separability of the integrals in Cartesian space, the solution to the above integral is a Green's function calculated as:

$$\begin{aligned}P(\mathbf{r}|\mathbf{r_0}, t) &= \int_{-\infty}^{+\infty} \exp\left(-4\pi^2 \, D_0 \, |\mathbf{k}_r|^2 \, t\right) \, \exp\left(\mathrm{j}\, 2\pi \sum_{i=1}^{n} k_{x_i} (r_{x_i} - r_{0,x_i})\right) \prod_{i=1}^{n} dk_{x_i} \\ &= \left[\int_{-\infty}^{+\infty} \exp\left(-4\pi^2 \, D_0 \, |\mathbf{k}_r|^2 \, t\right) \, \exp\left(\mathrm{j}\, 2\pi k_{x_i} (r_{x_i} - r_{0,x_i})\right) dk_{x_i}\right]^n \end{aligned} \tag{B.12}$$

Therefore, the diffusion propagator for the case of isotropic and free diffusion can be written as:

$$P(\mathbf{r}|\mathbf{r_0}, t) = \frac{1}{(4\pi D_0 t)^{n/2}} \, \exp\left(-\frac{|\mathbf{r} - \mathbf{r}_0|^2}{4 D_0 t}\right) \qquad \forall t > 0 \tag{B.13}$$

where n is the spatial dimension (The number of elements of $\mathbf{r}$). The Green's Function indictes how a single point of probability density initially at $\mathbf{r}_0$ evolves in time and space.

Eq. (B.13) indicates that diffusion is happening in precisely the same way, independently in all dimensions and diffusion in 3D is identical to diffusion in 1D happening simultaneously on three orthogonal axes. This property is only valid for the case of free and isotropic diffusion in which the diffusion tensor is time-invariant and $\mathbf{D}(t) = D_0\mathbf{I}_n$ and we can use the separability of the PDE. In general the diffusion is not isotropic and the solution for the disunion equation would be more complicated.